

**University of New Mexico
UNM Digital Repository**

Optical Science and Engineering ETDs

Engineering ETDs

6-9-2016

Ultrafast Broadband Terahertz Spectroscopy

Chia-Yeh Li

Follow this and additional works at: https://digitalrepository.unm.edu/ose_etds

Recommended Citation

Li, Chia-Yeh. "Ultrafast Broadband Terahertz Spectroscopy." (2016). https://digitalrepository.unm.edu/ose_etds/16

This Dissertation is brought to you for free and open access by the Engineering ETDs at UNM Digital Repository. It has been accepted for inclusion in Optical Science and Engineering ETDs by an authorized administrator of UNM Digital Repository. For more information, please contact disc@unm.edu.

Chia-Yeh Li

Candidate

Department of Physics and Astronomy

Department

This dissertation is approved, and it is acceptable in quality and form for publication:

Approved by the Dissertation Committee:

Mansoor Sheik-Bahae , Chairperson

Kevin J. Malloy

Majeed Hayat

Jeffrey G. Cederberg

ULTRAFAST BROADBAND TERAHERTZ SPECTROSCOPY

by

CHIA-YEH LI

B.S., National Tsing Hua University, 2003
M.S., University of New Mexico, 2009

DISSERTATION

Submitted in Partial Fulfillment of the
Requirements for the Degree of

**Doctorate of Philosophy
Optical Science and Engineering**

The University of New Mexico
Albuquerque, New Mexico

May 2016

ACKNOWLEDGEMENTS

I am grateful for the opportunity to work under the advisement of Mansoor Sheik-Bahae. His creative thinking and insights have been great inspiration to me. Throughout my graduate study I have learnt much from him and the diverse topics that we worked upon.

I have come to envy Michael Hasselbeck's enthusiasm in science, and very thankful for the advices and help he has given me during my pursuit of the Ph.D. degree. He never hesitates to lend a hand in troubleshooting the experiments, which is extremely valuable when I was short in laboratory experience.

Denis Seletskiy is a very knowledgeable previous group member, who brought me into the world of ultrafast terahertz spectroscopy. My researches in ultrafast spectroscopy are based on the foundations he laid down, and constantly benefited from the discussions and ideas that he generously offered.

I appreciate the constructive comments from Dr. Richard Epstein and Dr. Kevin Malloy. I would like to thank our collaborator Dr. Jeffery Cederberg (currently at MIT Lincoln laboratory) for both his skillful MOCVD growing and kindly filling a position in my defense committee. I would also like to thank Dr. Rolf Binder for the collaboration on semiconductor laser cooling device characterization. Past group members Andreas Stintz, Chengao Wang, Daniel Bender, Wendy Patterson, Seth Melgaard, and Mahendra Man Shakya have been very helpful and joy to work with. Working in the lab with Aram Gragossian and Zhou Yang were more than enjoyable, not to mention the positive discussions that inspired me from time to time. Alexander Albrecht has been of great assistance, and provided wild range of advices from machining to solutions fulfilling experimental needs. Mohammad Reza Ghasemkhani, Junwei Meng, Nathan Giannini, and Saeid Rostami have all been very helpful. I would like to thank my committee members Mansoor Sheik-Bahae, Majeed Hayat Kevin Malloy, and Jeffery Cederberg for their insightful comments.

Last but not least, I would like to thank my family for their long lasting support, without which I could not have completed the long journey toward the Ph.D. degree.

ULTRAFAST BROADBAND TERAHERTZ SPECTROSCOPY

By

Chia-Yeh Li

B.S., Physics, National Tsing Hua University, 2003

M.S., Optical Science and Engineering, University of New Mexico, 2009

Ph.D., Optical Science and Engineering, University of New Mexico, 2016

ABSTRACT

This dissertation centers on broadband terahertz spectroscopy and is arranged in four main sections. In the first section, we describe terahertz generation from a two-color laser air breakdown plasma. This is modeled with a plasma current that includes plasma density and dispersion in propagation. The terahertz spatial profile has a ring-like structure with a frequency dependent radius. Parameters for optimal terahertz generation are also presented. The next two sections discuss broadband terahertz detection techniques: optically biased coherent detection and electro-absorption in a semiconductor. The subject of the fourth section is terahertz imaging with electroabsorption.

Optically biased coherent detection is distinguished from air-breakdown coherent detection by replacing the electrical bias for an optical field. The importance of phase control in this technique is demonstrated. In addition, we found the terahertz-induced second harmonic to be spectrally delay-dependent. This is due to the phase matching condition and is discussed in detail.

Terahertz-induced electro-absorption is performed in GaAs/AlGaAs multiple double quantum wells and an AlGaAs bulk semiconductor. To the best of the author's knowledge, this is the first demonstration of large modulation induced by a single cycle terahertz pulse in such structures. The underlying mechanism is identified as the Franz-Keldysh effect that has been successfully modeled in both the temporal and spectral regimes.

Terahertz imaging of the plasma profile is accomplished with electro-absorption in these structures. The observed ring pattern is reproduced with the model described in the first section of this dissertation. Terahertz raster scan imaging of a large object is also presented.

Table of Contents

Table of Contents	vi
List of Figures	viii
Chapter 1. Introduction.....	1
1.1. Motivation	1
1.2. Dissertation outline	3
Chapter 2. Broadband THz generation	5
2.1. Method of THz generation	5
2.2. Broadband THz generation in gaseous medium	12
2.3. Modeling THz generation	13
Chapter 3. Broadband Terahertz Detection I.....	23
3.1. Methods of Terahertz Detection.....	23
3.2. Air-Breakdown Coherent Detection.....	28
3.3. Optically Biased Coherent Detection.....	31
3.4. OBCD Experimental setup.....	31
3.5. OBCD results and discussion.....	42
Chapter 4. Broadband Terahertz Detection II	51
4.1. THz induced electroabsorption in Semiconductors	51
4.2. THz-EA Experimental Setup	53

4.3. THz-EA results and discussion	56
Chapter 5. THz Electroabsorption Imaging.....	66
5.1. Introduction	66
5.2. THz-EA imaging Experimental Setup	68
5.3. THz-EA imaging results and discussion	70
Chapter 6. Conclusion and Research Outlook.....	75
Appendix A FemtoFit	77

List of Figures

Figure 1.1 Spectral range of terahertz [1]	1
Figure 1.2 Examples of THz applications. THz raster imaging with photoconductive antenna [3] of (a) integrated circuit in plastic packaging, and (b) water contents in leaf. (c) Drug detection showing MDMA, aspirin, and methamphetamine (left to right) imaged at seven different wavelengths [4].....	2
Figure 2.1 (a) Schematic of photoconductive antenna, (b) grown antennas without MSM, and (c) example antenna design. Antennas shown in (b) and (c) were grown by Dr. Jeffrey Cederberg at Sandia National Laboratory.	9
Figure 2.2 (a) Spatially-ordered array of InAs nanowires, grown using MOCVD by Dr. Jeffrey Cederberg at Sandia National Laboratory. (b) Linear autocorrelations (top) of the emitted THz are measured using bolometer for two orthogonal pump polarizations. Corresponding FFT spectra are shown below. Dotted lines represent control signal obtained from unstructured bulk InAs.....	11
Figure 2.3 Experimental scheme for two-color gas plasma THz generation.....	12
Figure 2.4 Energy level diagram for THz generation.	13
Figure 2.5 (a) polarsymmetry-broken two-color field $\tilde{E}(t)$, and (b) dynamics of the ionized charge density $\tilde{\rho}_e(t)$	15
Figure 2.6 $ G(\omega) $ in the numerical modeling, assuming 30% SHG conversion efficiency.....	16
Figure 2.7 (a) On axis ($r=0$) THz polarization strength integrated over frequency versus relative phase $\Delta\phi$, calculated with 9 % SHG intensity ratio with respect to the fundamental field. The electric field strength for each line is shown in the legend. (b) Dependence of the plasma frequency on the relative phase due to the variation of ionization.	18

Figure 2.8 (a) single-cycle composite electric field $\tilde{E}(t)$, (b) ionization rate $\tilde{W}_i(t)$, and (c) ionized number density $\tilde{\rho}_e(t)$. Assuming peak electric field strength of 3.03E10 V/m.....	19
Figure 2.9 On axis ($r=0$) THz polarization strength integrated over frequency v.s. phase $\Delta\phi$ at various mixing of ω and 2ω	20
Figure 2.10 (a) Modeled THz profile, and (b) including diffraction from finite numerical aperture from off-axis parabolic mirrors. The z axis of the plot is $\log(intensity)$	22
Figure 3.1 (a) Bandwidth comparison between pyroelectric detector (Gentec SPI-A-65THz) and bolometer (Infrared Laboratories). (b) Comparison between nitrogen purged (red) and unpurged measurements (black).	24
Figure 3.2 Schematic for THz detection using a photoconductive switch.	24
Figure 3.3 polarizations for EOS in $<110>$ ZnTe.....	26
Figure 3.4 Schematic for electro-optic sampling with balanced detection.	27
Figure 3.5 Experimental data of EOS with 0.5 mm ZnTe, the ultrafast THz source is derived from optical rectification with ZnTe.....	27
Figure 3.6 Calculated TISH generation v.s. applied THz field strength via plasma current model. An extrapolated linear fit of low field strength region (dashed line) illustrates the deviation at high fields.....	29
Figure 3.7 Schematic of OBCT experimental setup.....	32
Figure 3.8 photo of OBCT experimental setup (waveguide and its 3-axis translation stage is not shown here).....	33
Figure 3.9 Knife-edge measurements of THz spot sizes at two different positions.	34
Figure 3.10 Metallic waveguide. Waveguide is glued to a post that is mounted on a 3-axis translation stage.	34

Figure 3.11 Schematics for (a) the parallel plate THz waveguide with coupling cylindrical lens on both ends [93], and (b) the metal wire THz waveguide [94].	36
Figure 3.12 Transmission of a hollow metallic wave guide with inner diameter of 100 μm [87]. THz source originates from a two-color plasma. The 10 fs pump pulse consists of 10^{14} W/cm^2 and $2 \cdot 10^{13} \text{ W/cm}^2$ intensity of fundamental and second harmonic wave, respectively. (a) Spectra of the propagated THz in log scale, and (b) the waveform of the propagated THz ($< 250 \text{ THz}$) components. Propagation distance of 0.5, 2, and 10mm are represented with black dashed, green, and red lines, respectively.	37
Figure 3.13 Polarizations of \tilde{E}_ω , $\tilde{E}_{2\omega}^{LO}$, and \tilde{E}_{THz} .	38
Figure 3.14 Schematic of phase control using phase plate.	39
Figure 3.15 Fused silica wedges pair. (a) photo and (b) schematic.	40
Figure 3.16 Schematic for phase control using calcite plate.	41
Figure 3.17 Schematic for delay dependent TISH spectra measurement.	41
Figure 3.18 (a) OBCD time trace demonstrating coherent detection; the signal inverts when $\Delta\phi = \pi$. (b) Corresponding spectrum $E(\omega)$.	43
Figure 3.19 (a) TISH peak signal v.s. THz power, (b) OBCD peak signal v.s. THz field strength.	43
Figure 3.20 Measured OBCD signal $\tilde{S}_{2\omega}(\tau, \Delta\phi)$.	44
Figure 3.21 (a) TISH spectral peak v.s. delay, peak of bias $2\omega \approx 397 \text{ nm}$. (b) Integrated TISH signal v.s. delay.	45
Figure 3.22 (a) Wave vector diagram for the two possible processes of the TISH generation. (b) Angular phase matching for $\Delta k < 0$. (c) Calculated phase mismatch vs frequency for ω_{TISH}^+ and	

ω_{TISH}^- , assuming plasma frequency of 1.3 THz, and (d) angular phase matching angle for the $\Delta k < 0$ case.....	46
Figure 3.23 Measured (solid line) and calculated (dashed line) TISH and measured bias SH spectra at zero delay. Phase-matching is considered for 8 THz. The redshifted TISH spectrum demonstrates the dominance of the $\omega_{TISH}^- = 2\omega - \omega_{THz}$ process.	48
Figure 3.24 Numerically modeled OCD signal $S_{2\omega}(\tau, \Delta\phi)$. (a) No deviation of TISH central wavelength from injection wavelength, and (b) with 4 nm shift in TISH central wavelength....	49
Figure 3.25 Spectrally integrated TISH polarization v.s. THz field strength.	50
Figure 4.1 Single-cycle THz induced electroabsorption in AlGaAs at 793.9 nm. (a) EA v.s. THz-NIR probe delay with $\Delta T/T_0 \approx 40\%$, and (b) corresponding power spectrum showing bandwidth exceeding 7 THz.	52
Figure 4.2 Schematic of THz-EA experimental setup.	53
Figure 4.3 (a) Supercontinuum generation and spectral modulation. (b) Photo of the setup without sapphire crystal and knife edge.....	54
Figure 4.4 (a) Structure of SDQW, and (b) photoluminescence (PL) spectra of ADQW and SDQW.....	56
Figure 4.5 Photo of large area $\text{Al}_{0.11}\text{Ga}_{0.89}\text{As}$ sample, bonded to a glass slide.....	56
Figure 4.6 Calculated Franz-Keldysh oscillation (red and blue lines, $F>0$), compared to free carrier absorption (blue line, $F=0$).	59
Figure 4.7 (a) Measured normalized EA response $\Delta T(\lambda, \tau)/T_0(\lambda)$ of the $\text{Al}_{0.11}\text{Ga}_{0.89}\text{As}$ bulk sample, and (b) $\Delta T(\lambda, \tau)/T_0(\lambda)$ modeled using FKE.	60
Figure 4.8 Multiple reflections in bonded EA samples.	61

Figure 4.9 (a) Calculated EA response $\Delta T(\lambda, \tau)/T_0(\lambda)$ by combined effect of the FKE and Fabry-Perot. (b) $\Delta T(\lambda, \tau)/T_0(\lambda)$ data at single delay (circle dots), fitted with the FKE and Fabry-Perot Effect (red line), and same fit with the Fabry-Perot effect turned off (blue line).....	63
Figure 4.10 OCD measured THz waveform (blue line), and THz waveform extracted form $\Delta T(\lambda, \tau)/T_0(\lambda)$ (red line).....	64
Figure 4.11 (a) Measured and (b) modeled $\Delta T(\lambda, \tau)/T_0(\lambda)$ for SDQW structure at 135K.....	64
Figure 4.12 Measured and modeled $\Delta T(\lambda, \tau)/T_0(\lambda)$ for GaAs structure at room temperature with spectrally filtered supercontinuum probe.....	65
Figure 5.1 Calculated $\Delta T/T_0$ versus field strength F, including Franz-Keldysh and Fabry-Perot effect. Band edge wavelength used is 797 nm. (a) $\Delta T/T_0$ across all wavelengths, and (b) $\Delta T/T_0$ at 793 nm and 805 nm.....	67
Figure 5.2 Schematic for direct THz-EA imaging setup.	68
Figure 5.3 Schematic for THz-EA raster scan imaging setup.	69
Figure 5.4 Photo of the detection section of THz EA imaging setup.	70
Figure 5.5 THz profiles at the generation point. (a) pump power of 1.1W, and (b) 0.9W.....	71
Figure 5.6 THz profile at the generation point with gold waveguide.....	72
Figure 5.7 3D printed imaging objects. From left to right: the object for raster imaging, 100 μm cross slits, 200 μm cross slits, and 300 μm cross slits.	73
Figure 5.8 THz EA raster imaging.....	73
Figure 5.9 Schematic for arrayed THz-EA detection.	74
Figure A.0.1 MIIPS trace with transform limited pulse [128].....	78

Figure A.0.2 (a) Photo of the MIIPS optics, and (b) the FemtoFit software interface. Optimization of Ti:Sapphire oscillator laser pulse is shown. 79

Chapter 1. Introduction

1.1. Motivation

Located in frequency too high for electronics, and wavelength to long for optics, the so-called ‘terahertz gap’ was an area that previously rarely accessed by both areas of research. In the frequency range typically defined to be between 0.1 to 10 THz (3 mm to 300 μm for wavelength), terahertz ($\text{THz} = 10^{12} \text{ Hz}$) has generated a lot of interests in recent years.

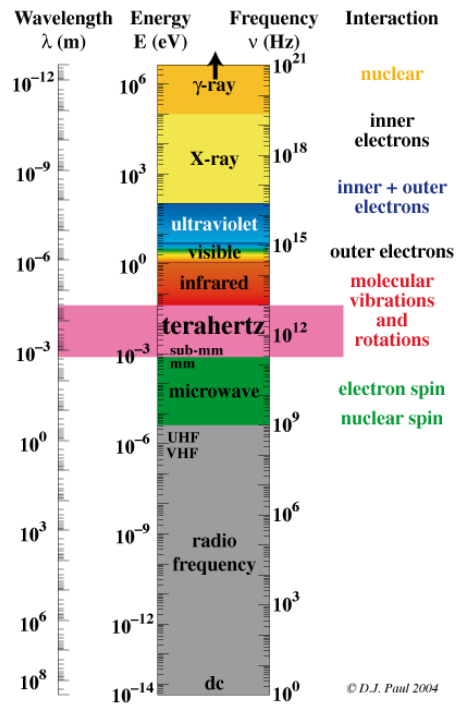


Figure 1.1 Spectral range of terahertz [1].

Because of the low absorption of THz by dry dielectric materials such as fabrics, papers, and plastics [2], there are applications for airport security screening and product inspection [3] [4]. The low photon energy is non-ionizing making it suitable for medical imaging of live tissues where commercial THz imagers are already available. The photon

energy overlaps with typical energies of vibrational/ rotational states in molecules, making it extremely useful for spectroscopy and chemical identification [4]. Molecules can be identified by distinct THz absorption lines. The THz radiation also provides a convenient probe of semiconductor carrier dynamics, e.g. Landau damping [5].

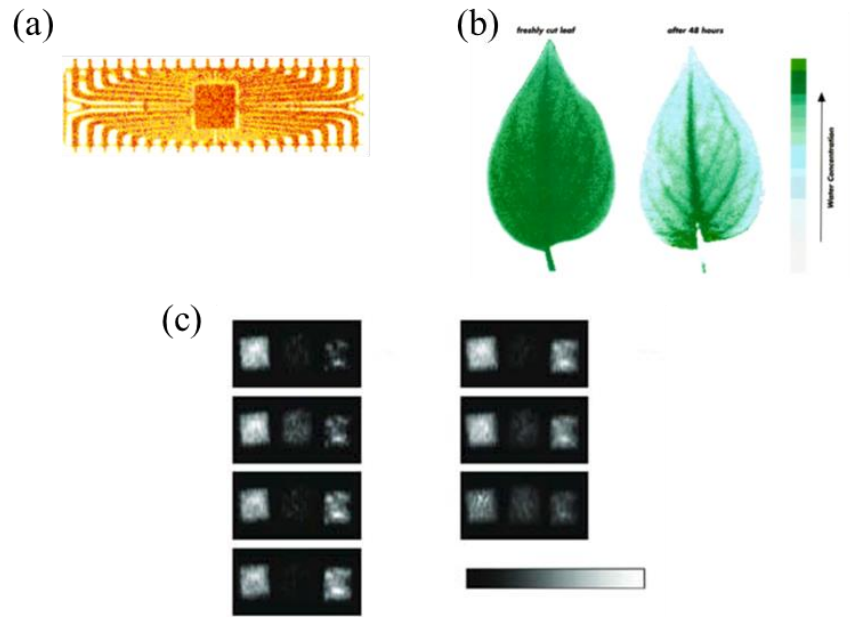


Figure 1.2 Examples of THz applications. THz raster imaging with photoconductive antenna [3] of (a) integrated circuit in plastic packaging, and (b) water contents in leaf. (c) Drug detection showing MDMA, aspirin, and methamphetamine (left to right) imaged at seven different wavelengths [4].

The topic of this dissertation is development of generation, point detection and imaging methods of broadband THz transients with the aim of using them for broadband THz spectroscopy of THz. A key contribution concerns the novel insight into the mechanism of THz generation via laser-induced plasma in gas [6] [7] [8], which is still a subject of scientific debate. The model described here considers the effect of dense plasma in the focal region to result in a spatially- and spectrally-coupled, non-uniform THz profile. The predicted features in the generation process are confirmed with a detailed experimental study. Next we develop a novel method of coherent detection of the generated THz transient. Our optically biased coherent detection technique removes the

need for an electrical high voltage requirement that has been used for some time in air-breakdown detection and even sold as a commercial product [9].

Finally, we present a study of alternate detection methods using THz-induced electro-absorption in semiconductors. In this method, the incident THz pulses induces changes in the absorption properties of the THz-biased semiconductor, which are then probed in transmission by an ultrafast probe pulse, resonant to the relevant interband transitions. Reliance on probe absorption drastically relaxes phase-matching requirements, and thereby promotes broadband operation of the detection method. Furthermore, it is shown that electro-absorption induced by a single-cycle THz pulse can be used for imaging. Observed features in the imaged THz profile are consistent with numerical simulations.

1.2. Dissertation outline

Following the introduction in the previous section, here we provide an outline of the rest of the dissertation:

Chapter 2 focuses on method of THz generation. A quick overview of current CW/pulsed THz generation mechanisms is given. Optical rectification and more importantly THz generation by laser-induced air-plasma are discussed in detail. Mechanisms of the above-mentioned two techniques are widely used, and detection of THz can be achieved by the reversal of mechanism. Finally, modeling of THz generation profile via laser induced air-plasma based on plasma current model is presented.

Chapter 3 concerns the first part addressing broadband THz detection. This chapter starts with an overview of existing THz detection techniques, which is followed by detailed descriptions of coherent THz detection by electro-optic sampling (EOS) and air-breakdown coherent detection (ABCD). Theoretical background, experimental result, and analysis of our purposed optically biased air-breakdown coherent detection technique (OBCD) are presented from Section 3.3 to 3.5.

Chapter 4 describes part two of broadband THz detection. This chapter focuses on observation of strong THz-induced electroabsorption in semiconductor structures. Experimental details, results and modeling are presented. The strong electroabsorption in semiconductors can be implemented in a THz detection scheme, which is further exploited as a THz imaging sensor in Chapter 5.

Chapter 5 demonstrates the two THz electroabsorption imaging techniques by treating semiconductor structures as either single pixel or large area detectors. THz profile at the generation is imaged and is found to be consistent with the prediction from Chapter 2.

Chapter 6 summarizes this dissertation and discusses the research outlook.

Chapter 2. Broadband THz generation

2.1. Method of THz generation

A common source of incoherent terahertz radiation is emitted in a process of black body radiation. Coherent terahertz source, however, must be engineered in the laboratory. Summarized below are some coherent THz sources categorized as continuous wave or pulsed.

Continuous wave (CW) THz sources:

- **Gas far-infrared lasers.** These are typically low-pressure gas lasers which operate on the rotational/ vibrational levels in gas molecules while pumped by CO₂ lasers. The typical lasing wavelengths are between 0.1-8 THz, tunable with composition/ pressure of the gas medium and pump frequency. CW power can be up to \approx 100 mW. The commonly used gas medium is methanol [10] [11].
- **Backward-wave oscillator (BWO).** This is vacuum tube with a metal corrugated structure. An electron beam propagating through it emits low frequency radiation in the backward direction [12]. Tunable output is typically achieved in the frequency range of 1 GHz -1 THz at power levels up to 100 mW [13].
- **Free electron laser (FEL).** Relativistic electrons traverse a periodic arrangement of magnets called undulator [14]. Transverse acceleration of the electrons produces monochromatic but incoherent synchrotron radiation. When the radiation is strong enough, electrons are modulated by the ponderomotive force and the radiation becomes coherent. Pulsed THz can also be generated when short pulses of electron beams are used.
- **Semiconductor far-infrared lasers.** Doped p-type germanium [15] and silicon [16] are biased and tuned by high electric and magnetic fields. The output power can

exceed 1 W and the maximum frequency is a few THz, making this laser of interest for imaging and spectroscopy. Cryogenic temperatures are required [17].

- **Quantum cascade laser (QCL).** The QCL was proposed by Kazarinov and Suris in 1971 [18] and eventually demonstrated in 1994 [19]. The QCL contains a superlattice formed by series of engineered heterostructures. A varying electric potential across the structure splits the conduction band into discrete electron subbands. In contrast to other semiconductor lasers that emit at the energy of the bandgap, the QCL radiates between electron subbands. The lasing wavelength therefore is engineered primarily by layer thickness. Operation typically requires substantial cooling, most often to cryogenic point.
- **Photomixing.** A photoconductive antenna (PCA) consists of a semiconductor surface with a pair of separated electrodes. An electrical bias voltage is applied across the gap and two overlapping optical beams illuminate it at frequencies ω_1 and ω_2 (Figure 2.1a), CW electromagnetic radiation is emitted at the beat frequency $\omega_b = \omega_1 - \omega_2$ [20] due to the created photo-current. By proper selection of ω_1 and ω_2 , PCA can efficiently radiate at THz frequencies [21]
- **Difference frequency generation (DFG).** Non-centrosymmetric crystals that exhibit a $\chi^{(2)}$ nonlinearity are potential candidates for DFG. Two CW laser beams of different frequencies incident upon nonlinear crystal results in the nonlinear polarization $P(\omega_1 - \omega_2) \propto \chi^{(2)} E_1(\omega_1) E_2^*(\omega_2)$ [22] at the THz frequency $\Delta\omega = \omega_1 - \omega_2$.
- **Frequency multiplication of microwave.** Microwave frequency up-conversion using voltage controlled oscillators or dielectric-resonator oscillators, such as Gunn/IMPATT diodes [2].

Pulsed THz sources:

- **Optical rectification.** OR is a second-order nonlinear effect [23] that mixes different frequency components of a wide-bandwidth femtosecond pulse. The low frequency

components typically result in the THz range, when generated with femtosecond pulses [24] [25].

Noncentrosymmetric crystals possess second-order nonlinearity $\chi^{(2)}$, the nonlinear response to the complex electric field $\tilde{E}(t) = Ee^{i\omega t} + c.c.$ is [22]:

$$\tilde{P}^{(2)}(t) = \varepsilon_0 \chi^{(2)} \tilde{E}^2(t) = \left[\varepsilon_0 \chi^{(2)} EE^* e^{i(\omega-\omega)t} + c.c. \right] + \left[\varepsilon_0 \chi^{(2)} E^2 e^{i2\omega t} + c.c. \right]. \quad (2.1.1)$$

The terms in the second bracket at frequency 2ω correspond to the process of second harmonic generation (SHG) of the incident field. The first bracket in Eq. (2.1.1) corresponds to the difference frequency generation (DFG) of the incident field. The DFG is the mixing of the monochromatic field with itself. It has zero frequency and is therefore results in a DC field within the crystal. This is referred to as optical rectification (OR). When a multi-cycle femtosecond pulse centered at ω is incident on the crystal, the DFG between the broad spectral contents within the pulse results in a nonlinear polarization at low frequency (terahertz). According to Eq. (2.1.1), the second-order polarization corresponding to the OR of an incident Gaussian pulse

$\tilde{E}_0(t) = E_0 e^{-4\ln 2 t^2/\tau_p^2} e^{i\omega t} + c.c.$ is:

$$\tilde{P}_{OR}^{(2)}(t) = 2\varepsilon_0 \chi^{(2)} E_0^2 e^{-8\ln 2 t^2/\tau_p^2}. \quad (2.1.2)$$

The resulting THz pulse width is hence comparable to that of the pump envelope (τ_p).

Other than the nonlinear coefficient, the amount of THz generated is influenced by phase mismatch [22]:

$$I_{THz} \propto L^2 \text{sinc}^2\left(\frac{\Delta kL}{2}\right), \quad (2.1.3)$$

where L is the length of the OR crystal and $\Delta k = k_1 - k_2 - k_\Omega$ is the wave vector mismatch due to dispersion in the crystal. Here ω_1 and ω_2 denotes the two frequency components in the pump, and Ω the frequency of THz. Perfect phase matching occurs when $\Delta k = 0$, and thereby $\frac{n_1\omega_1}{c} - \frac{n_2\omega_2}{c} = \frac{n_\Omega\Omega}{c}$. n_1 , n_2 , and n_Ω are the indices of refraction for ω_1 , ω_2 , and Ω frequencies, respectively. Using the Taylor expansion

$$n_2 = n_1 + (\omega_2 - \omega_1) \left. \frac{\partial n}{\partial \omega} \right|_{\omega_1} \quad \text{and} \quad \Omega = \omega_1 - \omega_2 :$$

$$\frac{1}{v_\Omega} = \frac{n_\Omega}{c} = \frac{n_1}{c} + \frac{\omega_2}{c} \left. \frac{\partial n}{\partial \omega} \right|_{\omega_1} \approx \frac{n_1}{c} + \frac{\omega_1}{c} \left. \frac{\partial n}{\partial \omega} \right|_{\omega_1} = \frac{\partial k_1}{\partial \omega_1} = \frac{1}{v_g}, \quad (2.1.4)$$

the condition of $\Delta k = 0$ is meet when the group velocity of the pump v_g is equal to the phase velocity of THz v_Ω . Since the *sinc* function peaks at $\frac{\Delta k L}{2} = 0$, Eq. (2.1.3) also indicates thin crystal is needed if broad generation bandwidth is desired. THz generation up to 100 THz has been demonstrated, although there are phonon resonances that add structures to the emission spectrum [26].

Typical nonlinear crystals used for OR include ZnTe [27], GaAs [24] [25], InP [28] [25], GaSe [29], and LiNbO₃ [30]. ZnTe, for example, is widely used because it is phase matched at 800 nm and therefore can be conveniently pumped with Ti:Sapphire lasers. Recently organic crystals such as DAST [31] [32], DSTMS [33] [34] and OH1 [35] [36] [37] possessing large second-order nonlinearities, have been developed for OR.

- **Photoconductive (PC) antenna.** This is similar to the two-beam CW technique except now a single femtosecond pump pulse with energy larger than the bandgap is used (Figure 2.1 (a)). The pulse is incident on the electrode gap and induces photocurrent transient. Energy stored in the gap due to the bias electric potential is released in the form of THz radiation [21]. The generation bandwidth is limited by carrier

lifetime, the RC time constant, and gate pulse duration [38] [39]. Shorter lifetime materials (sub-picosecond), such as low-temperature grown GaAs (LT-GaAs), doped silicon, radiation damaged silicon on sapphire [40], ErAs super lattices on GaAs substrate [41], and ion-implanted GaAs [42] [43] [44], are often selected for PC switches and antennas to increase the generation/ detection bandwidth. While high voltage bias could increase power and bandwidth, it is limited by the breakdown voltage of the material. Similarly, the optical pump power and pump aperture size are limited by thermal breakdown and carrier screening of the bias [45].

Various designs have been reported to increase generation bandwidth or power. A PC antenna with interdigitated MSM (metal-semiconductor-metal) electrodes has isolated metallization to mask every other electrode period from optical excitation. The photocurrent and hence THz emission between each pair of electrodes are constructively interfered [46] [47]. Examples of such antenna are shown in Figure 2.1 (b) and (c). Other solutions include trap-enhanced fields [48] [49] [50] and insulated RF bias [51].

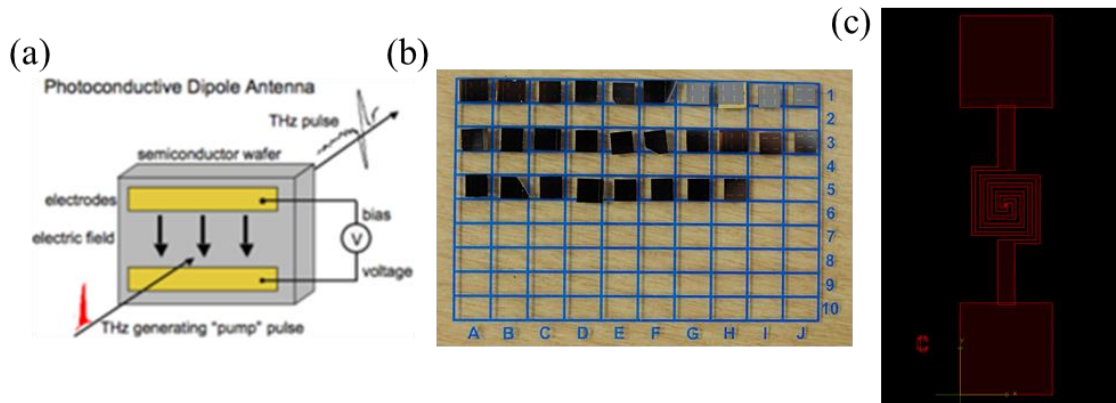


Figure 2.1 (a) Schematic of photoconductive antenna, (b) grown antennas without MSM, and (c) example antenna design. Antennas shown in (b) and (c) were grown by Dr. Jeffrey Cederberg at Sandia National Laboratory.

The large refractive index of the semiconductor severely limits the escape angle and coupling in to free space. A hemispherical lens, made from a transparent material such as high-resistivity silicon, is sometimes used to alleviate the problem.

- **Laser-induced air-plasma.** Generation of broadband terahertz by focusing femtosecond laser pulses in gas [52] [6] [7] [53] [8]; the laser driven photocurrent in gas plasma radiates THz and will be detailed in Section 2.2.
- **Photo-Dember.** Electron-hole pairs are created in a semiconductor by an ultrafast laser pulse with photon energy above the band-gap. Strong absorption near the surface causes an inhomogeneous distribution and steep spatial gradient into the bulk. Ambipolar diffusion of electrons and holes results in charge separation and a transient dipole field that can radiate a THz pulse [54] [55]. Relying on this mechanism, our group reported efficient THz generation using InAs nanowires [56]. A linear autocorrelation signal and corresponding spectrum of the THz emission from an array of spatially-ordered InAs nanowires are shown in Figure 2.2.

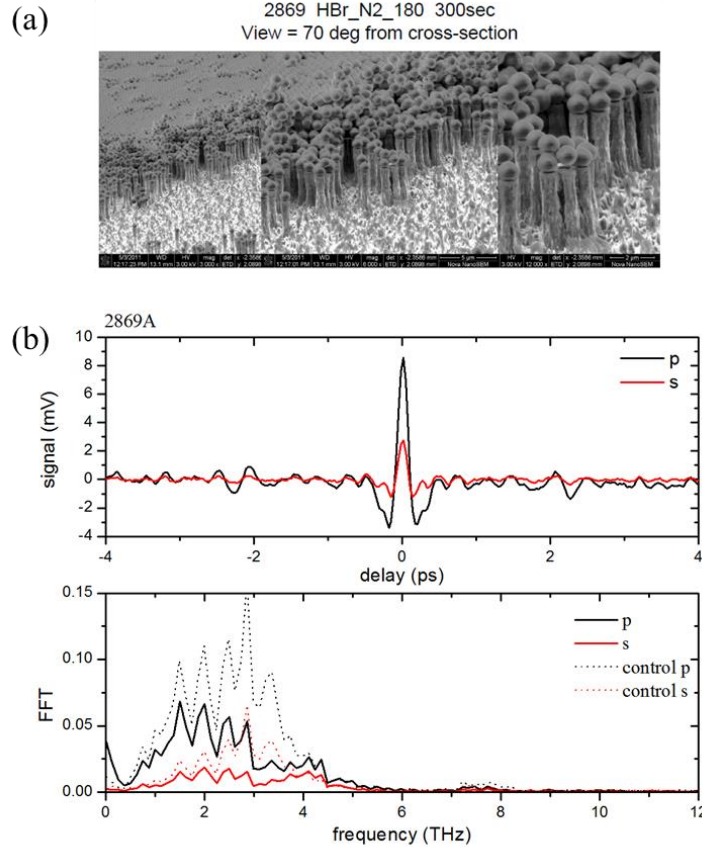


Figure 2.2 (a) Spatially-ordered array of InAs nanowires, grown using MOCVD by Dr. Jeffrey Cederberg at Sandia National Laboratory. (b) Linear autocorrelations (top) of the emitted THz are measured using bolometer for two orthogonal pump polarizations. Corresponding FFT spectra are shown below. Dotted lines represent control signal obtained from unstructured bulk InAs.

- **Built-in surface field.** The surface field of the semiconductor can drive dipole oscillations when electron-hole pairs are created by an optical pump. Screening of the surface field can also launch plasma oscillations in the bulk that can radiate into free space [2].

2.2. Broadband THz generation in gaseous medium

Recent years have seen an increasing amount of published work on the topic of THz generation from laser-induced plasmas in gas [52] [6] [7] [53] [8]. The field is proliferating due to the widespread availability of high-power, ultrashort pulse laser sources. The amount of THz power generated via optical rectification and photoconductive antennas is typically limited by material damage thresholds. This problem is absent in gas, which has now become an important source for broadband, high power THz pulses. Furthermore, relaxed phase-matching conditions promote substantially broader emission, with smooth spectra in the range from below 1 THz to several 10s of THz. Strong enhancement of the THz field strength was demonstrated by generating the plasma with two different laser frequencies [6] [7] [8]. In the simplest arrangement, the fundamental laser pulse centered at ω is focused into beta-barium borate (β -BBO) to generate a co-propagating beam at 2ω and focused in the gas (Figure 2.3). We estimate a THz field strength $> 1\text{MV/cm}$ in our two-color THz generation setup. It should be noted that THz can also be generated in plasma filament by Cherenkov radiation [57], resulting from ionized charge carriers moving in the wake of the pump pulse. In the following sections, the discussion focuses on the two-color gas plasma THz generation.

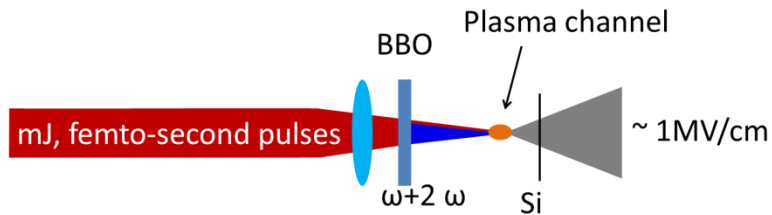


Figure 2.3 Experimental scheme for two-color gas plasma THz generation.

The mechanism was originally attributed to four-wave mixing process in air [6] [7], later literatures have shown experimental agreement [58] or disagreement [8] [59] [60].

In the four-wave mixing (FWM) picture, the nonlinear coefficient $\chi^{(3)}$ originates from the nonlinearity of air:

$$P_{THz} \propto \chi^{(3)} E_\omega^2 E_{2\omega} \cos \Delta\phi, \quad (2.2.1)$$

where E_ω and $E_{2\omega}$ are the amplitude of the time dependent electric field of the fundamental and second harmonic pulse $\tilde{E}_\omega = E_\omega(z, r) e^{i\omega t - ik_\omega z + i\phi_\omega} e^{-4\ln 2t^2/\tau_p^2} + c.c.$ and $\tilde{E}_{2\omega} = E_{2\omega}(z, r) e^{i2\omega t - ik_{2\omega} z + i\phi_{2\omega}} e^{-8\ln 2t^2/\tau_p^2} + c.c.$, respectively. P_{THz} is the resulting THz polarization. τ_p is the pulse width of the fundamental pulse. $\Delta\phi = 2\phi_\omega - \phi_{2\omega}$ is the relative phase between ω and 2ω .

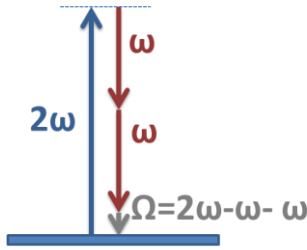


Figure 2.4 Energy level diagram for THz generation.

It has been pointed out that the known $\chi^{(3)}$ of air is too small to explain the magnitude of the generated THz [58]. The $\chi^{(3)}$ picture also predicts maximum THz generation at $\Delta\phi = 0$, which disagrees with the experimental results that show the THz yield approaches 0 at $\Delta\phi = 0$ [61]. The plasma current model proposed by Kim et al. explains the experimental results very well [61] [62]. In the next section, the model of the THz generation including spatial profile based on plasma current will be introduced.

2.3. Modeling THz generation

In this section, formalism for modeling of spatial and spectral aspects of the THz generation via air-breakdown two-color plasma is presented using the well-known plasma current model [61] [62]. The propagation of generated THz wave through air plasma,

including the effect of plasma dispersion and phase matching to the THz profile, is handled with electromagnetics.

In the plasma current model, THz occurs due to the polar asymmetry of the electric field [61] [62]. The large enhancement observed with two different pump frequencies is explained by a non-zero time average of this asymmetric field. The sum of fundamental and second harmonic co-polarized pump fields is $\tilde{E}(r, z, t) = \tilde{E}_\omega(r, z, t) + \tilde{E}_{2\omega}(r, z, t)$, which is clearly asymmetric for particular phase difference between the two fields ($\Delta\phi = 2\phi_\omega - \phi_{2\omega}$). We assume Gaussian spatial and temporal profiles for modeling purposes. For the spatial dependent amplitude $E_\omega(z, r)$ and $E_{2\omega}(z, r)$, Rayleigh range z_0 is taken to be same for both frequencies, while beam waist of 2ω pulse is $w_0 / \sqrt{2}$ (where $w_0 = \sqrt{\frac{2cz_0}{\omega_1}}$). A plot of such symmetric-broken field $\tilde{E}(t)$ with $\Delta\phi = \pi/2$ is shown in Figure 2.5(a).

The plasma photo current $\tilde{J}(t)$ resulting from the asymmetric field $\tilde{E}(t)$ is:

$$\frac{d\tilde{J}(t)}{dt} + \gamma_e \tilde{J}(t) = \frac{q^2}{m_e} \tilde{E}(t) \tilde{\rho}_e(t), \quad (2.3.1)$$

where γ_e is the collision frequency, m_e is the mass of electron, q is the electron charge, and $\tilde{\rho}_e(t)$ is the ionized carrier (electron) number density.

Ionization induced by intense laser fields can occur via two mechanisms, tunneling and multi-photon. With the applied external electric field, atomic ionization barrier can be lowered to induce tunneling process [63], and ionization can also be achieved by absorbing multiple photons [64]. The Keldysh parameter [65] is used to determine the dominating mechanism. The experimental condition of this dissertation correspond to the Keldysh parameter $\gamma = \sqrt{U_i / (2U_p)} = 0.13 < 1$, which makes tunneling the dominant ionization mechanism. The ionization potential is taken as $U_i = 15.58$ eV, which is the

ionization energy of nitrogen gas, $U_p = e^2 I / 2c\varepsilon_0 m \omega^2$ is the laser ponderomotive energy.

The ionization rate is:

$$\tilde{\rho}_e(t) = \rho_0 \left[1 - e^{-\int_{-\infty}^t \tilde{W}_t(t') dt'} \right], \quad (2.3.2)$$

where ρ_0 is the fully ionized number density estimated by ideal gas law and $\tilde{W}_t(t)$ is the tunneling ionization rate [63]:

$$\tilde{W}_t(t) = 4w_a \frac{E_a}{|\tilde{E}(t)|} e^{-\frac{2|E_a|}{3|\tilde{E}(t)|}}. \quad (2.3.3)$$

$w_a = me^4 / [(4\pi\varepsilon_0)^2 \hbar^3]$ is the atomic unit of frequency and $E_a = m^2 e^5 / [(4\pi\varepsilon_0)^3 \hbar^4]$ is the atomic unit of the electric field. Alternatively, the ionization can be modeled using Ammosov–Delone–Krainov (ADK) tunneling ionization rate [66]. Figure 2.5 (b) is a plot of $\tilde{\rho}_e(t)$, the step-like increase is due to the ionization buildup with each optical cycle of the multi-cycle femtosecond pump.

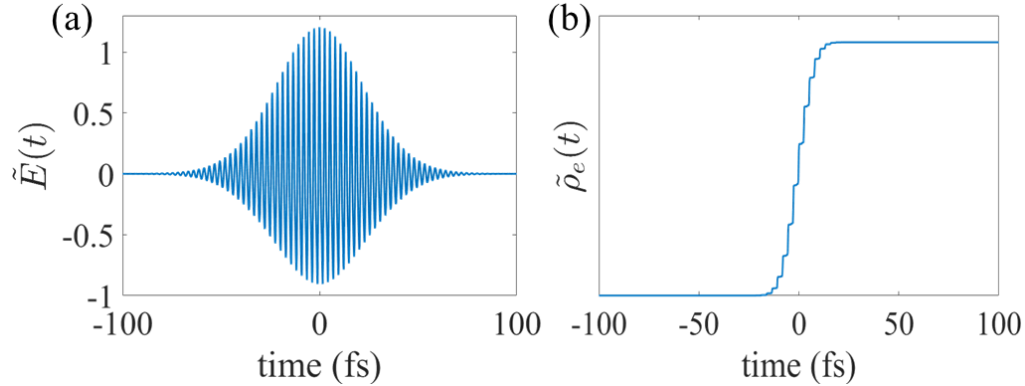


Figure 2.5 (a) polar-symmetry-broken two-color field $\tilde{E}(t)$, and (b) dynamics of the ionized charge density $\tilde{\rho}_e(t)$.

Taking Fourier transform of Eq.(2.3.1), the current density in frequency domain is

$$J(\omega) = \frac{q^2 \rho_0}{m_e} \frac{G(\omega)}{\gamma_e + i\omega}, \quad (2.3.4)$$

where $G(\omega) = FT \left\{ \tilde{E}(t) \tilde{\rho}_e(t) / \rho_0 \right\}$. ρ_0 is the fully ionized carrier density. In the case of fully ionized plasma ($\tilde{\rho}_e = \rho_0$), the corresponding plasma frequency ω_p is:

$$\omega_p = \sqrt{\frac{q^2 \rho_0}{m_e \epsilon_0}}. \quad (2.3.5)$$

Using Eq. (2.3.5) and $\tilde{J}(t) = d\tilde{P}(t) / dt$, where \tilde{P} is the polarization in time domain, the polarization in frequency domain, $P(\omega)$ is:

$$P(\omega) = \frac{J(\omega)}{i\omega} = -\epsilon_0 \frac{\omega_p^2}{\omega^2} \frac{G(\omega)}{1 - i\gamma_e / \omega}. \quad (2.3.6)$$

Figure 2.6 shows $|G(\omega)|$. We can separate the spectral components and designate THz, ω , 2ω , and n -th harmonic generation with P_{THz} , P_ω , $P_{2\omega}$, and $P_{n\omega}$, respectively.

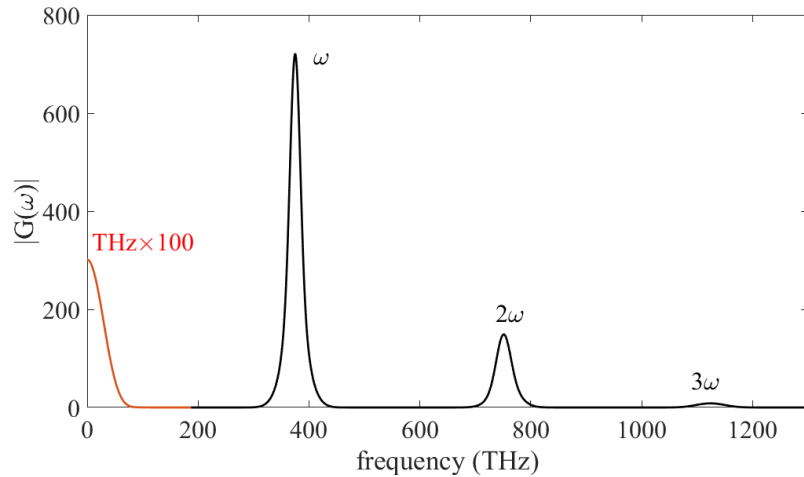


Figure 2.6 $|G(\omega)|$ in the numerical modeling, assuming 30% SHG conversion efficiency.

This model can then be used to optimize the emitted THz power. An important parameter is the relative phase $\Delta\phi$ between ω and 2ω . Figure 2.7 (a) shows the optimal phase between ω and 2ω for on-axis THz generation ($r=0$) at different ionization levels. The plotted lines are spectrally summed $|G(\omega)|$ to avoid the pole of $|P(\omega)|$ at zero frequency. The optimal phase $\Delta\phi$ is field strength dependent: it is less than $\pi/2$ when the field is strong enough to fully-ionize the air, and shifts away from $\pi/2$ with decreasing field strength. At lower field strength, the static tunneling ionization used in this modeling is no longer valid (Keldysh parameter is larger than unity).

Figure 2.7 (b) shows the corresponding plasma frequencies at each field strength, which is lowest at $\pi/2$. This is due to lowest ionization rate from the most asymmetric composite field. To illustrate this point, Figure 2.8 shows the plots of single-cycle $\tilde{E}(t)$, $\tilde{W}_t(t)$, and $\tilde{\rho}_e(t)$. The composite field is most temporally asymmetric at $\pi/2$, evident in when the gas is ionized (Figure 2.8 (c)). The ionization rate $\tilde{W}_t(t)$, however, is the lowest.

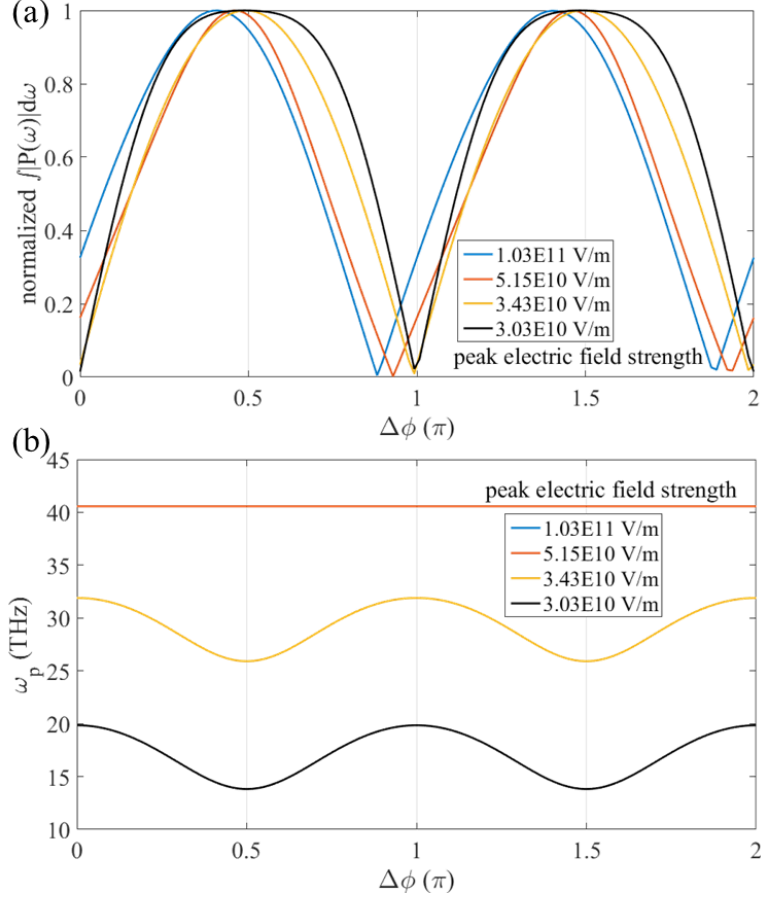


Figure 2.7 (a) On axis ($r=0$) THz polarization strength integrated over frequency versus relative phase $\Delta\phi$, calculated with 9 % SHG intensity ratio with respect to the fundamental field. The electric field strength for each line is shown in the legend. (b) Dependence of the plasma frequency on the relative phase due to the variation of ionization.

THz yield, on the other hand, is proportional to $P(\omega)$ (Figure 2.7 (a)). The drift velocity of the carrier $\tilde{v}_d(t) = -\frac{q}{m_e} \int_{t'}^t \tilde{E}(t) dt$ (where ionization occurs at $t = t'$) inherits

the temporal asymmetry of $\tilde{E}(t)$. This is where the sum of microscopic $\tilde{E}_{THz}(t) \propto q\tilde{v}_d(t) \frac{d\tilde{\rho}_e(t)}{dt}$ within the optical cycle raises due to the asymmetry [67], and

results in highest THz yield at $\Delta\phi = \pi/2$.

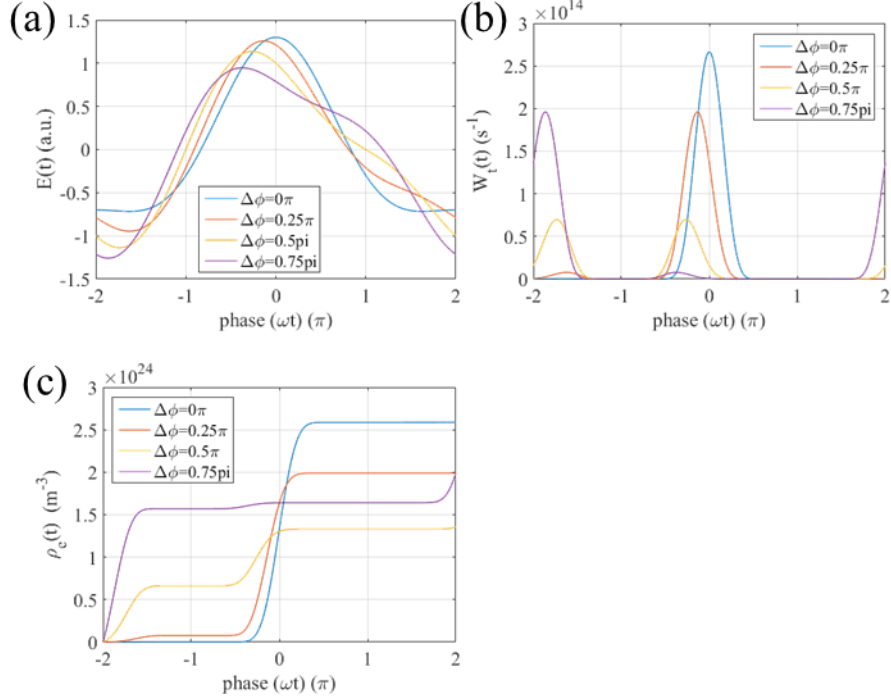


Figure 2.8 (a) single-cycle composite electric field $\tilde{E}(t)$, (b) ionization rate $\tilde{W}_t(t)$, and (c) ionized number density $\tilde{\rho}_e(t)$. Assuming peak electric field strength of 3.03E10 V/m.

The change of optimal phase at high field strength is related to the multi-cycle nature of the pump pulse. At high field strength, where the gas is eventually fully-ionized within the pulse duration, full ionization comes later in time at $\Delta\phi = \pi/2$ due to the lower degree of ionization. The total THz yield over the entire pulse duration is therefore lower. The effect of field asymmetry then further selects the optimal phase to be $< \pi/2$. One should note, for example, that $\tilde{E}(t, \Delta\phi = 0.25\pi)$ is not equal to $\tilde{E}(t, \Delta\phi = 0.75\pi)$ (Figure 2.8 (a)) because $\Delta\phi$ is $2\phi_{\omega} - \phi_{2\omega}$. While $\tilde{\rho}_e(\Delta\phi = 0.25\pi)$ and $\tilde{\rho}_e(\Delta\phi = 0.75\pi)$ are the same after one optical cycle (Figure 2.8 (c)), the time dependence originates from $\tilde{E}(t)$ determines the THz yield in the multi-cycle pump scenario.

Figure 2.9 shows the optimal phase with different amount of SH at field strength of 10.3E10 V/m. The shift in optimal phase can be contributed to variation of composite

field strength- the fundamental is kept same while SH changes with ratio in the simulation. Overall, the optimal phase is not dependent of the amount of SH field.

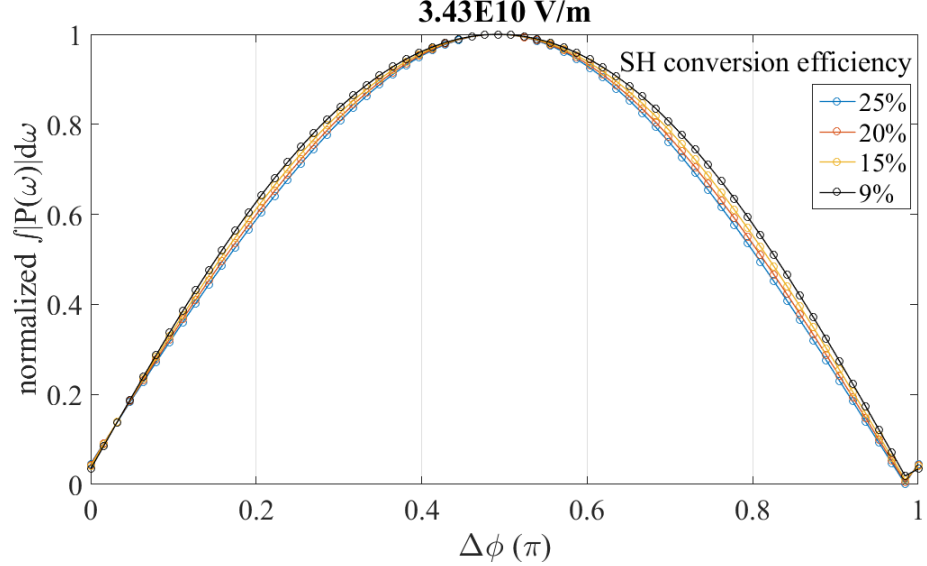


Figure 2.9 On axis ($r=0$) THz polarization strength integrated over frequency v.s. phase $\Delta\phi$ at various mixing of ω and 2ω .

The second part of the modeling includes the effect of THz propagation through air-plasma. Assuming all three beams (THz, ω , and 2ω) to be Gaussian, the wave equation is:

$$\frac{d^2 E(\omega, z, r)}{dz^2} = -\frac{\omega^2}{c^2} \left[\frac{P(\omega, z, r)}{\epsilon_0} + \epsilon(\omega) E(\omega, z, r) \right], \quad (2.3.7)$$

where $\epsilon(\omega)$ is the dielectric function for un-ionized gas that can be approximated as 1. For multi-cycle fundamental and second harmonic fields, Slowly Varying Envelop Approximation (SEVA) [68] can be applied to Eq.(2.3.7).

$$\begin{aligned} \frac{dA_\omega(\Omega - \omega, z, r)}{dz} &= -\frac{i\omega^2}{2k_\omega c^2} \left[\frac{P_\omega(\Omega - \omega, z, r) e^{ik_\omega z}}{\epsilon_0} \right] \\ \frac{dA_{2\omega}(\Omega - 2\omega, z, r)}{dz} &= -\frac{i\omega^2}{2k_{2\omega} c^2} \left[\frac{P_{2\omega}(\Omega - 2\omega, z, r) e^{ik_{2\omega} z}}{\epsilon_0} \right]. \end{aligned} \quad (2.3.8)$$

$E_\omega(\Omega, z, r) = A_\omega(\Omega - \omega, z, r)e^{-ik_\omega z} + c.c.$.and $E_{2\omega}(\Omega, z, r) = A_{2\omega}(\Omega - \omega, z, r)e^{-ik_{2\omega} z} + c.c.$. The solutions for $A_{\omega, 2\omega}$ are therefore just the integral over dz . For the single-cycle terahertz field $E_{THz}(\Omega, z, r)$, the SEVA is no longer valid, i.e. second derivative of $E_{THz}(\Omega, z, r)$ is non-vanishing. Substituting $E_{THz}(\Omega, z, r) = A_{THz}(\Omega, z, r)e^{-ik_{THz}(\Omega)z} + c.c.$ into Eq.(2.3.7), with $k_{THz}(\Omega) = \Omega\sqrt{\epsilon(\Omega)} / c$:

$$\frac{d^2 A_{THz}(\Omega, z, r)}{dz^2} - 2ik_{THz} \frac{dA_{THz}(\Omega, z, r)}{dz} = -\frac{\Omega^2}{c^2} \left[\frac{P_{THz}(\Omega, z, r)}{\epsilon_0} e^{ik_{THz} z} \right]. \quad (2.3.9)$$

$k(\Omega)$ can be calculated using plasma dispersion $\epsilon(\Omega) = 1 - \omega_p^2 / \Omega^2$ and spatial dependent $\omega_p(z, r) = \sqrt{q^2 \rho(z, r) / m_e \epsilon_0}$. $\rho(z, r)$ is the spatial-dependent ionized carrier density. The solution to Eq.(2.3.9) is:

$$A_{THz}(\Omega, z, r) = -\frac{\Omega^2}{\epsilon_0 c^2} e^{2ik_{THz} z} \int_0^z dz' \int_0^{z'} P_{THz}(\Omega, z, r) e^{ik_{THz}(z'' - 2z')} dz''. \quad (2.3.10)$$

To include the effect dispersion and self-phase modulation in plasma, the calculation should be carried out iteratively with the numerically computed $E_{\omega, 2\omega}(\omega, z, r)$ as the source field in Eq.(2.3.1). The effect of diffraction, due to finite numerical aperture of two off-axis parabolic mirrors in the experiment can be incorporated by convolving the THz profile with an Airy disk. The calculated radial-dependent THz profile at each frequency without iteration is shown in Figure 2.10. With the chosen spectral resolution there are 40 data points in the radial axis, limited by the amount of computer memory. The low THz frequencies are vanishing in the middle, due to the denser plasma that is non-propagating [60]. Periodical lines in the Airy disk-convolved profile is a numerical artifact due to limited amount of data points in Z, but overall the results indicates a broadened profile around the ring. In Section 5.3 we will show THz imaging of the generation point that agrees with Figure 2.10 (a). The THz beam is found tight enough not to be limited by aperture in our experiment. It should be noted that You et al. has also

reported similar beam structure, and explained it with off-axis phase matching condition [69].

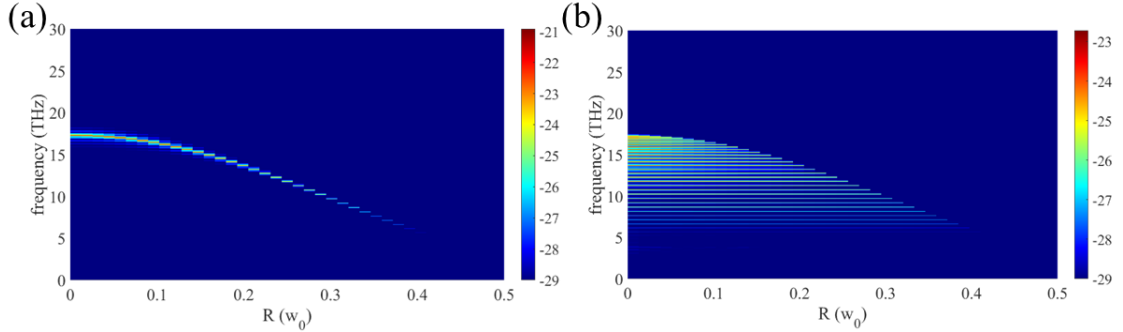


Figure 2.10 (a) Modeled THz profile, and (b) including diffraction from finite numerical aperture from off-axis parabolic mirrors. The z axis of the plot is $\log(\text{intensity})$.

To summarize this section, numerical modeling of the propagating THz profile shows a notable frequency-dependent spatial hole in the center due to plasma screening. Including a finite numerical aperture, the doughnut-shaped profile smears out due to convolution with the Airy disk. Future studies could image the frequency dependent profile with spectral filtering. Understanding how pump pulse parameters, such as chirp and SH ratio, affect generation could be beneficial for optimization. The plasma current model is not limited to co-polarized pumps so further studies of cross-polarized pump geometry could be beneficial.

Chapter 3. Broadband Terahertz Detection I

3.1. Methods of Terahertz Detection

Thermal detectors, such as bolometer, pyroelectric detector, and Golay cells are widely used for incoherent detection of THz. Bolometers [70] operate by measuring temperature-dependent electric resistance. Cryogenic cooled bolometers can achieve very high signal-to-noise ratio. A micro-bolometer thermal camera operates on the same principle with pixels made of thermal electric detector and an integrated readout circuit. Pyroelectric crystals [71] have permanent electric dipoles; a change of temperature at one surface leads to measurable current. A Golay cell [72] is a photo-acoustic device in which thermal expansion of the gas cell is measured optically. A disadvantage of thermal detectors is they are relatively slow ($>10\text{ms}$). They still have widespread application because they can be engineered to operate over large bandwidths. Figure 3.1 (a) compares the bandwidth of a pyroelectric detector (Gentec SPI-A-65THz) and liquid helium cooled bolometer (Infrared Laboratories) using THz FTIR. The THz is generated using the two-color air-breakdown plasma experimental setup that is described in Section 3.4. It is important to note that the bandwidth realized in a bolometer system is limited by input spectral filtering. The absorption lines in the power spectrum are due to water vapor absorption in air [73]. The effect of water vapor absorption can be alleviated with a nitrogen purge (Figure 3.1 (b)). In Chapter 4, we will demonstrate THz induced electroabsorption via Franz-Keldysh Effect (FKE), which is a promising technique for fast THz detection.

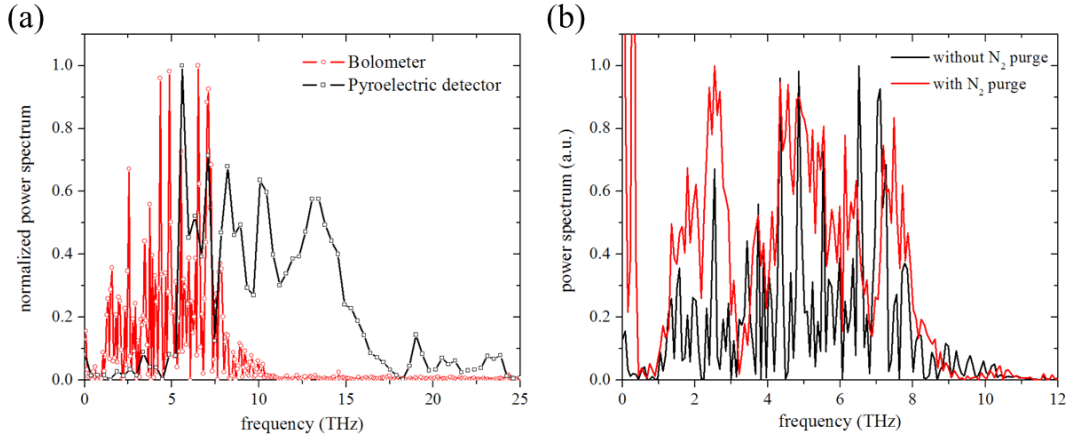


Figure 3.1 (a) Bandwidth comparison between pyroelectric detector (Gentec SPI-A-65THz) and bolometer (Infrared Laboratories). (b) Comparison between nitrogen purged (red) and unpurged measurements (black).

Time-domain THz detection is typically performed with a photoconductive switch [21] [74], Electro-Optic Sampling (EOS) [75], and more recently by Air-Breakdown Coherent Detection (ABCD) [76] [9]. All of these are essentially the reverse of a corresponding generation process.

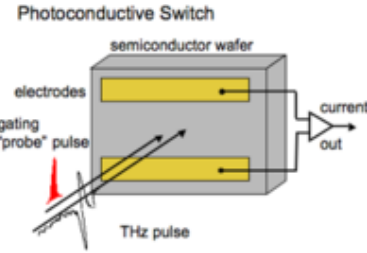


Figure 3.2 Schematic for THz detection using a photoconductive switch.

Detection of THz with photoconductive switch works very similar to the generation (Figure 3.2). Instead of a DC electric bias, the incident THz field is applied across the photoconductive gap and an optically gated photocurrent is measured at the electrodes. The current, however, cannot respond instantaneously to the THz field due to finite mobility of the charge carriers in the semiconductor. The measured signal is therefore a convolution between THz waveform and time dependent surface conductivity $\tilde{\sigma}_s(t)$ [40]:

$$\tilde{J}(t) = \int_{-\infty}^t \tilde{\sigma}_s(t-t') \tilde{E}_{THz}(t') dt' \quad (3.1.1)$$

Electro-optic sampling of an ultrafast THz pulse works via the linear electro-optic effect (Pockels effect):

$$P^{(2)}(\omega) = [2\epsilon_0 \chi^{(2)} E(0)] E(\omega), \quad (3.1.2)$$

in which the change of electrical susceptibility is linearly proportional to the applied DC field $E(0)$. To find the induced spatial polarization density components, we write the second-order susceptibility $\chi^{(2)}$ in tensor form, with i, j , and k denoting the Cartesian components:

$$P_i^{(2)}(\omega) = 2 \sum_{j,k} \epsilon_0 \chi_{ijk}^{(2)}(\omega, \omega, 0) E_j(\omega) E_k(0). \quad (3.1.3)$$

For $<110>$ oriented ZnTe crystal that is a widely used crystal for EOS crystal, phase-matching with large nonlinear constant d_{14} is achieved for optical probe at 800 nm (\vec{E}_ω) and THz (\vec{E}_{THz}) polarized in the $<1\bar{1}0>$ direction

$$(\vec{E}_\omega = \frac{E_\omega}{\sqrt{2}} \begin{pmatrix} 1 \\ -1 \\ 0 \end{pmatrix}, \vec{E}_{THz} = \frac{E_{THz}}{\sqrt{2}} \begin{pmatrix} 1 \\ -1 \\ 0 \end{pmatrix}) [77].$$

Eq. (3.1.3) is further simplified using Kleinman symmetry and spatial the symmetry of ZnTe crystal.

$$\begin{pmatrix} P_x \\ P_y \\ P_z \end{pmatrix} = 4\epsilon_0 d_{14} \begin{pmatrix} 000100 \\ 000010 \\ 000001 \end{pmatrix} \begin{pmatrix} E_{\omega,x} E_{THz,x} \\ E_{\omega,y} E_{THz,y} \\ E_{\omega,z} E_{THz,z} \\ E_{\omega,y} E_{THz,z} + E_{\omega,z} E_{THz,y} \\ E_{\omega,x} E_{THz,z} + E_{\omega,z} E_{THz,x} \\ E_{\omega,x} E_{THz,y} + E_{\omega,y} E_{THz,x} \end{pmatrix} = -4\epsilon_0 d_{14} E_\omega E_{THz} \hat{y}' \quad (3.1.4)$$

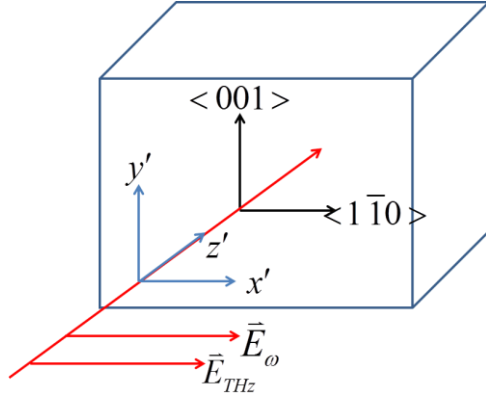


Figure 3.3 polarizations for EOS in $<110>$ ZnTe.

According to Eq. (3.1.4), the induced polarization density is linearly proportional to E_{Thz} in amplitude, but orthogonal to optical probe polarization. The total probe polarization becomes elliptical. EOS is usually experimentally setup with balanced photodiode to obtain a high signal-to-noise ratio [78]. As shown in Figure 3.4, the optical probe becomes circular polarized passing through the quarter wave-plate, after which it is split into two orthogonally polarized beams by a Wollaston prism. In this way the detector can be balanced for background-free detection. The signal detected is $\Delta I = I_0 \sin(\Delta\phi)$, where $\Delta\phi = \frac{\omega L}{c} n_\omega^3 d_{14} E_{Thz}$ [22]. The signal is approximately proportionally to $\Delta\phi$ and E_{Thz} , provided E_{Thz} is small enough; L is the crystal length and n_ω is the index of refraction at the probe frequency ω .

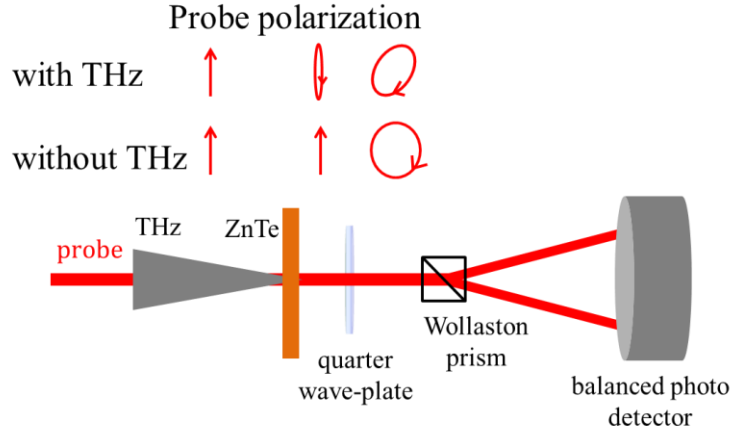


Figure 3.4 Schematic for electro-optic sampling with balanced detection.

Figure 3.5 shows experimentally measured THz transient with 0.5 mm $<110>$ ZnTe, THz source is optical rectification in ZnTe.

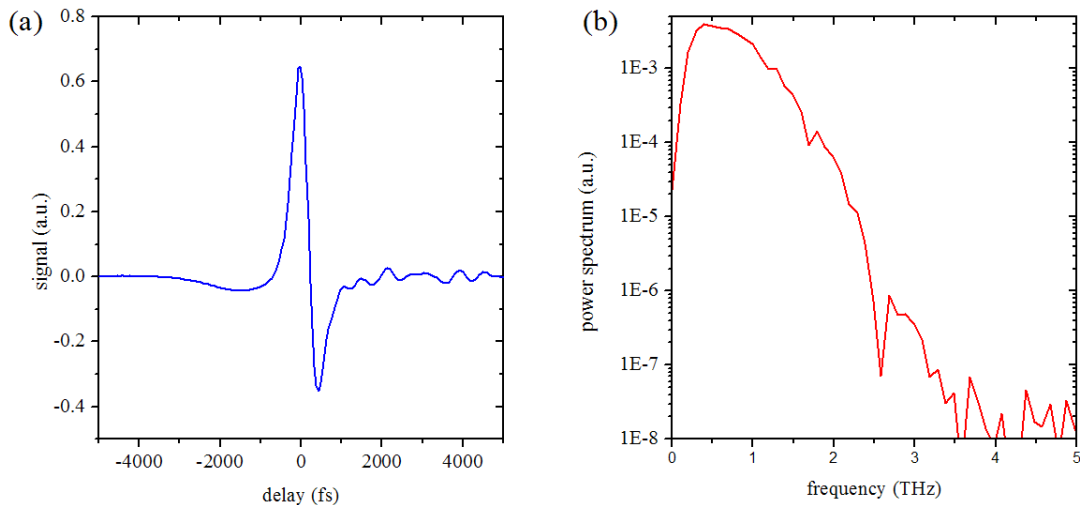


Figure 3.5 Experimental data of EOS with 0.5 mm ZnTe, the ultrafast THz source is derived from optical rectification with ZnTe.

The THz transient retrieved EOS can be distorted due to the finite probe pulse width, phase matching bandwidth (as discussed in Section 2.1), and dispersion in $\chi^{(2)}$ [40]. While a detection bandwidth up to 41THz was demonstrated with GaSe based EOS [79],

strong dispersion around the Restrahen band cannot be avoided. Air-Breakdown Coherent Detection is attractive because it does not suffer from Restrahen band absorption or catastrophic breakdown damage that occurs in solids. Linear THz electroabsorption in asymmetric quantum well structure [80] [81] indicate time domain spectroscopy of THz via electroabsorption is viable. In this chapter, we will present a modified ABCD technique and demonstrate that it is an all-optical detection scheme. In the following chapter, THz detection with electroabsorption in semiconductor structures is presented.

3.2. Air-Breakdown Coherent Detection

Broadband detection of THz by Terahertz Induced Second Harmonic (TISH) was first discovered in various materials [82] [83]. The recently reported Air-Breakdown Coherent Detection (ABCD) [76] [9] relies on detection of TISH as well. Although plasma current model [61] [62] is an accepted mechanism for generation, there are very few studies where it is used for detection [84]. One could argue that the generation process can always be reversed for detection and that is the approach implemented here.

TISH generation is modeled using the formalism in Section 2.3 with the addition of a DC field. When applied to TISH generation, there are the two key differences between four-wave mixing (FWM) and the plasma current model: saturation and optimal phase. The plasma current model predicts saturation of TISH generation resulting from complete ionization of available air molecules; such saturation does not exist in four-wave mixing. Figure 3.6 shows the calculated TISH polarization with increasing THz field strength. To demonstrate this saturation experimentally, very high THz field strengths are required, but the needed high intensity pulses cannot be generated in our laboratory. The plasma current model also predicts that the optimal phase difference between TISH and fundamental wave of $\pi/2$. The four-wave mixing picture, in contrast, requires that the fundamental, second harmonic, and TISH to be in phase.

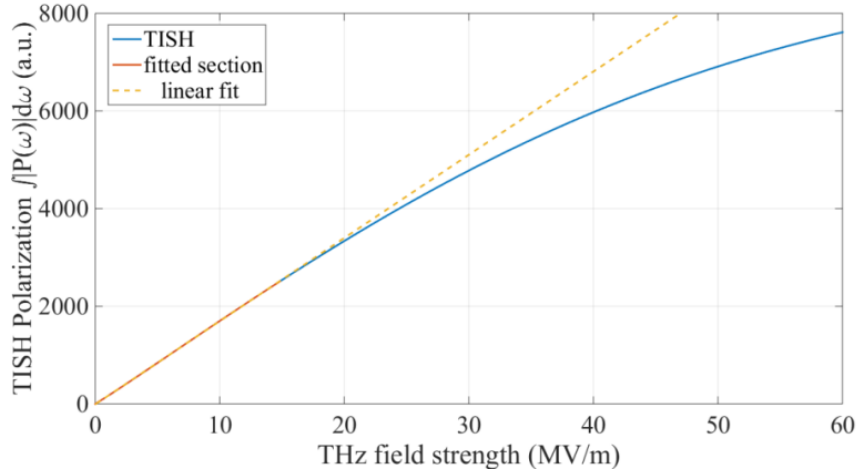


Figure 3.6 Calculated TISH generation v.s. applied THz field strength via plasma current model. An extrapolated linear fit of low field strength region (dashed line) illustrates the deviation at high fields.

TISH generation can be approximated by the four-wave mixing [6] [7] [8]. The $\Delta\phi = 0$ and $\Delta\phi = \pi$ in Figure 3.18 is labeled assuming the FWM process.

$$\tilde{I}_{TISH}(t) \propto |\chi^{(3)} \tilde{E}_\omega(t)^2 \tilde{E}_{THz}(t)|^2 \quad (3.2.1)$$

\tilde{I}_{TISH} is the intensity of TISH. $\tilde{E}_\omega(t) = E_\omega e^{i\omega t + i\phi_\omega}$ and $\tilde{E}_{THz}(t) = E_{THz} e^{i\Omega t}$ are the complex electric field of the fundamental and terahertz, respectively. The detected signal, which is a cross-correlation between probe ω and terahertz pulse, is:

$$\tilde{S}_{TISH}(\tau) \propto \int |\tilde{E}_\omega|^2(t+\tau) \tilde{E}_{THz}(t) dt. \quad (3.2.2)$$

As shown in above equation, detecting TISH along does not guarantee coherent detection because the intensity of TISH is proportional to the intensity of THz pulse. One could, however, interfere TISH with an additional field at frequency 2ω as first demonstrated by Dia et al. [76]. The source of 2ω field could come from local oscillator (LO), i.e. 2ω components in the plasma supercontinuum ($\tilde{E}_{LO}(t) = E_{LO} e^{i2\omega t + i\phi_{2\omega}} + c.c.$).

The total 2ω signal $\tilde{I}_{2\omega}$ is:

$$\tilde{I}_{2\omega} \propto \left| \chi^{(3)} \tilde{E}_{\omega}^2 \tilde{E}_{THz} + \tilde{E}_{LO} \right|^2 = \left| \chi^{(3)} \tilde{E}_{\omega}^2 \tilde{E}_{THz} \right|^2 + \left| \tilde{E}_{LO} \right|^2 + 2 \operatorname{Re} \left\{ \chi^{(3)} \tilde{E}_{\omega}^2 \tilde{E}_{THz} \tilde{E}_{LO}^* \right\}. \quad (3.2.3)$$

The measured time resolved cross-correlation signal in the ABCD experiment is:

$$\begin{aligned} \tilde{S}_{2\omega}(\tau) &\propto \int \left| \tilde{E}_{\omega}^2(t) \tilde{E}_{THz}(t+\tau) + \tilde{E}_{LO}(t) \right|^2 dt \\ &= \int \left[\left| \tilde{E}_{\omega}^2(t) \tilde{E}_{THz}(t+\tau) \right|^2 + \left| \tilde{E}_{LO} \right|^2 + 2 \operatorname{Re} \left\{ \tilde{E}_{\omega}^2(t) \tilde{E}_{THz}(t+\tau) \tilde{E}_{LO}^*(t) \right\} \right] dt, \end{aligned} \quad (3.2.4)$$

where τ is the delay between the probe ω and THz field. The second term can be experimentally excluded with lock-in detection while chopping the THz beam. The first term can be ignored when \tilde{E}_{LO} is large enough. Under these conditions, the measurable third term allows for coherent detection. With the requirement of a large LO field, high probe intensity is required to ensure coherent detection [76]. Further limitations of this method are the lack of independent phase and intensity control of the LO, which tracks the probe fundamental ω .

The same group latter reported a technique to generate the required 2ω by applying high DC voltage across the detection plasma (ABCD) [9]. The DC field breaks the centro-symmetry of the plasma, thus enables second harmonic generation of the field \tilde{E}_{LO} . This relaxed the requirement for a high intensity probe. High voltage electrode pairs placed orthogonally have been used for polarization reconstruction of the terahertz [85]. With sufficient long electrode pair, signal modulation in the third term of Eq. (3.2.4) due to phase-shift between ω and 2ω averages out, a precise phase control is therefore not necessary. The disadvantage of this approach is that the remote detection becomes problematic. In the next section, we introduce an all optical technique to supply the required local oscillator 2ω , and remove the requirement of high voltage bias.

3.3. Optically Biased Coherent Detection

The requirement of local oscillator for coherent detection of THz can also be satisfied by providing 2ω optically, which is implemented in experiment by inserting a β -BBO into the probe arm. The phase between \tilde{E}_{LO} and \tilde{E}_ω is therefore important since $\tilde{E}_\omega^2 \tilde{E}_{LO}^*$ in Eq. (3.2.4) is $E_\omega^2 E_{LO}^* e^{i\Delta\phi}$, where $\Delta\phi = 2\phi_\omega - \phi_{2\omega}$. Since E_{LO} is produced by second harmonic generation in β -BBO, $\tilde{E}_{LO}(t) \propto \tilde{I}_\omega(t)$ and the measured coherent signal is:

$$\tilde{S}_{2\omega}(\tau) \propto \cos(\Delta\phi) \int \tilde{I}_\omega^2(t) \tilde{E}_{THz}(t + \tau) dt. \quad (3.3.1)$$

The measured signal is sensitive to $\Delta\phi$, and the condition of $\Delta\phi = m\pi$ (m is an integer) is essential for sensitive coherent detection of a THz time signal. The coherence of this detection technique can also be studied experimentally by $\Delta\phi$ dependent $\tilde{S}_{2\omega}(\tau, \Delta\phi)$ response.

The benefit of this Optically-Biased Coherent Detection (OBED) is the removal of the external high voltage bias. Bias supplied by a light pulse further allows for polarization/ phase control and convenient stand-off detection setup. Supplying high voltage bias electrodes at remote location is certainly problematic.

3.4. OBED Experimental setup

The experimental setup consists of two arms, one arm generates THz source via air-breakdown plasma and the other arm generates the detection plasma required for ABCD. THz generation via optical rectification in ZnTe can be implemented in the generation arm instead, for experiments that require less field strength. The laser source is a 40fs Ti:Sapphire amplifier (Coherent Legend Elite) with pulse energy $\approx 3.5 \mu\text{J}$. The central wavelength is around 800 nm, and repetition rate is 1 kHz. The amplifier is seeded with a conventional, home-built mode-locked Ti:Sapphire oscillator with 88 MHz repetition rate

and $\approx 500\text{mW}$ mode-locked average power. To further ensure an optimal and consistent pulse as close to transform limited as possible, a femtoFit pulse shaper is employed (see Appendix A). The amplifier output is split into two experiment arms by an ultrafast 50-50 beam splitter (Newport).

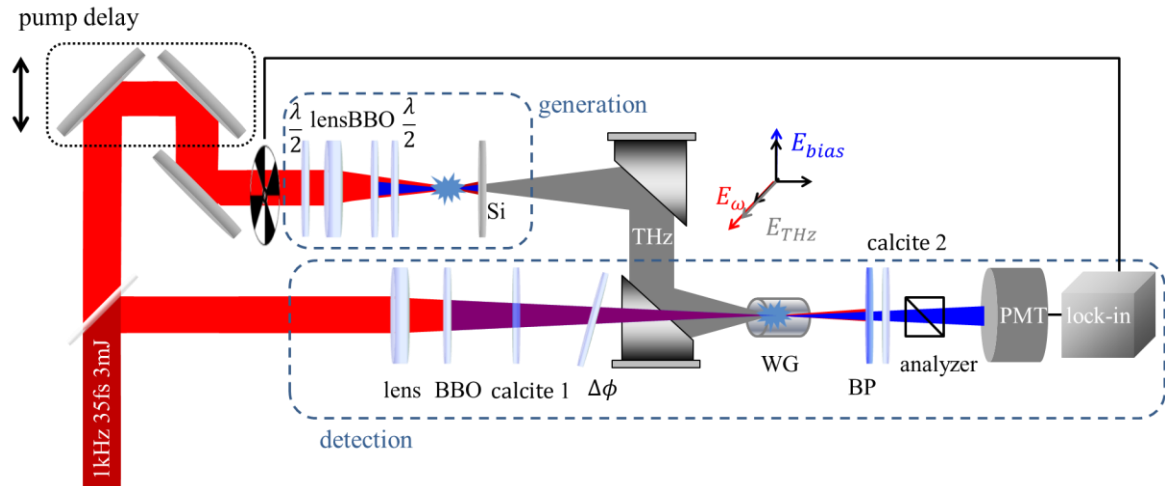


Figure 3.7 Schematic of OBCD experimental setup

In the THz source arm, beam first passes through an ultrafast zero-order half wave plate (HWP, Newlight Photonics WPS02-H-800-AR800/400 $\approx 45\ \mu\text{m}$) for polarization matching purposes and focused by a 12.5 cm lens (Thorlabs BK7 lens LA1986-B, B-coated BK7). The focused beam passes through a 30 μm -thick type-I beta-Barium Borate (β -BBO) crystal that generates second-harmonic wavelength required for two-color plasma THz generation with p-polarization. The fundamental beam is then rotated to p-polarization for optimal THz generation by another zero-order HWP.

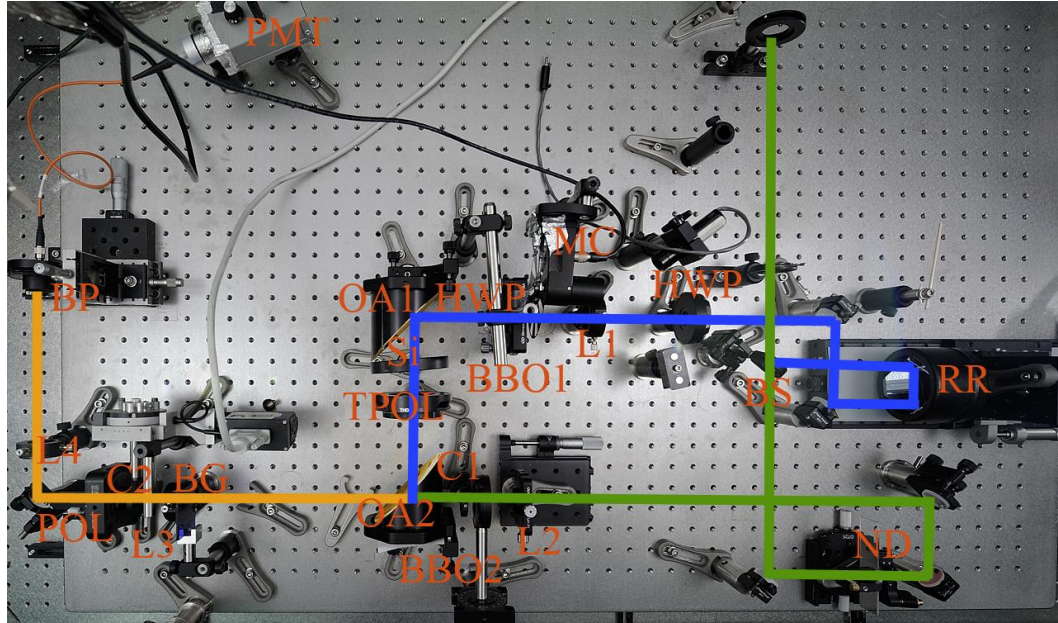


Figure 3.8 photo of OBCD experimental setup (waveguide and its 3-axis translation stage is not shown here).

The optimal phase between ω and 2ω for THz yield is 0.5π (section 2.4). This condition is attained by moving the BBO position along beam propagation direction. The phase control is possible due to the dispersion in the air for the two frequencies, e.g. propagation in 25.9 mm of air results in relative phase shift of π .

The THz beam generated by the two-color plasma interaction is collimated and refocused on the detection plasma by a set of 3-inch gold coated off-axis parabolic mirrors (Edmund Optics NT63-200 and NT63-199. $f=76.2$ mm and 50.8 mm, respectively). Residual pump light (ω and 2ω) is absorbed by a 0.5 mm high resistivity Silicon wafer (MTI <100> HR-Si, 3" diameter x 0.5 mm. 2 sides polished, N-type undoped) placed between two off-axis parabolic mirrors (OAPMs). THz polarizer (TYDEX HDPE polarizer, 63 mm open aperture) could be place in between the two OAPMs to pass only p-polarized THz. However, the TISH generated by a THz polarized orthogonal to probe fundamental is negligible, so this is not necessary. Experimental results with and without the polarizer show no difference other than a small amplitude change. For lock-in detection, an optical chopper blade (Thorlabs MC2000 with MC1F10

chopper blade) is inserted between the focusing lens and BBO crystal. Alternatively, we can chop THz directly with a two-slot blade (MC1F2).

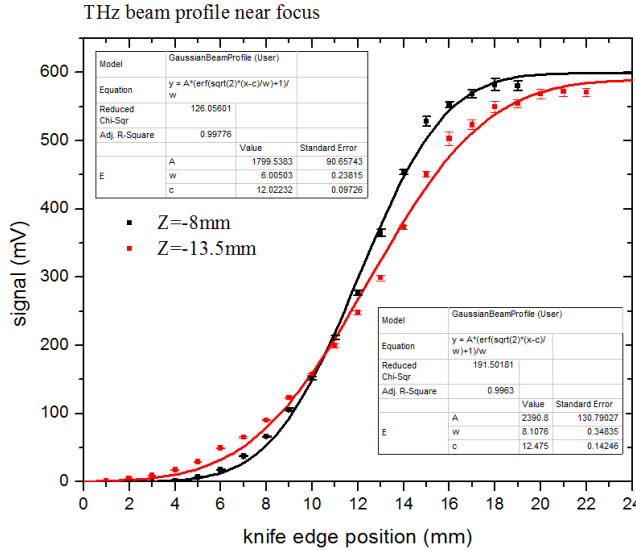


Figure 3.9 Knife-edge measurements of THz spot sizes at two different positions.

THz beam waist size w_0 was estimated with knife-edge experiment. Two spot sizes were measured at different positions to calculate w_0 (Figure 3.9). The estimated w_0 for 1 THz is about 150 μm . With an additional THz power measurement from pyroelectric detector (Gentec SPI-A-65THz), the estimated peak THz field is $\approx 1 \text{ MV/cm}$.



Figure 3.10 Metallic waveguide. Waveguide is glued to a post that is mounted on a 3-axis translation stage.

In the detection arm, the probe is attenuated to ≈ 50 nJ by reflective metal neutral density (ND) strip. A 17.5 cm lens (Thorlabs LA1229-B, B-coated BK7) is used to focused the probe beam through a 10 μm -thick type-I β -BBO (Newlight BTC10010-SHG800(I)-P), that generates the optical bias \tilde{E}_{LO} . The optical bias pulse is temporally shifted ahead of the fundamental probe pulse by a 500 μm calcite plate (Newlight CAL1200-A). This arrangement has the advantage of avoiding possible cross-phase modulation induced by the detection plasma. The group delay dispersion induced by 3mm-long fully-ionized plasma is estimated to be only 6.4 fs², which is negligible. The calcite pair can thereby provide phase control, as described later in this section. The temporal shifts between \tilde{E}_{LO} and \tilde{E}_{TISH} as they propagate through optical elements are detailed in Table 3.1. The focusing optical bias and probe pass through a hole in the center of the THz-focusing OAPM, and at their focal point produce a weak detection plasma in spatial overlap with the focusing THz.

	\tilde{E}_{LO} (s-pol.)	\tilde{E}_{TISH} (p-pol.)
500 μm Calcite	-252.17 fs	N/A
20 cm Air+10 μm BBO +FS wedge pair	+(61.20+X) fs	N/A
200 μm Calcite at normal	+133.47 fs	+10.20 fs
total	(-57.50+X) fs	+10.20 fs

Table 3.1 Temporal displacement of \tilde{E}_{LO} and \tilde{E}_{TISH} relative to the probe fundamental ω after passing each optical element. Positive numbers represent that ω leads in time. BBO crystal with 1mm fused silica substrate is assumed. X is the amount contributed from fused silica wedge pair (Eq. 3.4.3). If used without fused silica wedge pair, rotation of 200 μm calcite plate is needed to increase the effective thickness, thus bringing \tilde{E}_{LO} and \tilde{E}_{TISH} in temporal overlap.

Since the spectral and spatial THz profile from the plasma is not uniform [86] [69], a 5-mm long silver coated stainless steel cylindrical waveguide of inner diameter $< 200 \mu\text{m}$ (Figure 3.10) is placed near the focus to improve phase matching of the probe pulse with THz frequencies of large k vector [87]. The mounted waveguide is attached to a 3-axis translation stage for position fine tuning.

THz waveguides can be used in THz time-domain spectroscopy to measure thin films or gas [88]. In such experiments, THz source and detector are coupled to both ends of the waveguide, with the material interrogated placed inside the hollow waveguide [89]. The circular and rectangular hollow waveguide were found to exhibit strong group velocity dispersion and loss in the THz regime [90] [88] [89]. Other THz waveguides, such as plastic ribbon [91] and unclad sapphire fiber [92], are capable of single mode operation, but also display strong dispersion.

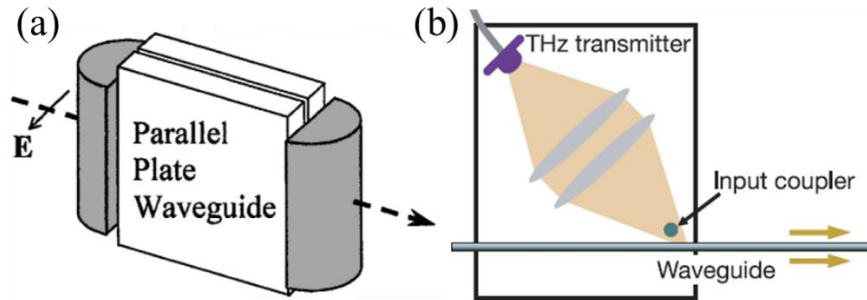


Figure 3.11 Schematics for (a) the parallel plate THz waveguide with coupling cylindrical lens on both ends [93], and (b) the metal wire THz waveguide [94].

Single mode (TM_0) propagation of broadband THz field, which is polarized perpendicular to the plates, has been demonstrated in the copper parallel plate waveguides [93] with low dispersion and loss. Intriguingly, a simple metal wire waveguide also exhibits low loss and dispersion in THz regime [94]. Since the metal wire waveguide operates in a radial TM mode, coupling linearly polarized THz field into the wire is inefficient. In Figure 3.11 (b), another metal wire perpendicular to the waveguide is utilized as the input coupler. Studies have shown that the coupling efficiency can be increased by using conical metal wire waveguides [95], or a radial symmetric

photoconductive antenna as the THz source [96]. For our OBCT experiment, the co-propagation of the optical probe and TISH along with THz pulse is essential; therefore the hollow circular waveguide is the only viable choice.

Using a circular metallic waveguide over the two-color generation plasma was theoretically studied by Babushkin et. al. [87]. The plasma current is used for modeling the generation, and THz waveform propagated through the argon-filled, aluminum-coated hollow waveguide was calculated. The linearly polarized EH₁₁ mode shows strong absorption under 11THz (Figure 3.12 (a)), as well as strong dispersion < 250 THz (Figure 3.12 (b)). For the optical pump pulses, the loss is small but there is a slightly broadening [87].

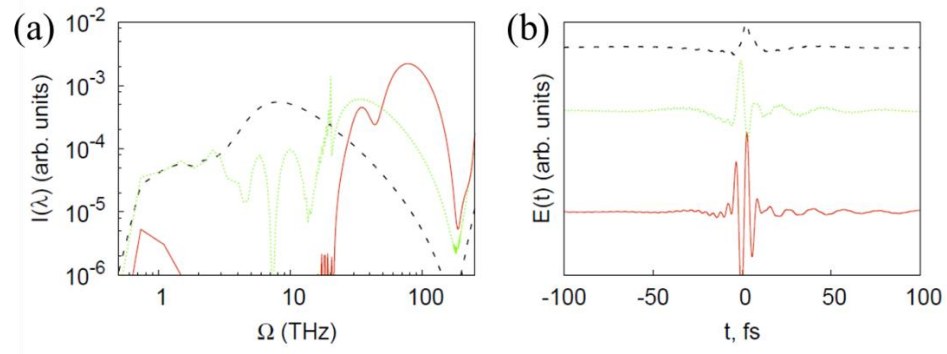


Figure 3.12 Transmission of a hollow metallic wave guide with inner diameter of 100 μm [87]. THz source originates from a two-color plasma. The 10 fs pump pulse consists of 10^{14} W/cm^2 and $2 \cdot 10^{13} \text{ W/cm}^2$ intensity of fundamental and second harmonic wave, respectively. (a) Spectra of the propagated THz in log scale, and (b) the waveform of the propagated THz ($< 250 \text{ THz}$) components. Propagation distance of 0.5, 2, and 10mm are represented with black dashed, green, and red lines, respectively.

While we still call it a waveguide in our experiment, we do not rely on its THz wave guiding capability, but instead use it to confine the optical probe and THz wave for the generation of TISH. The intention is to increase the overlap between the optical probe and the THz wave, which divergence is frequency dependent. Since the waveguide we

used is similar to the one studied by Babushkin et. al. [87], we argue that due to the strong loss, the contribution to TISH generation from the propagated and distorted THz wave is small. Currently we have limited waveguides available in our lab, and modeling of the waveguide we used is prevented by lack of accurate waveguide parameters, due to manufacturing limitations. However, for future studies, it would be of great interest to design and fabricate a waveguide structure that is optimal for the detection process.

After passing through the plasma, the diverging TISH and optical bias are re-collimated by a 20 cm calcium fluoride lens (Thorlabs LA5714). The collimated beams then pass through a 200 μm calcite plate (Newlight CAL12002-A) to bring them into temporal overlap. Since the polarizations are orthogonal, a Glan-Thompson polarizer is can conveniently select the amount of optic bias. The polarizations of fundamental E_ω , second harmonic optical bias \tilde{E}_{LO} , and THz \tilde{E}_{THz} are shown in Figure 3.13.

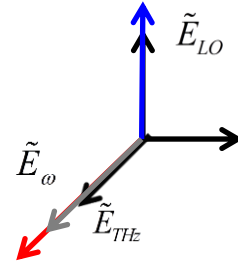


Figure 3.13 Polarizations of \tilde{E}_ω , \tilde{E}_{LO} , and \tilde{E}_{THz} .

As mentioned in Section 3.4, the condition of $\Delta\phi = 0$ is critical for accurate THz time trace measurement. $\Delta\phi$ can be controlled by various ways in our experiment. The simplest method is to use a thin AR-coated fused silica (thickness: 100 μm or 250 μm) phase plate after the 10 μm -thick BBO (Newlight photonics FSG10010-AR800/400 or FSG10025-AR800/400). Tilting of the phase plate introduces optical path length difference between \tilde{E}_{LO} and \tilde{E}_ω that translates into phase difference (Figure 3.14):

$$\Delta\phi = \frac{2\pi d}{\lambda_{2\omega}} \left[\left(\frac{n_\omega}{\cos \theta_\omega} - \frac{n_{2\omega}}{\cos \theta_{2\omega}} \right) - \sin \theta_0 (\tan \theta_\omega - \tan \theta_{2\omega}) \right] \quad (3.4.1)$$

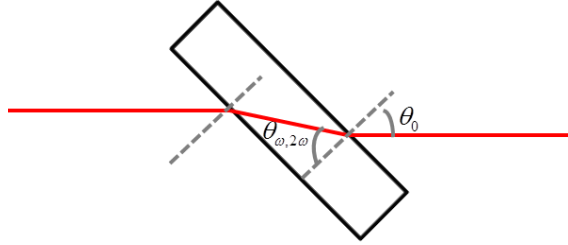


Figure 3.14 Schematic of phase control using phase plate.

Here $\lambda_{2\omega}$ is the wavelength of 2ω , θ_0 is the incident angle, n_ω and $n_{2\omega}$ are the refractive indices of fused silica at ω and 2ω , respectively. θ_ω and $\theta_{2\omega}$ are the refractive angles of ω and 2ω inside fused silica phase plate, respectively. In Eq. (3.4.1), $\Delta\phi > 0$ means ω lags in time. The disadvantages of using phase plate are the introduction a global time delay as $\Delta\phi$ changes due to increase of optical path length, and also a parallel spatial shift $\Delta x_{\omega,2\omega}$ due to finite thickness of the phase plate:

$$\Delta x_{\omega,2\omega} = d \sin \theta_0 (1 - \cot \theta_0 \tan \theta_{\omega,2\omega}). \quad (3.4.2)$$

This parallel shift leads to reduced overlap of probe and THz and manifests as a reduction of signal as the phase plate rotates. Since THz spectral profile is not uniform, it would also introduce experimental error in $\tilde{S}_{2\omega}(\tau, \Delta\phi)$ measurement.

The second method involves a pair of fused silica wedges (FemtoLasers OA924, 30mm x 20mm, Figure 3.15), in place of the phase plate. Changing the wedge insertion varies $\Delta\phi$ according to:

$$\Delta\phi = \frac{2\pi \tan \alpha_w \Delta x}{\lambda_{2\omega}}, \quad (3.4.3)$$

where α_w is the wedge angle and Δx is the change in vertical insertion. The advantage of using wedge pair is that while the beam does shift vertically, the amount of shift does not change due to constant distance between the two wedges. Changing the insertion amount, however, still introduce global delay as does the phase plate.

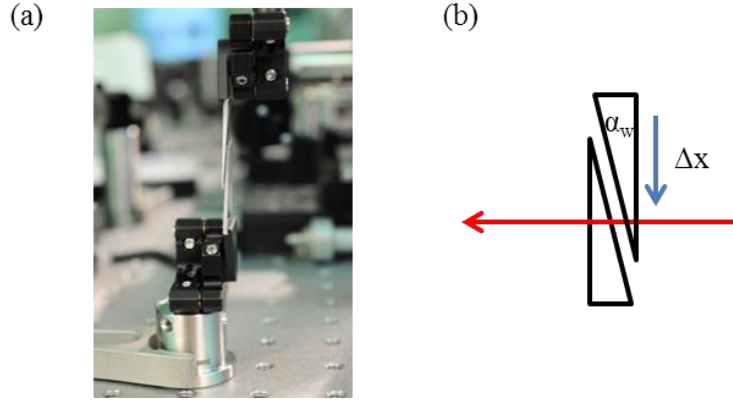


Figure 3.15 Fused silica wedges pair. (a) photo and (b) schematic.

The third method is to rotate the 200 μm -thick calcite plate around the optical axis (Figure 3.16). Rotation around the optical axis does not change the index of refraction for the p (extraordinary, \tilde{E}_{TISH}) or s (ordinary, \tilde{E}_{LO}) polarized beam, but changes the effective optical path for both. The time delay between the two when brought into overlap is therefore controllable. The change of phase relative to normal incidence scenario is in the same form as Eq. (3.4.1):

$$\Delta\phi = \frac{2\pi d}{\lambda_{2\omega}} \left[\left(\frac{n_{2\omega,o}}{\cos \theta_{2\omega,o}} - \frac{n_{2\omega,e}}{\cos \theta_{2\omega,e}} \right) - \sin \theta_0 (\tan \theta_{2\omega,o} - \tan \theta_{2\omega,e}) \right]. \quad (3.4.4)$$

Here we assume \tilde{E}_{LO} and \tilde{E}_{TISH} are both centered at 2ω . $n_{2\omega,o}$ and $n_{2\omega,e}$ are ordinary and extraordinary index of refraction of calcite, respectively. $\theta_{2\omega,o}$ and $\theta_{2\omega,e}$ are the refractive angle inside calcite of \tilde{E}_{LO} and \tilde{E}_{TISH} , respectively. Since the rotation is done after the detection plasma, the distinct advantage of this method is that it does not

change the global delay or the probe-THz overlap. Experimentally, the 200 μm calcite plate is mounted on a motorized rotational stage for better precision.

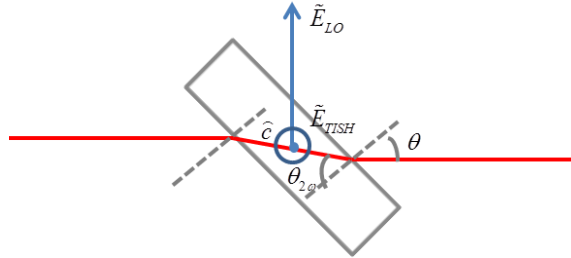


Figure 3.16 Schematic for phase control using calcite plate.

A measurement of TISH spectrum versus THz-probe delay is performed using a simplified setup shown in Figure 3.17. An Ocean Optics HR4000 USB spectrometer is used in this experiment. Data is taken with a Labview program which automatically records multiple spectra at each delay to improve signal-to-noise ratio through averaging. The reason why this measurement is performed is discussed in Section 3.5.

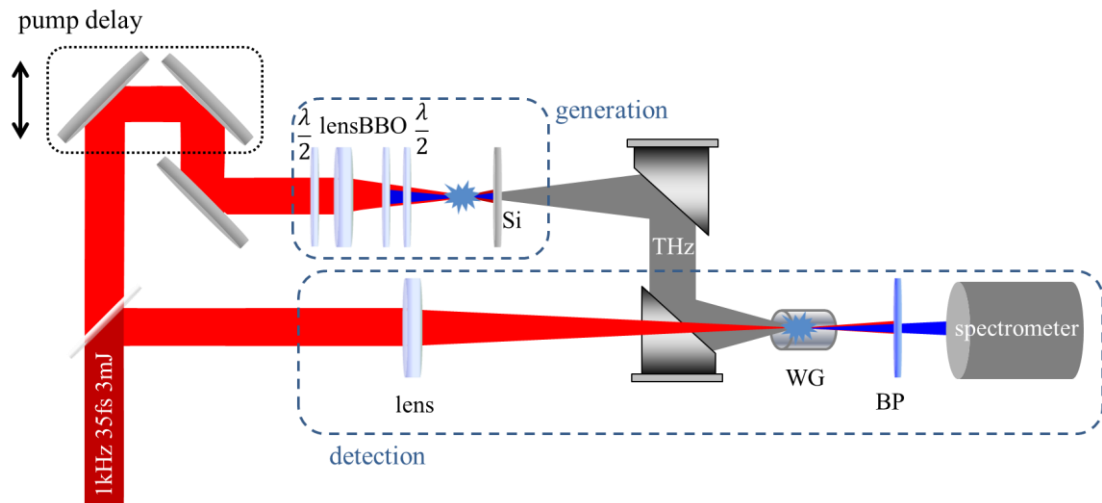


Figure 3.17 Schematic for delay dependent TISH spectra measurement.

3.5. OBCD results and discussion

A typical time trace for a THz pulse generated by two-color air-breakdown plasma and measured by OBCD is shown in Figure 3.18 (a), detection bandwidth reaches up to 15 THz as shown in Figure 3.18 (b). The THz pulse has a fast raising peak that decays to a valley at a slower rate. The persistent oscillation at longer delay is due to free-induction decay of water vapor in ambient air [97]. It disappears in a nitrogen-purged setup. The result is multiple dips in linear spectrum (Figure 3.18 (b)). The coherence of this detection technique is also demonstrated in Figure 3.18 (a) by the almost perfect flip of signal when $\Delta\phi$ is changed by π . The slight difference of peak amplitude is attributed to the time domain sampling resolution and the accuracy of $\Delta\phi$ ($\Delta\phi$ is derived from corresponding phase control scheme).

The signal-to-noise ratio (S/N) for the data presented in Figure 3.18(a) is around 40, with 100ms time constant on the lock-in amplifier, a 370 Hz mechanical chopper frequency, and averaging over 3 time traces. Assuming 0.7 MV/cm of peak field strength we had available when this experiment was performed, the minimum detectable peak field strength is 17.5 kV/cm. In comparison, EOS claimed minimum field sensitivity of 1 V/cm [75], and about 0.5 to 1 kV/cm for ABCD [9] (estimated from data presented). The reason for relatively low S/N in OBCD is that the coherent signal is measured on top of a large background (optical bias), and the saturation of the detector becomes the limiting factor. The S/N can be further improved by lowering the injected 2ω just enough to avoid detection saturation yet held high enough to render incoherent term negligible for linear detection. This requires substantial modification of the experiment, including separate, independent generation of optical bias from the probe pules.

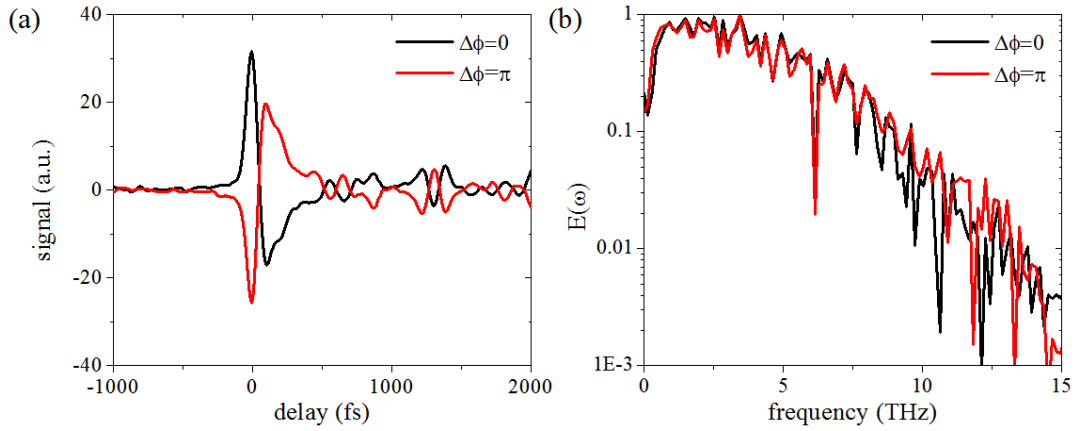


Figure 3.18 (a) OBCD time trace demonstrating coherent detection; the signal inverts when $\Delta\phi = \pi$. (b) Corresponding spectrum $E(\omega)$.

To verify the four-wave mixing picture and linear detection of OBCD are valid within our experimental parameters. The peak TISH signal versus THz power and peak OBCD signal versus THz field amplitude are plotted in Figure 3.19. Both follow the expected scaling, i.e. with intensity and field amplitude, respectively. THz power is attenuated by additional HR Si wafers placed between the pair of off-axis parabolic mirrors, and measured by pyroelectric detector.

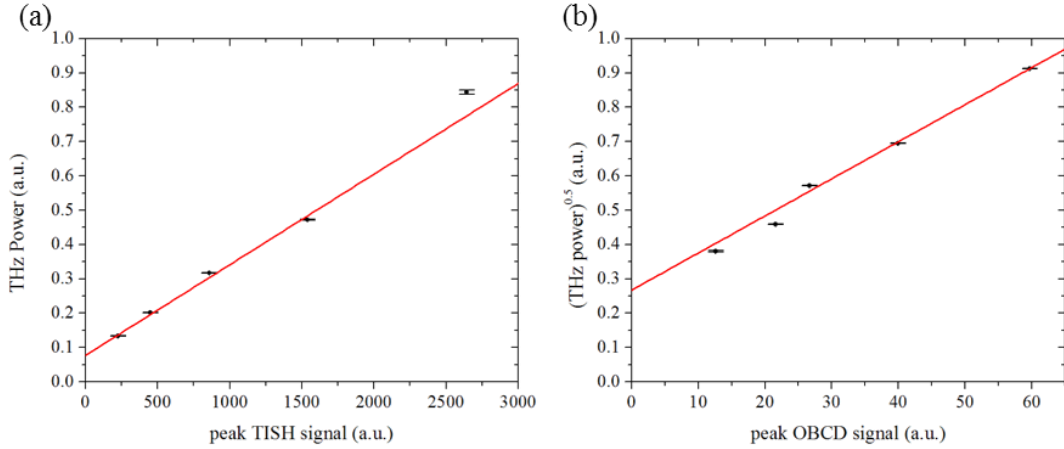


Figure 3.19 (a) TISH peak signal v.s. THz power, (b) OBCD peak signal v.s. THz field strength.

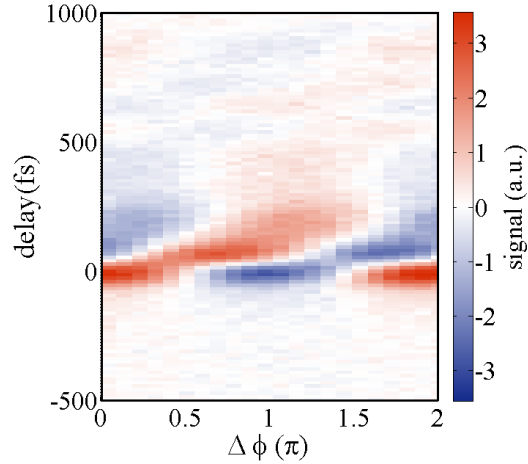


Figure 3.20 Measured OBCD signal $\tilde{S}_{2\omega}(\tau, \Delta\phi)$.

A typical phase dependent OBCD signal $\tilde{S}_{2\omega}(\tau, \Delta\phi)$ is plotted as a surface map in Figure 3.20. The expected signal nodes is missing, i.e. at $\Delta\phi = (m+1)\pi / 2$ (m is an integer), the signal approaches zero as suggested by Eq. (3.3.1). For comparison, the expected surface map is plotted in Figure 3.24 (a). The lack of nodes can be explained by two factors: shift in central wavelength of the TISH (away from 2ω) and finite probe duration. On a side note, Gouy phase dependence of the signal in the case of high voltage ABCD with thin electrodes has been reported [98]. The lack of nodes is also evident in the data presented.

To explain this unexpected feature, we first measure the peak wavelength of the TISH spectrum versus delay. This measurement is performed immediately before the acquisition of the phase dependent OBCD response (Figure 3.20). The data shows that the central wavelength of TISH redshifts ≈ 4 nm in the main peak portions of the THz transient. (Figure 3.21). Figure 3.21 (b) shows the integrated spectrum as a function of delay, which is THz pulse intensity temporal profile.

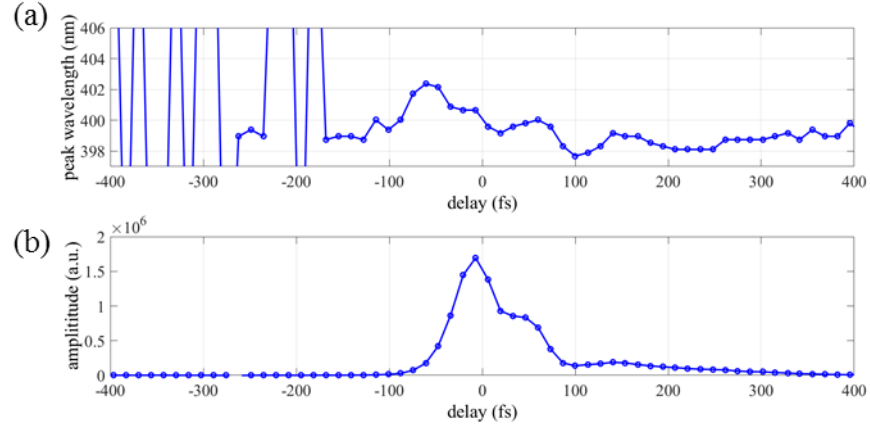


Figure 3.21 (a) TISH spectral peak v.s. delay, peak of bias $2\omega \approx 397$ nm. (b) Integrated TISH signal v.s. delay.

The redshift can be explained by phase matching of tightly focused Gaussian beams [22] [60]. In the forward propagation scenario, TISH generation consists of two possible paths: $\omega_{TISH}^{\pm} = 2\omega \pm \omega_{THz}$ (Figure 3.22 (a)). To calculate the phase matching condition, one needs to include the plasma dispersion. Plasma dispersion from Drude model is used here:

$$n = n_{air} \sqrt{1 - \omega_p^2 / \omega^2} \quad (3.5.1)$$

$$\omega_p = \sqrt{\frac{n_e e^2}{m_e \epsilon_0 n_{air}}} \quad (3.5.2)$$

n_{air} is the refractive index of air, which is taken to be 1. Wavelength λ is in the unit of μm . ω_p is the plasma frequency, and n_e , e , m_e , and ϵ_0 are number density of electron, electric charge, mass of electron, and permittivity of free space, respectively. The propagation of THz through plasma is forbidden or heavily damped when $\omega < \omega_p$, so transparency only occurs at partially-ionized spatio-temporal regions of the plasma [60]. To estimate the phase matching condition, plasma frequency ≈ 1.3 THz is used, in consistent with the absent of low frequencies in the measured OBCD spectrum. The

calculated phase mismatch $\Delta k = k_{2\omega} - 2k_\omega - k_{THz}$ for ω_{TISH}^+ and ω_{TISH}^- frequencies is shown in Figure 3.22 (c). Angular phase matching is also possible when $\Delta k < 0$ ($\omega_{TISH}^- = 2\omega - \omega_{THz}$) (Figure 3.22 (b)). The angular phase matching angle, which is within the converging angle of the probe beam in our experiment, is shown in Figure 3.22 (d). The calculation shows that $\omega_{TISH}^- = 2\omega - \omega_{THz}$ is the favored process [99].

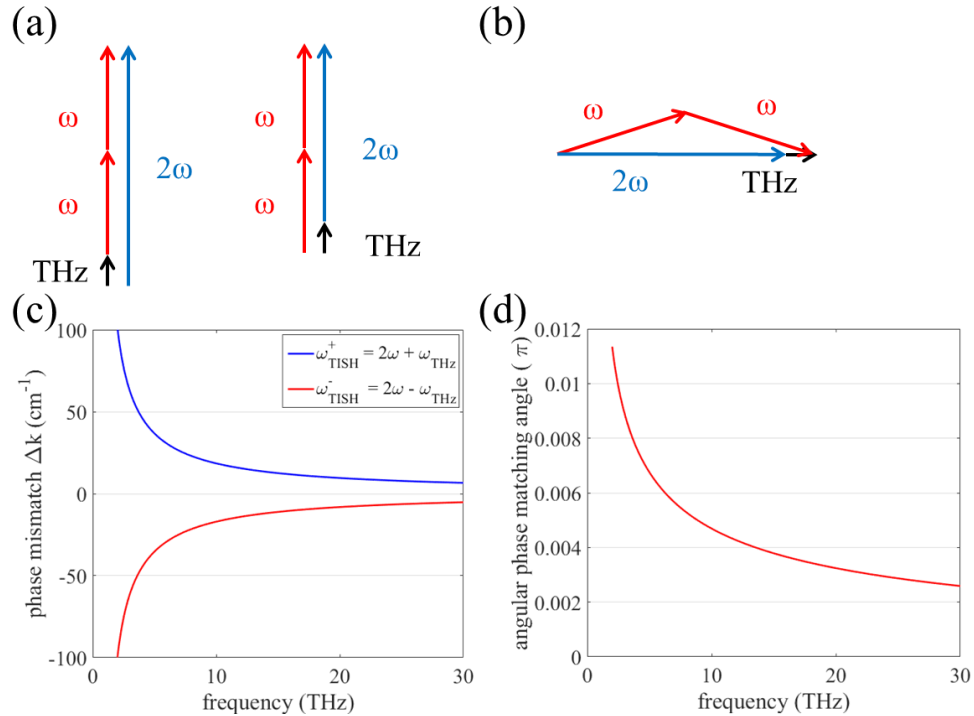


Figure 3.22 (a) Wave vector diagram for the two possible processes of the TISH generation. (b) Angular phase matching for $\Delta k < 0$. (c) Calculated phase mismatch vs frequency for ω_{TISH}^+ and ω_{TISH}^- , assuming plasma frequency of 1.3 THz, and (d) angular phase matching angle for the $\Delta k < 0$ case.

The TISH spectrum of tightly focused Gaussian beam can be calculated using the formalism described in Ref. [99] and Ref. [22]. Starting from wave equation and making the slowly varying envelop approximation:

$$2ik_{TISH} \frac{\partial A_{TISH}}{\partial z} + \nabla_T^2 A_{TISH} = -\frac{4\pi\omega_{TISH}^2}{c^2} p_{TISH} e^{i\Delta kz}, \quad (3.5.3)$$

with A_{TISH} and p_{TISH} being the spatial varying part of complex electric field and polarization density (i.e. $E_{TISH}(2\omega) = A_{TISH}(r, z)e^{i2\omega t}$ and $P_{TISH}(2\omega) = p_{TISH}(r, z)e^{i2\omega t}$), respectively. $\nabla_T^2 = \frac{1}{r} \frac{\partial}{\partial r} (r \frac{\partial}{\partial r}) + \frac{1}{r^2} \frac{\partial^2}{\partial \varphi^2}$ is the transverse Laplacian in cylindrical coordinate and $\Delta k = k_{TISH} - 2k_\omega - k_{THz}$ is the phase mismatch. Assuming the process $\omega_{TISH}^- = 2\omega - \omega_{THz}$ and $p_{TISH}(r, z) = \chi^{(3)} A_\omega(r, z)^2 A_{THz}^*(r, z)$, the solution for Eq. (3.5.3) can be found by using the trail solution:

$$A_\omega(r, z) = \frac{A_\omega}{1 + iz/z_R} e^{-r^2/w_0^2(1+iz/z_R)}, \quad A_{TISH}(r, z) = \frac{A_{TISH}(z)}{1 + iz/z_R} e^{-2r^2/w_0^2(1+iz/z_R)}$$

$$\text{, and } A_{THz}(r, z) = \frac{A_{THz}}{1 + iz/z_T}. \quad (3.5.4)$$

, where z_R and z_T are the Rayleigh length of the fundamental and THz, respectively. w_0 is the beam waist of the fundamental. A_ω and A_{THz} are the amplitude of the fundamental and THz, respectively. Radial dependence of THz is ignored because its beam waist is much larger than that of the optical frequencies. The TISH spectrum can be calculated using:

$$A_{TISH}(z) = \frac{i4\pi\omega}{n_\omega c} \chi^{(3)} A_\omega^2 A_{THz} \int_{-\infty}^{\infty} \frac{e^{i\Delta kz'} dz'}{(1 + iz'/z_R)(1 - iz'/z_T)}$$

$$= \frac{i8\pi^2\omega}{n_\omega c} \chi^{(3)} A_\omega^2 A_{THz} \frac{z_R z_T e^{i\Delta kz_T}}{z_R + z_T} \quad (3.5.5)$$

Calculated TISH spectrum assuming 8 THz pump pulse, using the above-mentioned formalism is presented in Figure 3.23.

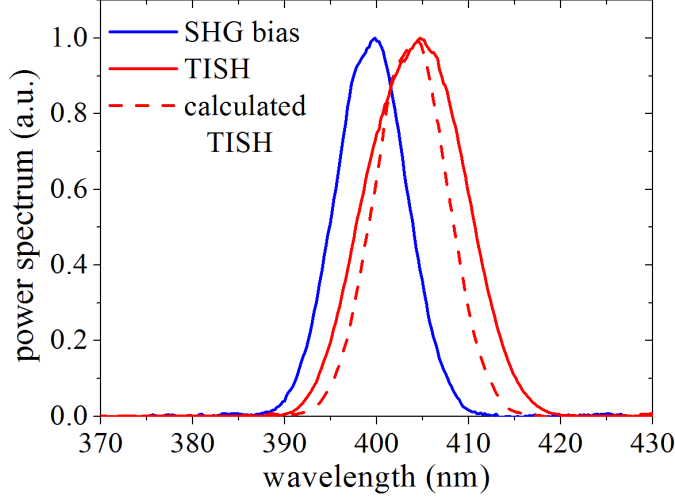


Figure 3.23 Measured (solid line) and calculated (dashed line) TISH and measured bias SH spectra at zero delay. Phase-matching is considered for 8 THz. The redshifted TISH spectrum demonstrates the dominance of the $\omega_{TISH}^- = 2\omega - \omega_{THz}$ process.

To include the combined effect of wavelength shift and finite probe pulse width, the cross term in Eq. (3.2.3) can be rewritten as:

$$2\chi^{(2)}\chi^{(3)} \operatorname{Re}\left\{\tilde{I}_\omega^2(t)\tilde{E}_{THz}(t+\tau)e^{i(\Delta\omega t + \Delta\phi)}\right\} \quad (3.5.4)$$

using the fact that $\tilde{E}_{LO} \propto \chi^{(2)}\tilde{I}_\omega(t)$ and $\tilde{E}_{TISH} \propto \chi^{(3)}\tilde{I}_\omega(t)\tilde{E}_{THz}(t+\tau)e^{i\Delta\omega t}$, where τ is the delay between probe and THz. $\Delta\omega$ is the difference in frequency between injection 2ω and ω_{TISH} . $\tilde{I}_\omega(t) = |\tilde{E}_\omega^2(t)|$ is the intensity of the fundamental pulse. The experimentally measured coherent component is:

$$\tilde{S}_{2\omega}(\tau, \Delta\phi) \propto \int \tilde{I}_\omega^2(t)\tilde{E}_{THz}(t+\tau)\cos(\Delta\omega t + \Delta\phi)dt. \quad (3.5.5)$$

The effect of finite probe pulse duration manifest itself as the fact that $\tilde{E}_{THz}(t+\tau)$ cannot be taken outside of the integral, and the shift in TISH central frequency produces additional phase $\Delta\omega t$. As the consequence, the phase-dependent OBCD response

$\tilde{S}_{2\omega}(\tau, \Delta\phi)$ no longer approaches to zero at some $\Delta\phi$. Therefore the nodes expected in the $\tilde{S}_{2\omega}(\tau, \Delta\phi)$ are absent, as shown in Figure 3.24 (a).

Theoretical modeling is presented in Figure 3.24. The OBCD measured THz waveform (Figure 3.18 (a)) is used in this calculation. Figure 3.24 (a) shows the expected experimental result without TISH spectral shift. Figure 3.24 (b) shows the simulation assuming a constant 4nm shift in central wavelength across the entire time delay and 36fs probe pulse width. The numerically simulation (Figure 3.24 (b)) agrees well with the experimental data (Figure 3.20). Minor discrepancy away from the zero-delay is attributed to the assumption of constant TISH spectral shift, which is not avoidable in numerical simulation.

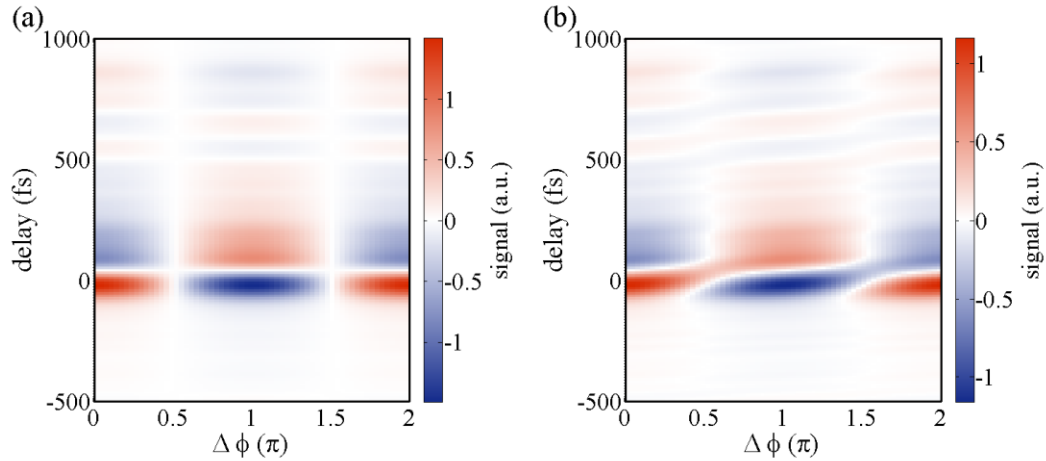


Figure 3.24 Numerically modeled OBCD signal $S_{2\omega}(\tau, \Delta\phi)$. (a) No deviation of TISH central wavelength from injection wavelength, and (b) with 4 nm shift in TISH central wavelength.

Linearity of the detection shown in Figure 3.19, can be addressed using numerical modeling. With the four-wave mixing picture, one expects infinite linearity in OBCD. The plasma current model, presented in Section 2.3, predicts differently about OBCD linearity.

In our experimental geometry, 2ω is moved ahead of the probe pulse in time. We therefore model TISH generation with a single color field (\tilde{E}_ω) plus a DC field. The polarization of TISH can be found in the numerically calculated $P(\omega)$, as described in Eq.(2.3.6). The plasma current model shown in Figure 3.25 predicts TISH saturation at THz field strength above 15 MV/cm. For future works, it would be interesting to look for a deviation from linearity at this THz field strength, which would serve as further experimental verification of the fundamental mechanism behind TISH.

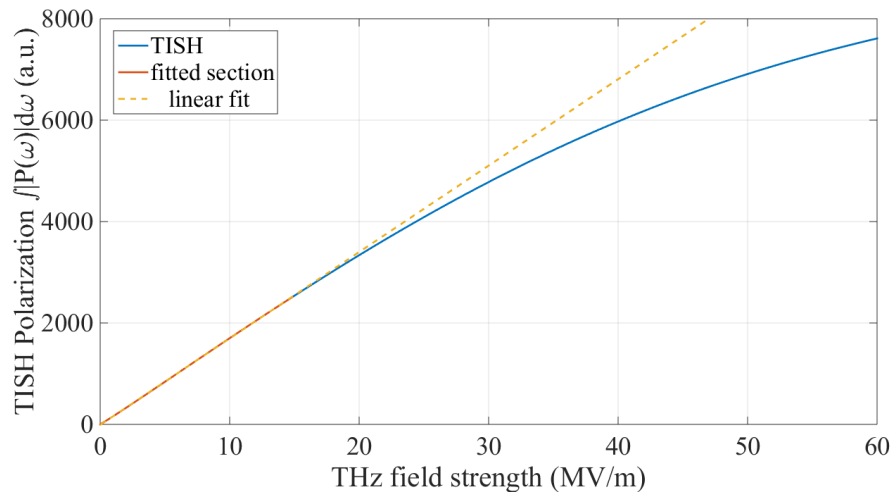


Figure 3.25 Spectrally integrated TISH polarization v.s. THz field strength.

To summarize, we have demonstrated a novel coherent THz detection technique (OBCD), and the observed TISH spectrum shift is explained by phase matching of tightly focused Gaussian beams. Coherent control in OBCD is demonstrated and modeled with a spectrally shifted TISH. For future work, the optical bias can be generated from a split probe arm, then recombined with the probe fundamental. The amount of optical bias is then independent of probe intensity, and can be optimized for signal-to-noise ratio. Finally, if TISH saturation can be experimentally observed at high THz field strength, it can serve as additional evidence for the plasma current model.

Chapter 4. Broadband Terahertz Detection II

4.1. THz induced electroabsorption in Semiconductors

Electric field induced absorption change in semiconductor (electroabsorption, EA) can be caused by different physical phenomena including the Franz-Keldysh Effect (FKE) [100] [101], the Quantum Confined Stark Effect (QCSE) [102], and the AC Stark effect [103]. Excitonic electroabsorption has a response time as fast as 50 fs [104], which is a major advantage for applications in high speed communication. For this reason, EA has been subject of studies in opto-electronics, e.g. electroabsorption modulators (EAM). The necessary electric fields are typically applied with a bias voltage across metallic contacts, and a 50 GHz bandwidth has been demonstrated with a multiple quantum well (MQW) EAM [105]. Electronically controlled switching bias, however, cannot reach speeds approaching 1 THz. The recent availability of strong THz field (>1 MV), most notably through air breakdown plasma with femtosecond lasers, opened up the possibility of THz-induced electroabsorption. EA in quantum dots [106] and carbon nano tubes (CNT) [107], for example, have been demonstrated with sub-picosecond response time.

In this chapter, broadband THz detection using THz induced electroabsorption in semiconductors is demonstrated. The detection bandwidth can be greatly enhanced when the material thickness is small compared to the THz wavelength (in our case $\approx 1\mu\text{m}$). The common problem of high dispersion around the Restrahlen absorption band in solid-state detectors is negligible. We have observed modulation of the transmission spectra up to $\approx 40\%$ $\Delta T/T_0$ and a detection bandwidth exceeding 7 THz (Figure 4.1). In this particular set of data, obtained by averaging ~ 50 spectra from an USB spectrometer, shows signal-to-noise ratio ≈ 80 . The corresponding minimum detectable peak THz field strength is 8.8 kV/cm. Higher sensitivity can be obtained by more spectra averaging, or by taking the time trace with the combination of PMT and monochromator (Section 4.2). Detailed analysis of the experimental data is presented in this chapter. The large depth of

modulation makes THz imaging with electroabsorption a possibility, a subject that will be discussed in Chapter 5.

This work is motivated by earlier reports of excitonic electroabsorption in multiple quantum wells with DC bias [80], electroabsorption in asymmetric multiple double quantum wells (ADQW) using QCSE with DC bias [81], and THz transient induced EA in GaAs/AlGaAs QWs [108]. To demonstrate THz coherent detection using QCSE, a complicated beam geometry is necessary because of the high refractive index of semiconductors. We however observed large amount of electroabsorption when THz polarization is perpendicular to the growth direction of the asymmetric/ symmetric double quantum wells (ADQW/ SDQW). This is unexpected because the QCSE should only occur when the electric field is polarized parallel to the direction of the quantum confinement. To isolate the responsible mechanism, we have investigated a bulk Al_{0.11}Ga_{0.89}As sample, and found the time-dependent differential spectra are explained by the combination of Franz-Keldysh and Fabry-Perot effects.

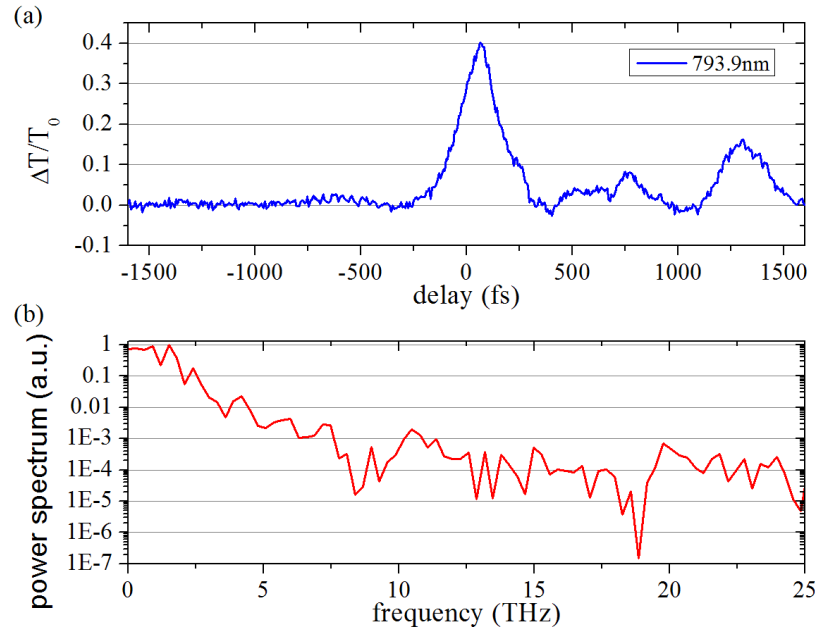


Figure 4.1 Single-cycle THz induced electroabsorption in AlGaAs at 793.9 nm. (a) EA v.s. THz-NIR probe delay with $\Delta T/T_0 \approx 40 \%$, and (b) corresponding power spectrum showing bandwidth exceeding 7 THz.

4.2. THz-EA Experimental Setup

The setup is similar to the pump-probe experiment described in Section 3.4. The THz-EA experiment consists of a generation arm as previously detailed in Section 3.4, and a detection arm with either unfocused or focused probe. The probe intensity is attenuated below 1.6 μJ with refractive metallic neutral density filters (Thorlabs) to avoid free carrier effects, and to prevent damages when focused probe is used. In the case of an unfocused probe, a metallic pinhole of 150 μm mounted in X-Y translation is placed behind the sample to sample the localized electroabsorption response. This is better than getting an average response when the THz profile is known to be non-uniform. A 50 cm calcium fluoride lens (Thorlabs LA5464) is used in the focused probe geometry; the focused spot is smaller than 50 μm . Figure 4.2 shows the schematic of the experiment using a focused pulse.

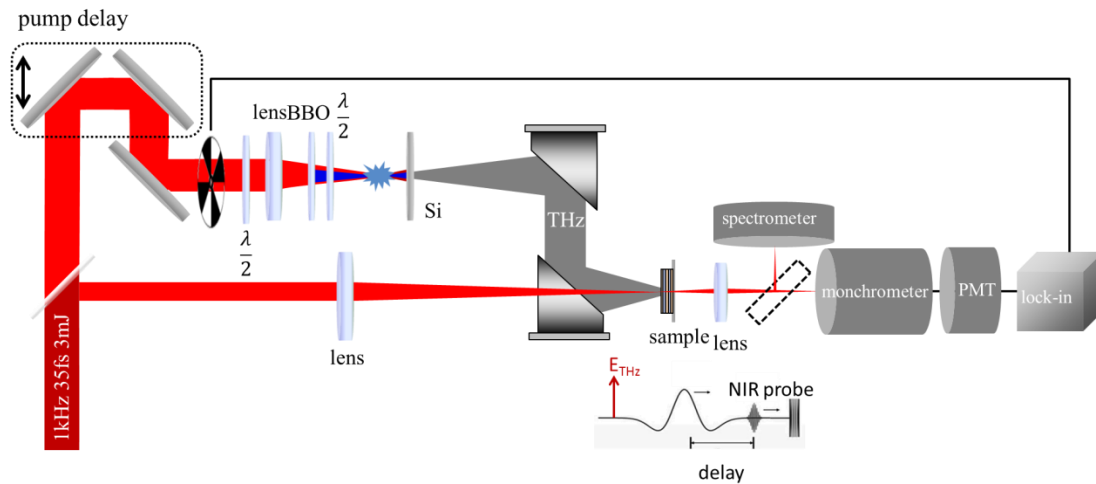


Figure 4.2 Schematic of THz-EA experimental setup.

Supercontinuum generated by a sapphire crystal can also be used as an octave-spanning probe that can be spectrally filtered by equilateral prism pairs and a knife edge. A supercontinuum probe avoids large free-carrier absorption when ADQW/ SDQW is interrogated at room temperature, and provides the extended spectral range for probing bulk GaAs at room temperature.

A schematic of the supercontinuum generation and its spectral modulation is shown in Figure 4.3 (a). Supercontinuum is generated and collimated by a pair of lenses (L1 and L2). The end mirror after prism pairs (M1) tilt the beam slightly vertical, allowing the return beam to be picked up and sent to the experiment by a second mirror (M2).

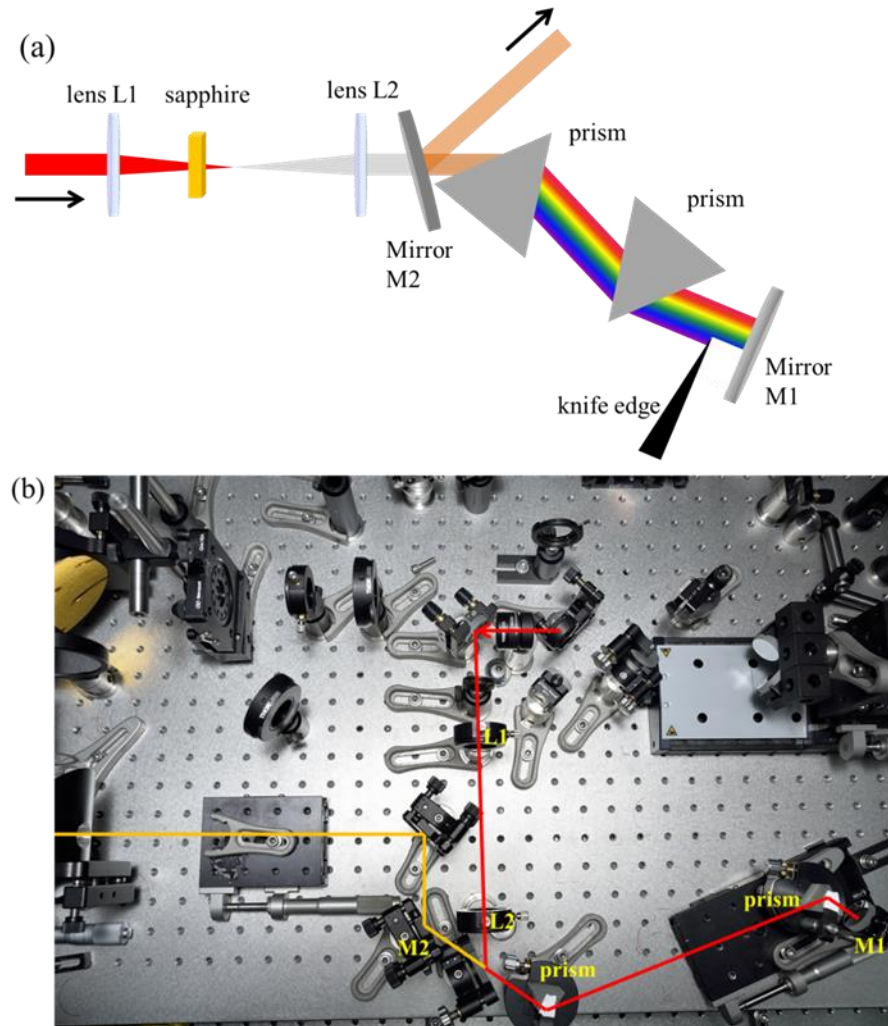


Figure 4.3 (a) Supercontinuum generation and spectral modulation. (b) Photo of the setup without sapphire crystal and knife edge.

The alternative to the use of a filtered supercontinuum probe is to cryogenically cool the samples. A liquid nitrogen cryostat (Janis) is deployed for this purpose. To allow transmission of the far-IR, a special cryostat window is used. It is a 17mm-diameter,

250 μm -thick piece of CVD diamond mounted in custom holder. A spectrometer shows the window has $\approx 60\%$ power transmission across relevant THz spectrum. The temperature of the sample is varied by a Lakeshore 331 PID controller.

By varying the delay τ between THz pump and weak NIR probe, temporal electroabsorption response $\Delta T_\lambda(\tau)$ can be measured at selected wavelength using a monochromator with a photo-multiplier tube (PMT) detector. The complete spectral-temporal response $T(\lambda, \tau)$ can be measured, by recording the time-dependent transmission spectra with Ocean Optics HR-4000 USB spectrometer. The THz is chopped at 1 Hz with Thorlabs MC2000 optical chopper between the off-axis mirror pair.

The normalized transmission change is $\frac{\Delta T(\lambda, \tau)}{T_0(\lambda)}$, where $T_0(\lambda)$ is the sample transmission spectra in the absence of THz light. Chopping the THz beam allows the acquisition of $T_0(\lambda, \tau)$ instead of just a reference spectrum $T_0(\lambda)$, and the laser power fluctuations are thereby removed. An average of 100 spectra per delay step was made to increase the signal-to-noise ratio.

The ADQW structure we investigated was first proposed by Aguilar et al. [81]. Our samples were grown by Dr. Jeffery Cederberg with MOCVD process at Sandia National Laboratory. The ADQW contains 90 pairs of 5 nm and 6 nm double quantum wells, separated by 2 nm of Al_{0.3}Ga_{0.7}As. A SDQW sample was grown on GaAs (100) substrate as a comparison with the same structure except for an equal quantum well thickness of 5 nm (Figure 4.4(a)). Photoluminescence spectra of ADQW/ SDQW are shown in Figure 4.4 (b). The variation of the peak wavelengths is due to sample inhomogeneity across the wafer. GaAs heterostructure (750 nm InGaP/ 750 nm GaAs/ 750 nm InGaP) and Al_{0.11}Ga_{0.89}As bulk thickness of 1017 nm were also investigated. As the experiment is setup in transmission geometry, all samples are epitaxially lifted off from the substrate and then bonded to BK7 glass slides. Our group member Zhou Yang processed the samples using techniques that make bonding large-area samples possible [109] [110] (Figure 4.5).

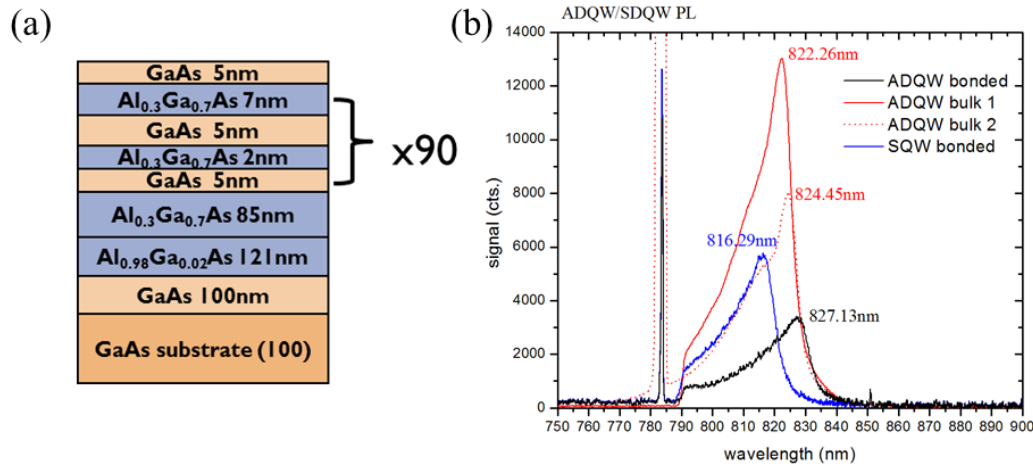


Figure 4.4 (a) Structure of SDQW, and (b) photoluminescence (PL) spectra of ADQW and SDQW.

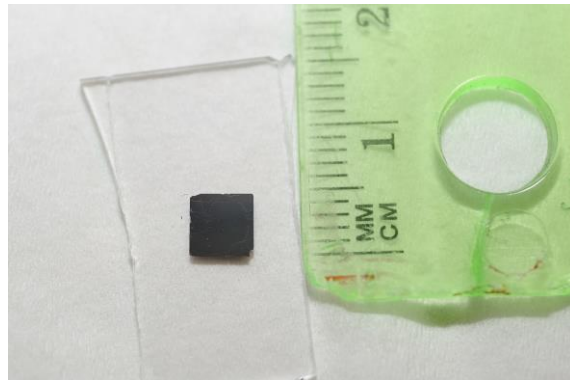


Figure 4.5 Photo of large area Al_{0.11}Ga_{0.89}As sample, bonded to a glass slide.

4.3. THz-EA results and discussion

By treating the THz transient as a quasi-DC field, the electroabsorption in bulk semiconductors we observed can be described by the Franz-Keldysh effect (FKE) [100] [101]. The Franz-Keldysh effect is named after Walter Franz and Leonid Keldysh, and was first observed by Böer et. al. [111]. In the absence of external electric field, the two

particle (electron-hole pair) Schrödinger equation and its discrete solution $\phi_n(\vec{r})$ without Coulomb potential is [112]:

$$-\frac{\hbar^2}{2m_r} \nabla^2 \phi(\vec{r}) = E\phi(\vec{r}), \quad \phi_n(\vec{r}) = \frac{e^{ik_x x + ik_y y + ik_z z}}{\sqrt{V}}. \quad (4.3.1)$$

Where $\phi(\vec{r})$ is the wave function, E is the energy measured from bandgap energy E_g .

$m_r = (1/m_e^* + 1/m_h^*)^{-1}$ is the reduced effective mass, where m_e^* and m_h^* are the effective electron and hole mass, respectively. The quantum number $n \equiv (n_x, n_y, n_z)$. The wave vector $k_{x,y,z} = 2\pi n_{x,y,z} / L$, where L is the unit cell length. V is the unit cell volume.

In comparison, under the influence of uniform electric field, the Schrödinger equation becomes [112]:

$$(-\frac{\hbar^2}{2m_r} \nabla^2 + e\vec{F} \cdot \vec{r})\phi(\vec{r}) = E\phi(\vec{r}). \quad (4.3.2)$$

Assuming the applied field \vec{F} is along z axis ($\vec{F} = F\hat{z}$), the solution is [112]:

$$\phi(\vec{r}) = \frac{e^{ik_x x + ik_y y}}{\sqrt{A}} \phi(z), \text{ where } \frac{d^2\phi(Z)}{dZ^2} - Z\phi(Z) = 0. \quad (4.3.3)$$

A is the area of the unit cell and $Z = (\frac{2m_r e F}{\hbar^2})^{1/3} (z - \frac{E_z}{eF})$, where E_z is the eigenenergy of the z dependent wave function. The solution for the Z dependent part of the wave function has the form of Airy function. The forbidden optical transitions below the bandgap then become possible due to tunneling. When a time varying electric field is applied, the electroabsorption is referred as dynamic Franz-Keldysh effect [113] [114]. Since the slowly varying THz transient can be consider as a quasi-DC field, we found it sufficient to model the experimental data with classical FKE.

The modified absorption coefficient due to FKE, which can be derived from the transition rate given by the Fermi's golden rule and the wave function solution of Eq. (4.3.3), is [112]:

$$\alpha(\omega) = \frac{e^2 E_p}{12c\epsilon_0 m_r n_r \omega} \left(\frac{2m_r}{\hbar^2} \right)^{3/2} \sqrt{\hbar\theta_F} \left[-\eta A_i^2(\eta) + A_i'^2(\eta) \right], \quad (4.3.4)$$

where m_0 , E_p , ϵ_0 , n_r are the electron mass, Keldysh energy parameter, vacuum dielectric constant, refractive index (assumed constant), respectively. A_i is the Airy function. $\hbar\theta_F = \left(\frac{\hbar^2 e^2 F^2}{2m_r} \right)^{1/3}$ and $\eta = \frac{E_g - \hbar\omega}{\hbar\theta_F}$. In the limit of $F \rightarrow 0$ it can be shown that the FKE modified $\alpha(\omega)$ approaches the free carrier absorption value $\alpha_0(\omega)$ [112]:

$$\begin{aligned} \alpha_0(\omega) &= \frac{e^2 E_p}{12c\epsilon_0 m_r n_r \omega} \left(\frac{2m_r}{\hbar^2} \right)^{3/2} \frac{\sqrt{\hbar\omega - E_g}}{\pi} && (\hbar\omega \geq E_g) \\ \alpha_0(\omega) &= 0 && (\hbar\omega < E_g). \end{aligned} \quad (4.3.5)$$

An example calculation of the FKE oscillation is plotted in Figure 4.6. Notable characteristics of FKE are the increase of absorption below the gap, and an oscillatory behavior of the absorption coefficient above the gap. The spectral oscillatory frequency in the above-gap region decreases with the increase of electric field strength.

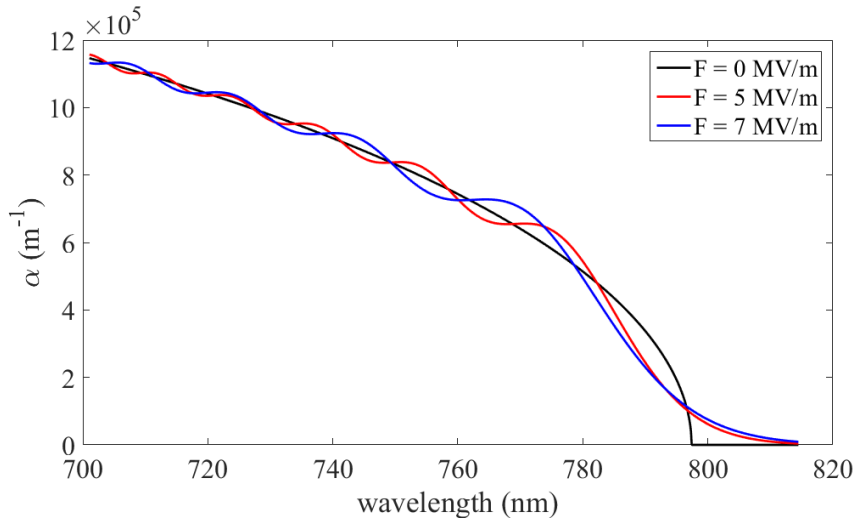


Figure 4.6 Calculated Franz-Keldysh oscillation (red and blue lines, $F>0$), compared to free carrier absorption (blue line, $F=0$).

The normalized electroabsorption response $\frac{\Delta T(\lambda, \tau)}{T_0(\lambda)}$ of the $\text{Al}_{0.11}\text{Ga}_{0.89}\text{As}$ bulk

sample at room temperature subjected to the time dependent THz bias field is shown in Figure 4.7 (a). The calculated FKE response using THz waveform measured by OBCD (Figure 3.18 (a)) is shown in Figure 4.7 (b). The above gap behavior is well described by the FKE. The below-gap spectral oscillations in the experimental data, however, are not predicted by Franz-Keldysh effect. A plausible explanation is given by the Fabry-Perot transmission interference arising from the air-semiconductor and the semiconductor-glass interfaces.

We now derive the Fabry-Perot transmission of the NIR probe corresponding to our experiment conditions. We assume the multiple reflections occur between the air-semiconductor and the semiconductor-glass interfaces. The reflections from the glass-air interface are not considered because the glass slide thickness is much greater than the coherence length. Each medium has different index of refraction. The semiconductor layer in addition has index of refraction that changes when the THz modulates the absorption. The absorption of the NIR probe pulse in the semiconductor layer is accounted for, and this absorption is also modified by the THz pump.

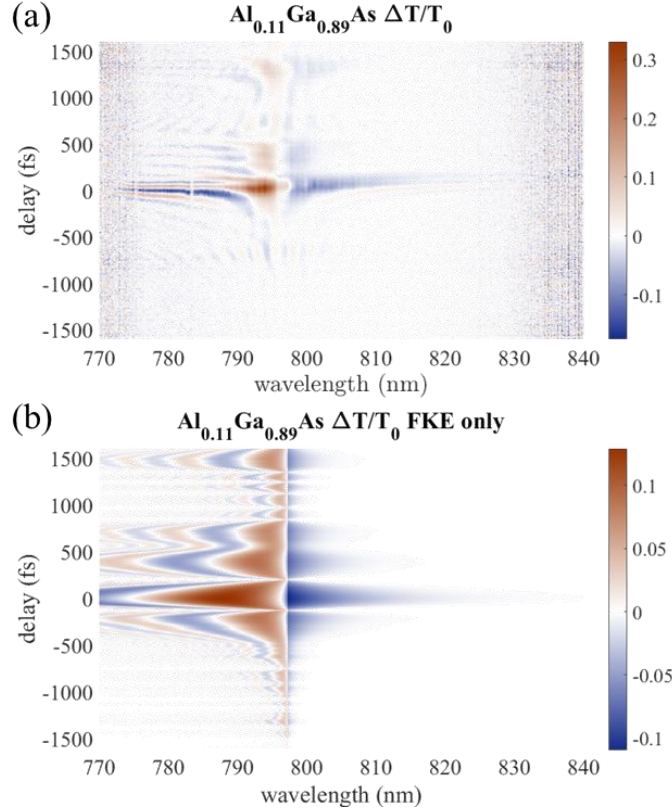


Figure 4.7 (a) Measured normalized EA response $\Delta T(\lambda, \tau)/T_0(\lambda)$ of the Al_{0.11}Ga_{0.89}As bulk sample, and (b) $\Delta T(\lambda, \tau)/T_0(\lambda)$ modeled using FKE.

A schematic illustrating multiple reflections within the bonded sample is shown in Figure 4.8. n_0 , n_1 , and n_2 are the refractive indices of air, semiconductor, and glass, respectively. Following the usual formalism for the Fabry-Perot transmission and adding the media absorption, the total complex electric field transmission coefficient is:

$$t = \sum_{m=0}^{\infty} t_m = e^{-\frac{\alpha L}{2\cos\theta_1}} t_{01} t_{12} \sum_{m=0}^{\infty} (r_{10} r_{12} e^{-\frac{\alpha L}{\cos\theta_1}} e^{i\delta})^m = \frac{t_{01} t_{12} e^{-\frac{\alpha L}{2\cos\theta_1}}}{1 - r_{10} r_{12} e^{-\frac{\alpha L}{\cos\theta_1}} e^{i\delta}}. \quad (4.3.6)$$

t_m is the m -th transmitted field, L is the thickness of the sample, θ_1 is the probe refractive angle in the semiconductor as given by Snell's Law: $\theta_1 = \arcsin(n_0 \sin \theta_0 / n_1)$, where θ_0 is the probe incident angle. t_{01} and t_{12} are the field transmission coefficients of the air-

semiconductor interface and the semiconductor-glass interface. r_{10} and r_{12} are the field reflection coefficients of the semiconductor-air interface and the semiconductor-glass interface. Because the reflections at both interfaces are internal, r_{10} and r_{12} are real quantities. δ is the phase difference that is added to each successive reflection due to the path length difference:

$$\delta(n_1, \lambda) = 2k_1 L / \cos \theta_1 - k_2 L_2 = \frac{4\pi n_1}{\lambda} L \cos \theta_1, \quad (4.3.7)$$

where k_1 and k_2 are the probe wave-vectors in semiconductor and glass, respectively. The path length difference between t_m and t_{m-1} in glass is $L_2 = 2L \tan \theta_1 \sin \theta_2$, where θ_2 is the refraction angle in glass: $\theta_2 = \arcsin(n_1 \sin \theta_1 / n_2)$.

The transmitted intensity is:

$$T(\theta_1(n_1), \lambda, \alpha) = tt^* = \frac{|t_{01}|^2 |t_{12}|^2 e^{\frac{-\alpha L}{\cos \theta_1}}}{1 + |r_{10}|^2 |r_{12}|^2 e^{\frac{-2\alpha L}{\cos \theta_1}} - 2|r_{10}||r_{12}|e^{\frac{-\alpha L}{\cos \theta_1}} \cos(\frac{4\pi n_1 L \cos \theta_1}{\lambda})}. \quad (4.3.8)$$

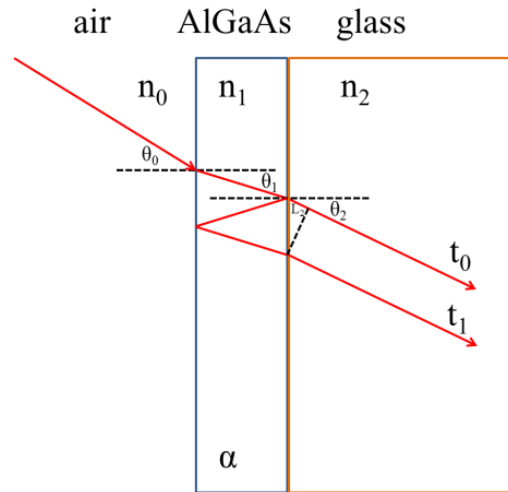


Figure 4.8 Multiple reflections in bonded EA samples.

The transmitted intensity is time-dependent because it depends on time-dependent n_1 and α . More explicitly, the time-dependent n_1 modifies the refractive angles (θ_1 and θ_2) and the Fresnel reflection/ transmission coefficients (r_{01} , r_{10} , t_{01} , and t_{12}). The change of refractive index Δn_1 due to the change of the absorption $\Delta\alpha$ can be calculated using Kramers-Kronig relationship:

$$\Delta n_1(\omega) = \frac{c}{\pi} \int_0^\infty \frac{\Delta\alpha(\omega')}{\omega'^2 - \omega^2} d\omega' . \quad (4.3.9)$$

With the above modification, the normalized differential transmission $\Delta T(\lambda, \tau)/T_0(\lambda)$ is calculated in Figure 4.9 (a). All the essential features of the experimental data are well reproduced. The blue line in Figure 4.9 (b) shows $\Delta T(\lambda, \tau)/T_0(\lambda)$ fitted at single time delay, and the red line shows the data fitted exclusively with FKE with the same parameters. The main takeaway for Figure 4.9 (b) is that a more accurate model accounting for both FKE and Fabry-Perot interference describes increased transmission below the gap, while a model that ignores interference cannot.

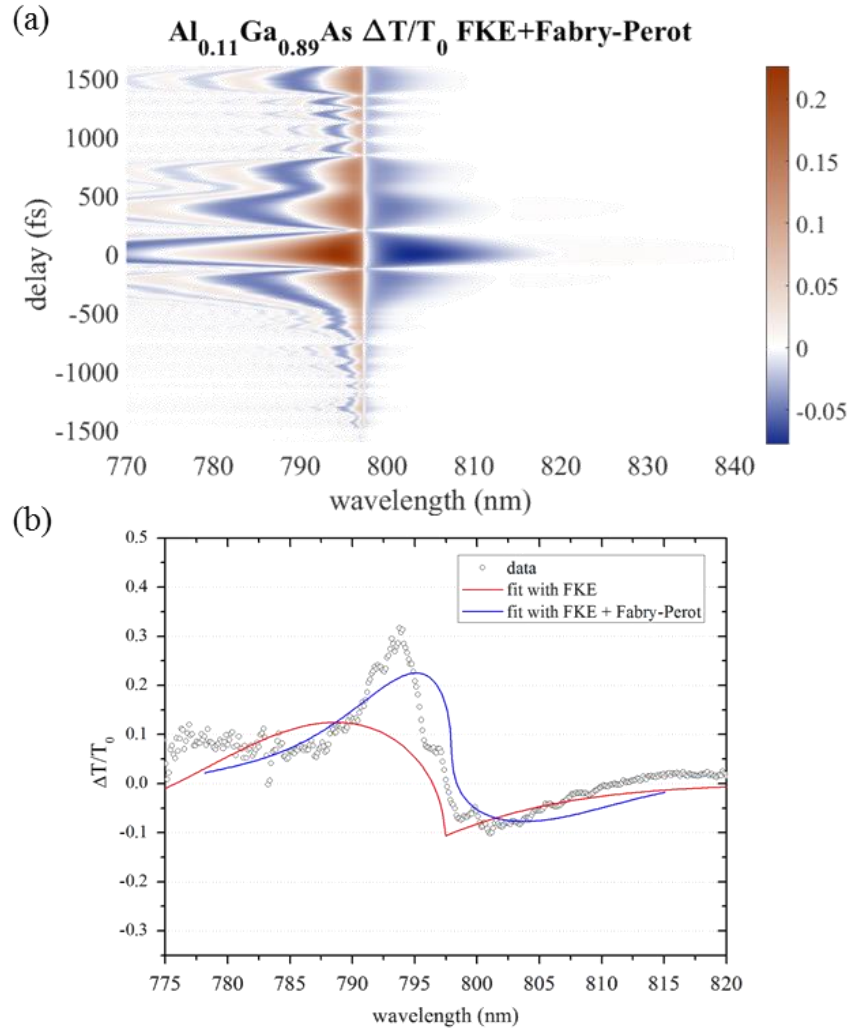


Figure 4.9 (a) Calculated EA response $\Delta T(\lambda, \tau)/T_0(\lambda)$ by combined effect of the FKE and Fabry-Perot. (b) $\Delta T(\lambda, \tau)/T_0(\lambda)$ data at single delay (circle dots), fitted with the FKE and Fabry-Perot Effect (red line), and same fit with the Fabry-Perot effect turned off (blue line).

The experimentally measured data can also be used to retrieve the THz waveform. By least square fitting of field strength at each delay, while keeping the other parameters fixed, the THz waveform amplitude can be extracted (Figure 4.10).

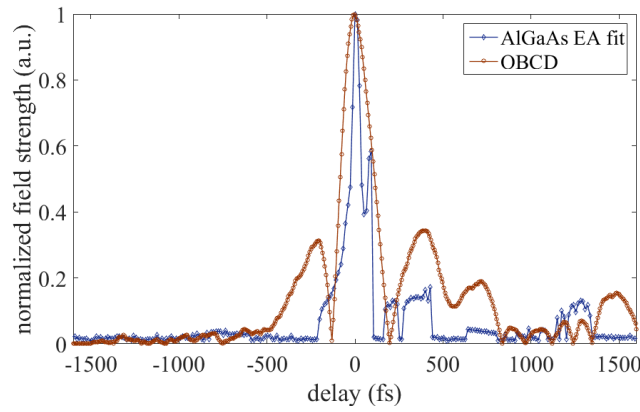


Figure 4.10 OBCD measured THz waveform (blue line), and THz waveform extracted form $\Delta T(\lambda, \tau) / T_0(\lambda)$ (red line).

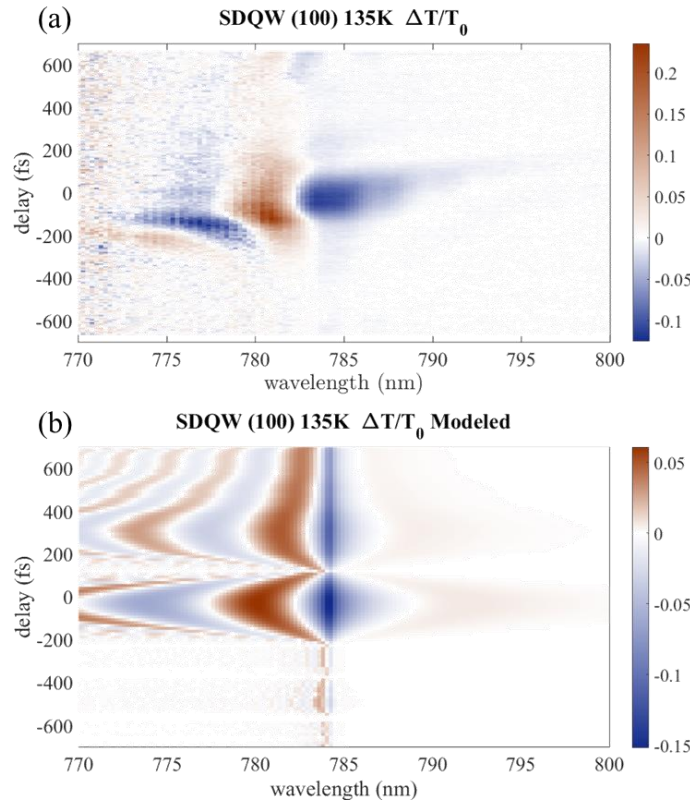


Figure 4.11 (a) Measured and (b) modeled $\Delta T(\lambda, \tau) / T_0(\lambda)$ for SDQW structure at 135K.

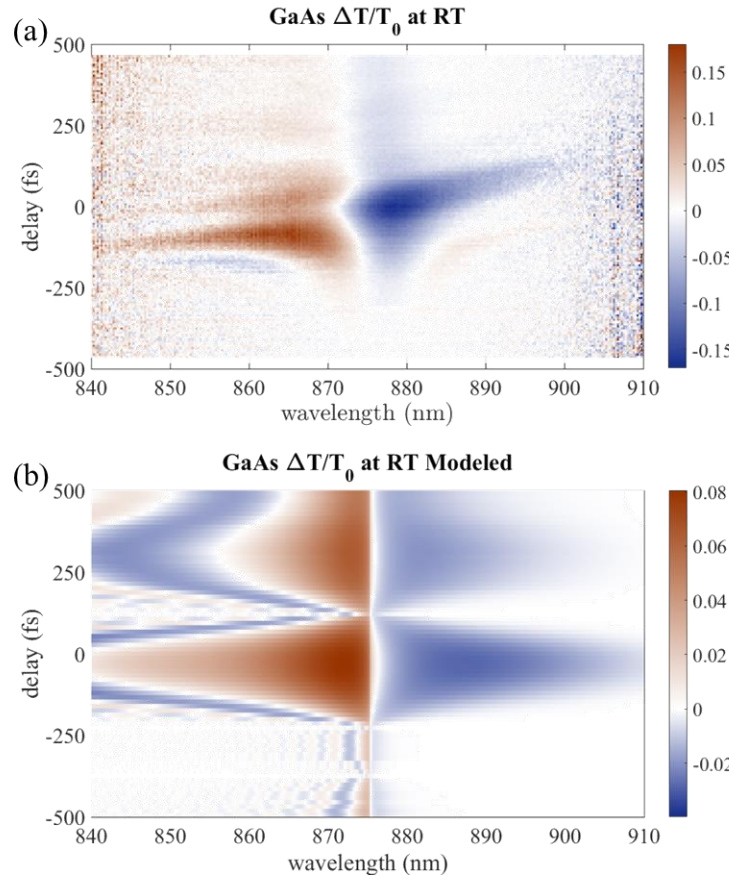


Figure 4.12 Measured and modeled $\Delta T(\lambda, \tau)/T_0(\lambda)$ for GaAs structure at room temperature with spectrally filtered supercontinuum probe.

In this chapter we have shown large electroabsorption induced by single cycle THz pulse. The electroabsorption response $\Delta T(\lambda, \tau)/T_0(\lambda)$ can be modeled with the combination of the Franz-Keldysh and the Fabry-Perot effect. For future studies, one could demonstrate coherent THz detection with quantum confined stark effect in an ADQW structure. The THz electric field, however, must be polarized along the quantum confinement direction. This requires complicated experimental setup, as one must be able to isolate the contribution of QCSE induced EA (coherent) from the FKE induced EA (incoherent).

Chapter 5. THz Electroabsorption Imaging

5.1. Introduction

The importance of THz imaging has been briefly summarized in Chapter 1. Similar to the THz detection, THz imaging techniques can be catalogued as incoherent or coherent techniques, and continuous-wave (narrow-band) or pulsed (broadband) techniques. Incoherent THz real-time imaging can be performed with a pyroelectric camera [115] or a microbolometer array [116]. An example of a commercialized microbolometer cameras is the NEC unclooled THz imager. There are also commercially available CW THz sources derived from photomixing in a PCA or the QCL. The combination of such sources and detectors yields a tunable narrow-band real-time THz imaging system achieved with relatively low cost and complexity.

Coherent THz imaging is typically uses raster scanning with EOS or photoconductive antenna [3]. The main drawback of raster scan is the relatively slow image acquisition speed. Use of an arrayed photoconductive antenna [117], for example, can increase data collection rate. Alternatively, Zhang et al. have demonstrated THz imaging using the EOS of the entire THz beam [118] [119] [120] [121]. More sophisticated techniques include compressed sensing [122] [123], interferometric array [124], and linearly chirped probe [125] that improve the speed of image acquisition.

The large electroabsorption via FKE demonstrated in Chapter 4 is a promising approach for incoherent THz imaging. The formalism detailed in Section 4.3 is used to calculate FKE EA response of a semiconductor (band edge at 797nm), shown in Figure 5.1. The large modulation above the gap does not scale monotonously with field strength due to the Franz-Keldysh oscillation (Figure 5.1 (b)), so it is important to select the probe wavelength to be below the gap for imaging purposes.

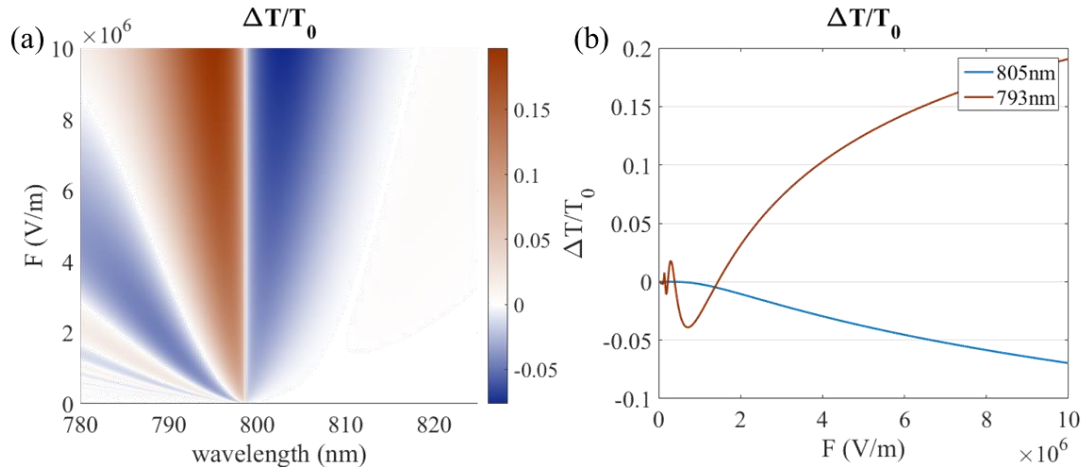


Figure 5.1 Calculated $\Delta T/T_0$ versus field strength F , including Franz-Keldysh and Fabry-Perot effect. Band edge wavelength used is 797 nm. (a) $\Delta T/T_0$ across all wavelengths, and (b) $\Delta T/T_0$ at 793 nm and 805 nm.

In this chapter, two schemes for the THz EA imaging are proposed. In the first scheme, EA response of the semiconductor images a focused THz beam. This is potentially a fast and inexpensive THz imaging technique, which requires only a CCD camera responsive to the probe wavelength (800nm in our experiment).

As discussed in Chapter 2, the spatial profile of a THz pulse generated from air-breakdown plasma is not uniform, which makes it a poor choice as an imaging source. The object size for this large-area THz-EA imaging technique is also limited by the spot size of the focused THz beam ($\approx 375 \mu\text{m}$ in our setup). The object features that can be resolved must be larger than THz wavelength (30 μm - 300 μm) to avoid diffraction. Higher power and uniform THz sources, such as optical rectification with LiNbO₃, DSTMS, and OH1 [37], are better suited for this application because looser focusing can be used.

The second imaging scheme is to use the semiconductor structure as a single-pixel detector. The THz images are obtained with a raster scan, which relaxes the limitation on the object size. A PMT is used in our experiment to obtain high dynamic range. The image acquisition time can be reduced with a 2-axis motorized translation stage.

5.2. THz-EA imaging Experimental Setup

There are two types of imaging experiments described in this section. The first utilizes the entire focused THz beam for the large-area THz-EA imaging, and the second uses raster scan imaging.

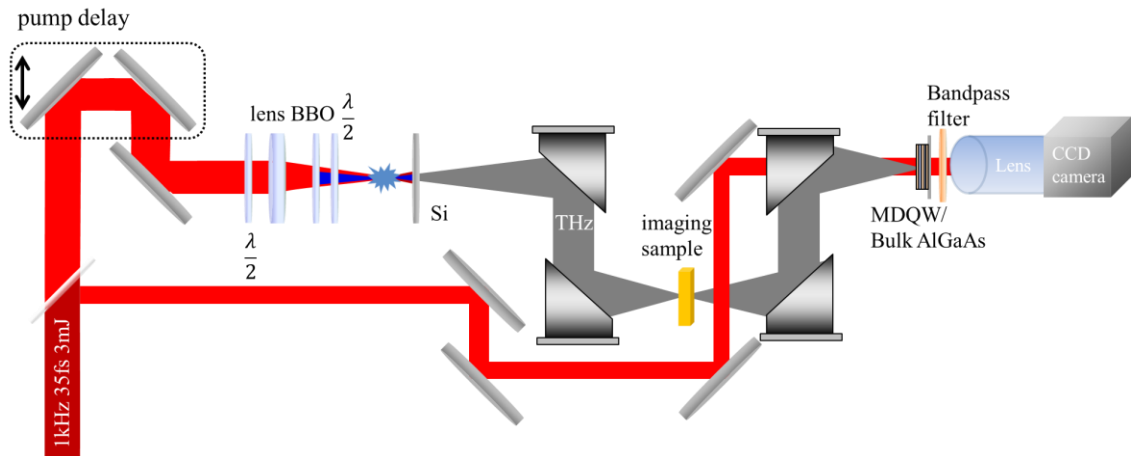


Figure 5.2 Schematic for direct THz-EA imaging setup.

The experimental setup for large-area THz EA imaging is shown in Figure 5.2, the THz generation arm is described in Section 3.4. The object to be imaged is located where the THz beam is focused. The THz beam transmitted through the object is collimated and focused onto the semiconductor detector, which is a MDQW or bulk semiconductor. The imaging magnification is determined by the off-axis parabolic telescope. There are four off-axis parabolic mirrors with focal lengths (in sequence) of 7.62 cm, 5.08 cm, 7.62 cm, and 5.08 cm (Edmunds Optics NT63-200, NT63-199, NT63-188, and NT63-199 with a hole drilled in the center). Magnification at the detector is unity. The unfocused near-IR probe beam passes through the hole in the final OAPM, and is incident onto the detector collinearly with the THz beam. The probe pulse is brought into temporal overlap with the THz pulse with a motorized stage delay. The transmitted probe beam is filtered by a bandpass filter that selects the probe spectral range. A bandpass filter of 810 ± 10 nm (Thorlabs FB810-10) is used for AlGaAs, and a $830\text{ nm}\pm10$ nm bandpass filter is used for SDQW (Thorlabs FB830-10). A zoom lens of variable magnification from 0.7 to 4.5

(Edmund Optics NT83-892) is mounted on the CCD camera (Mightex BTE-B050-U) to increase resolution. By capturing the images with and without the object, and a background image of the probe itself, THz imaging of the object can be obtained by:

$$\frac{image_{off} - image_{on}}{image_{off} - image_{BG}}, \quad (5.2.1)$$

where $image_{off}$ and $image_{on}$ are the images captured without and with the object, respectively. $image_{BG}$ is the background image captured without the THz pulse and the object present. The final image is normalized to the signal in the area where THz beam is completely blocked by the object. When simply imaging the THz profile at generation point, i.e. without an object, a background subtraction suffices. The CCD camera manufacturer supplied a Microsoft C# image capture sample software, it is modified to view images with background subtraction in real-time, enable convenient alignment and optimization.

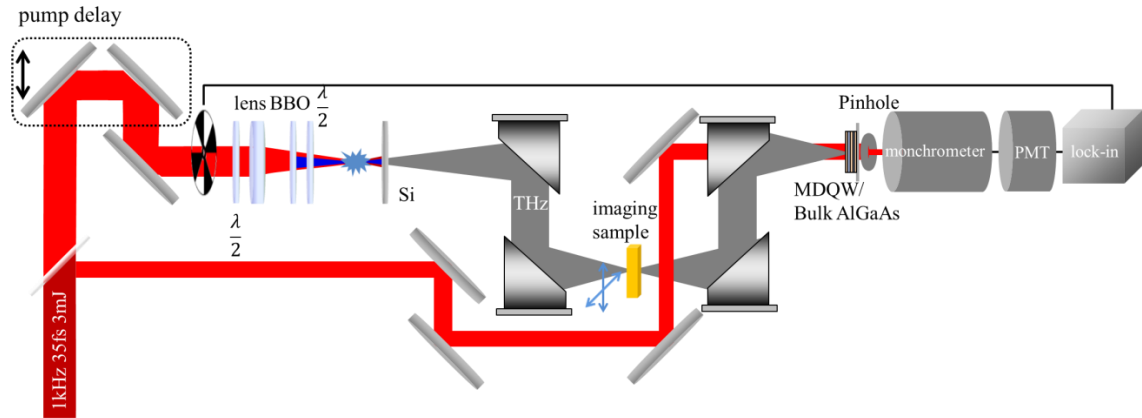


Figure 5.3 Schematic for THz-EA raster scan imaging setup.

The second method treats the semiconductor EA device as a single-pixel detector. The OAPM telescope in this configuration has less magnification, but it's irrelevant to single-pixel detection. The object is translated across two dimensions orthogonal to the beam path allowing the EA response to map out the THz transmission. The maximum object size is only limited by the range of the translation. A photo of the setup is shown in

Figure 5.3. A metallic pinhole of $150\mu\text{m}$ is placed behind the detector to define the size of the single-pixel. The transmitted probe passes through a monochromator impinging on a PMT. Lock-in detection is used.

The imaging targets for large area imaging includes cross slits of 50, 100, 200, and $300\mu\text{m}$. The raster scan images a plastic sheet with lettering ‘THZ’ cut out. All targets were commercially 3-D printed. Photos of targets are shown with the imaging results in Section 5.3.

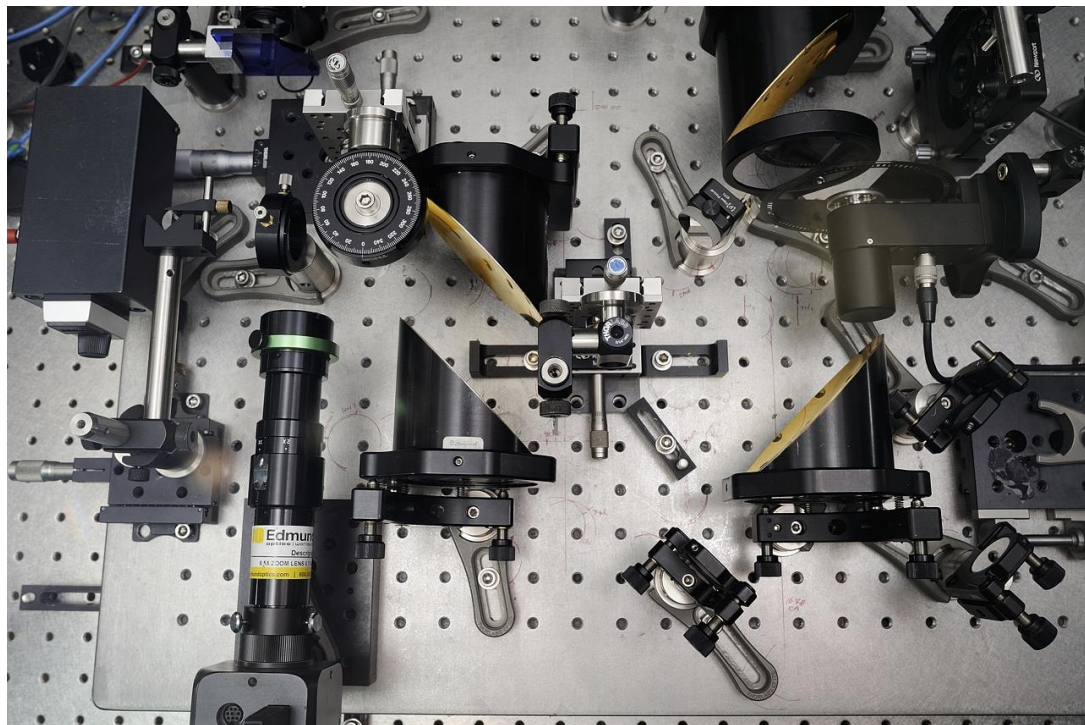


Figure 5.4 Photo of the detection section of THz EA imaging setup.

5.3. THz-EA imaging results and discussion

We first show the THz beam profile at the generation point, i.e. without an object, imaged at the focus of the last OAPM (Figure 5.5). A SDQW is used here due to the large

electroabsorption modulation below the gap it exhibits. The fringes and dots in the processed images are the unfocused probe diffraction pattern by the hole in the last OAPM and the defects on the sample. Differential imaging should remove these from the background, but the residual signals remain due to both power and spatial fluctuations of the amplified laser beam.

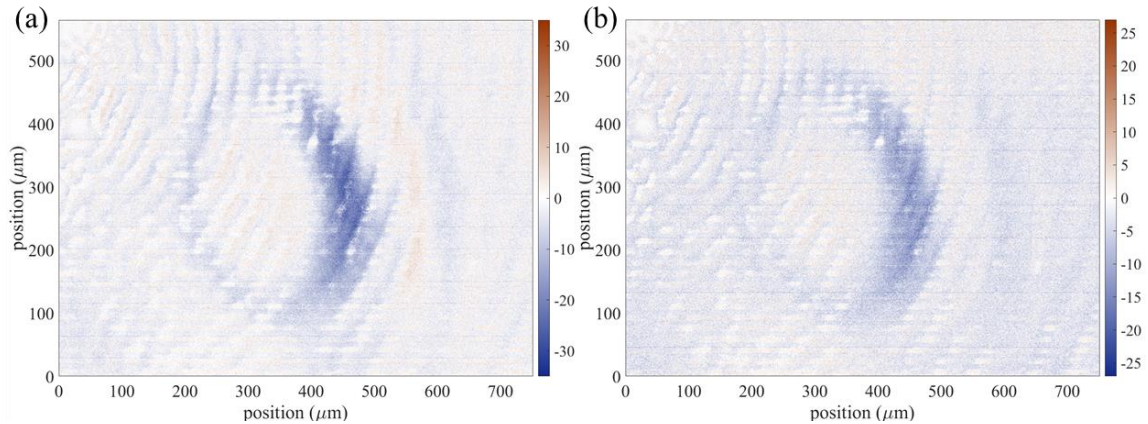


Figure 5.5 THz profiles at the generation point. (a) pump power of 1.1W, and (b) 0.9W.

The ring structure of the THz profile is consistent with the discussion and modeling in Chapter 2 without a limiting aperture. It arises from the opacity at the center of the high density air-breakdown plasma. The measured THz beam size between first and second OAPMs is about 2.5 cm diameter, which is much smaller than the 7.5 cm collection area of the OAPM. No aperture effect is expected or observed. The dimensions in Figure 5.5 are deduced from pixel size of the CCD camera and the 3X magnification of the lens. The spot size is also consistent with the knife edge experiments (Section 3.4). The two profiles at different pump powers are shown, with the lower-power one displaying a marginally smaller hole in the center, consistent with the model.

Next we quickly demonstrate the effect of a metallic waveguide in THz generation. A gold waveguide of inner diameter around $500\mu\text{m}$ is placed at the focus of the pump, the corresponding THz profile is shown in Figure 5.6. Compared to the profile without waveguide, the spot size is larger, and its energy distribution is more localized. The THz

power is 72 % of the value measured by a pyroelectric detector without the waveguide. The modulation is larger, and could be contributed to change in THz frequency spectrum due to frequency-dependent waveguide loss, and the frequency-dependent EA response. The larger center hole is also expected due to higher plasma density at the center. The effect of a waveguide is, however, a complicated subject. Multiple parameters such as the material, dimension, placement of the waveguide, and the focusing geometry of the pump beam, affect the generated THz profile. As discussed previously in Section 3.4, a systematic study in the future is required to draw conclusions.

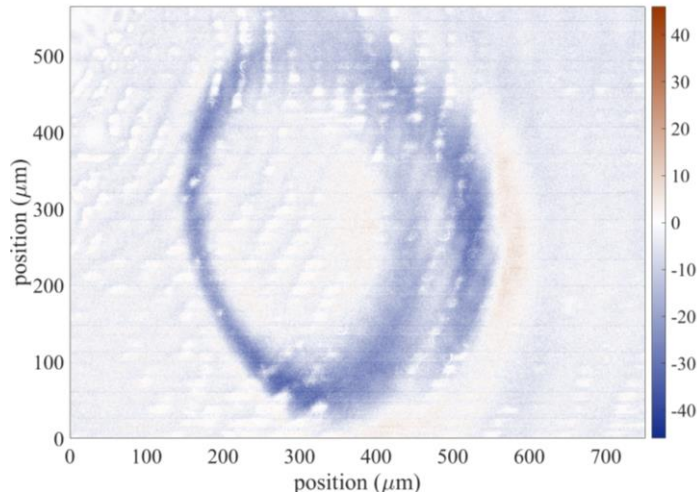


Figure 5.6 THz profile at the generation point with gold waveguide.

The commercially 3D printed plastic objects (Shapeways) for the large-area imaging experiment are shown in Figure 5.7. Because of the highly non-uniform THz profile from air-breakdown plasma and the tight focusing, it unsurprisingly we have yet to demonstrate imaging with these cross slits. The difficulty in imaging small features is consistent with the THz imaging resolutions previously reported (200 μm to 1 mm) [3] [116] [122]. The primary complication preventing diffraction-limit resolution here is the lack of THz intensity at the center of the beam.

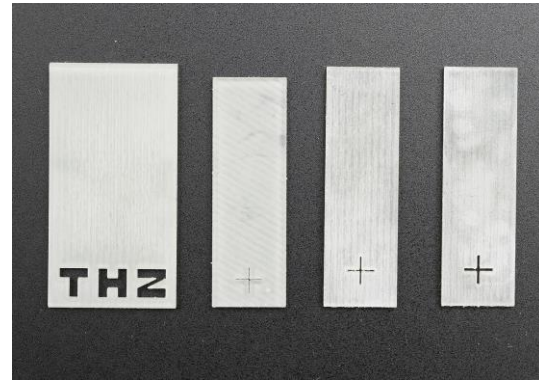


Figure 5.7 3D printed imaging objects. From left to right: the object for raster imaging, 100 μm cross slits, 200 μm cross slits, and 300 μm cross slits.

The raster method, in contrast, is not limited by THz beam size. THz raster imaging of the object, on the far left of Figure 5.7, is shown in Figure 5.8. The pixel size is 500 μm by 500 μm . The Bulk AlGaAs sample described in Section 4.2 was used as the detector in this experiment. Signal-to-noise ratio of about 67 was achieved with lock-in detection and a PMT. An automated data acquisition system would allow for rapid rendering of THz images.

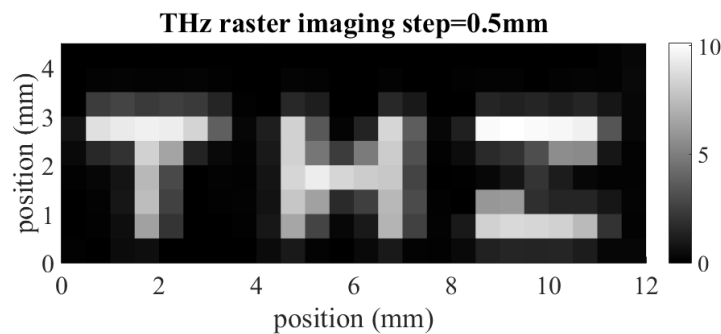


Figure 5.8 THz EA raster imaging.

To summarize, we have demonstrated THz imaging via electroabsorption with single-cycle THz pulse. The images of THz at the generation points exhibit features described by the model presented in Chapter 2. The effect of metallic waveguide on THz

generation was shown. The THz raster imaging with EA is demonstrated to be easy to implement.

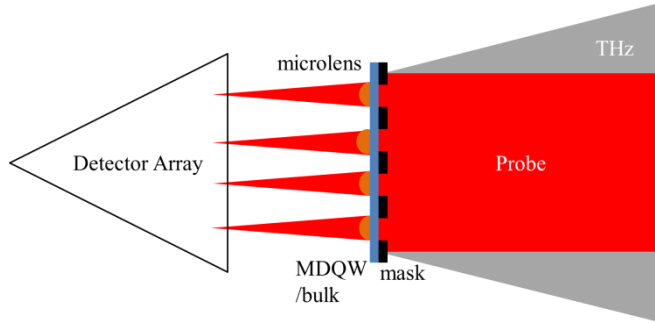


Figure 5.9 Schematic for arrayed THz-EA detection.

Future study can examine how various waveguide geometries affect THz generation in both temporal and spatial domain using OCD and THz EA imaging. For raster imaging, arrangements such as arrayed detection could be done to increase acquisition speed (Figure 5.9). As mentioned in Chapter 4, one could expect broadband coherent THz detection with a MDQW via QCSE, and with it, the hyperspectral imaging should be attainable.

Chapter 6. Conclusion and Research Outlook

In this dissertation we have modeled the terahertz profile generated by a two-color air plasma. For the generation part, the plasma current model is used. The propagated polarization is calculated from the solution of the wave equation, where the dispersion is included. The terahertz profile is shown to be ring-like due to the plasma screening, our approach to obtain THz profile is novel, although other published works have predicted the emission directionality as well. Without the propagation, the plasma current model also predicts that the optimal phase between the two-color fields should be around $\pi/2$. This is the major discrepancy between the plasma current model and the four-wave mixing picture; it should be subjected to future studies. This dissertation also includes, to our knowledge, the first theoretical prediction of pump power dependent optimal phase in two-color plasma THz generation

For the broadband terahertz detection, we have demonstrated the first an all-optical gas plasma detection technique based on ABCD. The controlled optical bias (second harmonic beam) is injected as the replacement of the high voltage bias in ABCD. The spectral shift of the TISH is uncovered and explained by phase matching condition while the coherence of the OBCD was studied. We have also modeled the detection process by treating the terahertz as a quasi-DC field in the plasma current model. The predicted deviation from linearity at high THz field strength is yet another discrepancy from the four-wave mixing picture, which is a potential experimental evidence to the underlying mechanism

We have also reported the first spectro-temporal study of large single-cycle THz induced FKE in bulk and multiple quantum well structures at room temperature. The terahertz induced electroabsorption is very promising for broadband terahertz detection. The large modulation we observed is attributed to the Franz-Keldysh effect, and the data is modeled successfully with the combined effect of the FKE and the Fabry-Perot. Even with the incoherent detection, we have shown that the retrieval of the terahertz envelope is possible. For future studies, the THz induced QCSE in an ADQW structure has the

potential for coherent detection, but with a less trivial experimental setup. With the large EA observed from FKE, it is reasonable to expect coherent detection can only be achieved when the incident terahertz is entirely polarized in the quantum confinement direction. Even so, the prospect of achieving broadband coherent terahertz detection with an ADQW is very exciting.

Using the terahertz induced electroabsorption we have demonstrated two imaging techniques, large-area and raster scan. To our knowledge, this is the first demonstration of THz imaging techniques base on electroabsorption. The imaging of the air-plasma THz source is consistent with the predicted terahertz profile. With an uniform terahertz source, large-area fast terahertz imaging should be a viable technique. While the circular metallic wave guides have shown effects for improving phase matching in OBCD. For generation, there is however enough to explore and warrant another dissertation. Terahertz raster scan of a large object is presented in this dissertation. The raster scan method has limited speed. However, various schemes to improve acquisition speed, which we could benefit from, have been reported.

Appendix A FemtoFit

A FemtoFit is a commercially produced pulse shaper/measurer; the principle of measurement is the multiphoton intrapulse interference phase scan (MIIPS) [126] [127]. A known phase function is added to the measuring pulse by a spectral light modulator (SLM, a liquid crystal array). FemtoFit performs phase retrieval by measuring a set of phase dependent second harmonic spectrum. The spectral phase is compensated with the SLM to optimize the output pulse.

The second harmonic spectrum $S^{(2)}(\Delta)$ at frequency $2(\omega_0 + \Delta)$, where ω_0 is the central frequency of the fundamental, is related to the spectral phase $\varphi(\Delta)$ by [127]:

$$S^{(2)}(\Delta) \propto \left| \int |A(\Delta + \Omega)| |A(\Delta - \Omega)| e^{i[\varphi(\Delta + \Omega) + \varphi(\Delta - \Omega)]} d\Omega \right|. \quad (\text{A.1})$$

Expanding the spectral phase in Eq. (A.1) around Δ , the SH spectrum is only affected by even-order terms. The zero-order term is a constant:

$$S^{(2)}(\Delta) \propto \left| e^{2i\varphi(\Delta)} \int |A(\Delta + \Omega)| |A(\Delta - \Omega)| e^{2i \sum_{n=2(m+1)}^{\infty} \frac{\varphi^{(n)}(\Delta)}{n!} \Omega^n} d\Omega \right|, \quad (\text{A.2})$$

where m is a positive integer. $S^{(2)}(\Delta)$ is maximum when spectral phase is minimal (transform limited pulse). FemtoFit optimizes the phase by adding a known phase function $f(\Delta, \delta)$. The total spectral phase is $\varphi(\Delta) = \phi(\Delta) + f(\Delta, \delta) = \phi(\Delta) + \alpha \cos(\gamma\Delta - \delta)$, where α and γ (\approx pulse duration) are constants. The δ -dependent SH spectrum $S^{(2)}(\Delta, \delta)$ (MIIPS) is measured for each iterative optimization that minimizes $\varphi''(\Delta)$, such that $\varphi''(\Delta) = f''(\Delta, \delta_{\max})$. Therefore, the pulse measurement process itself is also the pulse shaping process.

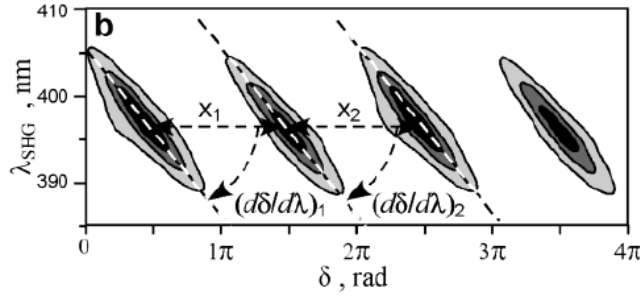


Figure A.0.1 MIIPS trace with transform limited pulse [128].

Intuitively, when the pulse is transform-limited, maximums of $S^{(2)}(\Delta, \delta)$ only occur at δ_{\max} for all wavelengths. The maximums also occur at an interval of π across the wavelength due to the cosine phase function $f(\Delta, \delta)$. Parallel lines in measured MIIPS trace serve as a visual confirmation that the pulse is transform-limited (Figure A.0.1).

A photo of optical setup in MIIPS is shown in Figure A.0.2 (a). The original pulse is spatially dispersed by the grating and focused onto the SLM. The slightly tilted return beam clears the first turning mirror and exits the enclosure. For optimizing a chirp pulse amplifier, such as the one in our setup, FemtoFit commonly sits between the seeding Ti:Sapphire oscillator beam and the amplifier. The detection section measures SH generated from amplifier pulse with a β -BBO crystal and a Ocean Optics USB spectrometer (USB4000). In this arrangement FemtoFit optimizes the oscillator pulse for a transform limited amplifier output; the potential damages to the SLM, caused by the high energy amplified pulse are avoided.

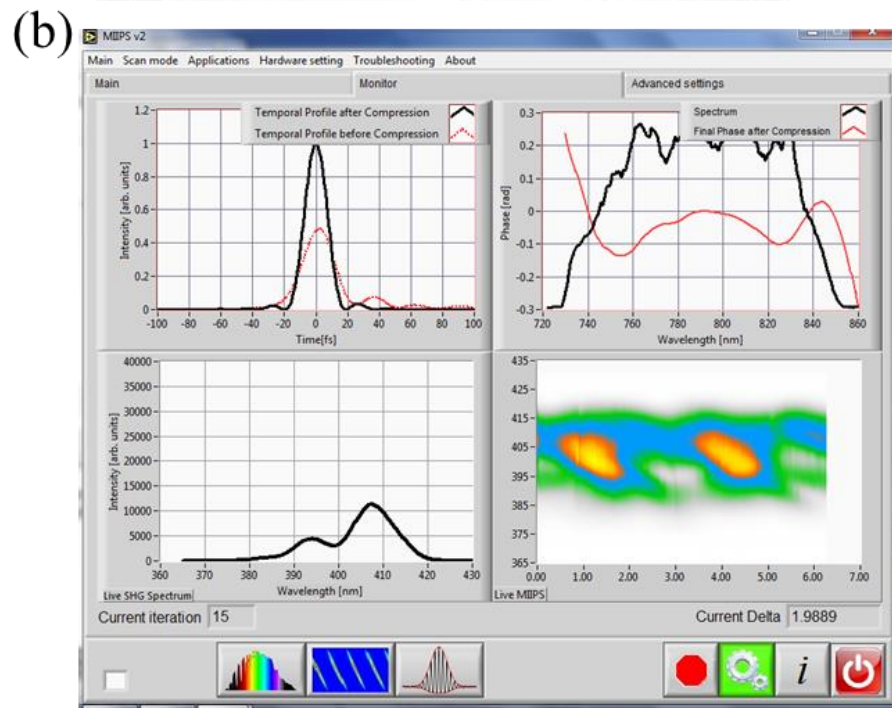
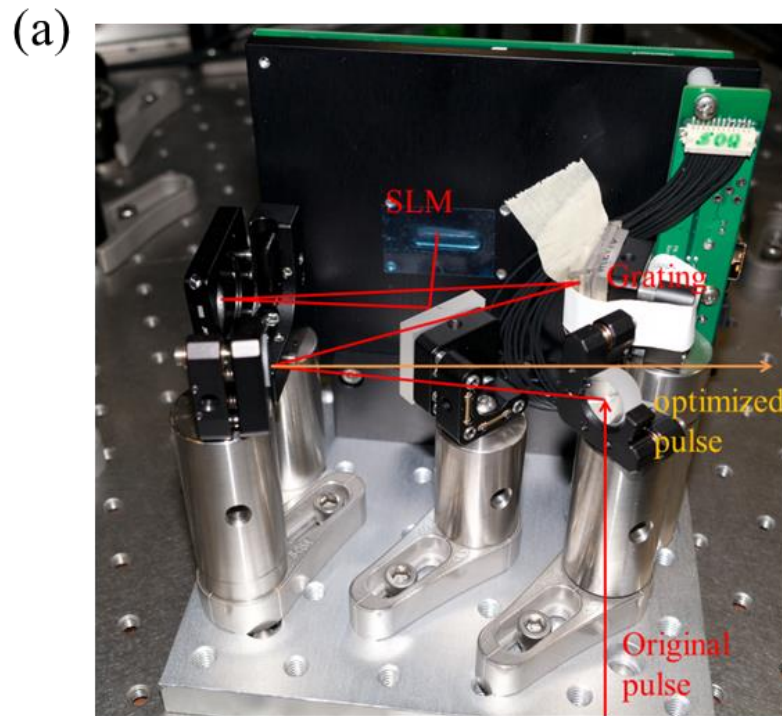


Figure A.0.2 (a) Photo of the MIIPS optics, and (b) the FemtoFit software interface. Optimization of Ti:Sapphire oscillator laser pulse is shown.

References

- [1] D. J. Paul , "Terahertz Research," 2004. [Online]. Available: <http://userweb.eng.gla.ac.uk/douglas.paul/terahertz.html>. [Accessed 11 2 2016].
- [2] X. C. Zhang and J. Xu, Introduction to THz Wave Photonics, New York: Springer, 2010.
- [3] B. B. Hu and M. C. Nuss, "Imaging with terahertz waves," *Opt. Lett.*, vol. 20, pp. 1716-1718, 1995.
- [4] K. Kawase, "Terahertz Imaging For Drug Detection And Large-Scale Integrated Circuit Inspection," *Opt. Photonics News*, vol. 15, no. 10, pp. 34-39, 2004.
- [5] M. P. Hasselbeck, D. Seletskiy, L. R. Dawson and M. Sheik-Bahae, "Direct observation of Landau damping in a solid state plasma," *Phys. Stat. Solidi (c)*, vol. 5, pp. 253-256, 2008.
- [6] D. J. Cook and R. M. Hochstrasser, "Intense terahertz pulses by four-wave rectification in air," *Opt. Lett.*, vol. 25, no. 16, pp. 1210-1212, 2000.
- [7] X. Xie, J. Dai and X.-C. Zhang, "Coherent Control of THz Wave Generation in Ambient Air," *Phys. Rev. Lett.*, vol. 96, no. 7, p. 075005, 2006.
- [8] M. Kress, T. Löffler, S. Eden, M. Thomson and H. G. Roskos, "Terahertz-pulse generation by photoionization of air with laser pulses composed of both fundamental and second-harmonic waves," *Opt. Lett.*, vol. 29, no. 10, pp. 1120-

- 1122, 2004.
- [9] N. Karpowicz, J. Dai, X. Lu, Y. Chen, M. Yamaguchi, H. Zhao, X.-C. Zhang, L. Zhang, C. Zhang, M. Price-Gallagher, C. Fletcher, O. Mamer, A. Lesimple and K. Johnson, "Coherent heterodyne time-domain spectrometry covering the entire "terahertz gap"," *Appl. Phys. Lett.*, vol. 92, no. 1, p. 011131, 2008.
- [10] E. R. Mueller, "Submillimeter wave lasers," in *Wiley Encyclopedia of Electrical and Electronics Engineering*. , Webster J. G. (Ed.), vol. 20, Hoboken, NJ: Wiley, 1999, p. 597–615.
- [11] P. Shumyatsky and R. R. Alfano, "Terahertz sources," *J. Biomed. Opt.*, vol. 16, no. 3, p. 033001 , 2011.
- [12] A. Staprans, E. W. McCune and J. A. Ruetz, "High-power linear-beam tubes," *Proceedings of the IEEE*, vol. 61, no. 3, pp. 299-330, 1973.
- [13] G. P. Gallerano and S. Biedron,, "Overview of Terahertz Radiation Sources," *Proc. of 2004 FEL conference* 216-221, 2004.
- [14] D. A. G. Deacon, L. R. Elias, J. M. J. Madey, G. J. Ramian, H. A. Schwettman and T. I. Smith, "First Operation of a Free-Electron Laser," *Phys. Rev. Lett.*, vol. 38, no. 16, pp. 892-894, 1977.
- [15] K. Park, R. E. Peale, H. Weidner and J. J. Kim, "Submillimeter p-Ge laser using a Voigt-configured permanent magnet," *IEEE J. Quantum*, vol. 32, no. 7, pp. 1203 - 1210, 1996.

- [16] S. G. Pavlov, R. K. Zhukavin, E. E. Orlova and V. N. Shastin, "Stimulated Emission from Donor Transitions in Silicon," *Phys. Rev. Lett.*, vol. 84, no. 22, pp. 5220-5223, 2000.
- [17] A. Borak, "Toward Bridging the Terahertz Gap with Silicon-Based Lasers," *Science*, vol. 308, no. 5722, pp. 638-639, 2005.
- [18] R. F. Kazarinov and R. A. Suris, "Possibility of amplification of electromagnetic waves in a semiconductor with a superlattice," *Sov. Phys. Semi-cond.*, vol. 5, no. 207, p. 797–800, 1971.
- [19] J. Faist, F. Capasso, D. L. Sivco, C. Sirtori, A. L. Hutchinson and A. Y. Cho, "Quantum Cascade Laser," *Science*, vol. 264, no. 5158, pp. 553-556, 1994.
- [20] E. R. Brown, K. A. McIntosh, F. W. Smith, M. J. Manfra and C. L. Dennis, "Measurements of optical-heterodyne conversion in low-temperature-grown GaAs," *Appl. Phys. Lett.*, vol. 62, no. 11, pp. 1206-1208, 1993.
- [21] P. R. Smith, D. H. Auston and M. C. Nuss, "Subpicosecond photoconductive dipole antennas," *IEEE J. Quantum Electron.*, vol. 24, no. 2, pp. 255-260, 1988.
- [22] R. W. Boyd, Nonlinear Optics, San Diego: Academic Press, 2008.
- [23] M. Bass, P. A. Franken, J. F. Ward and G. Weinreich, "Optical Rectification," *Phys. Rev. Lett.*, vol. 9, no. 11, pp. 446-448, 1962.

- [24] X.-C. Zhang, Y. Jin, K. Yang and L. J. Schowalter, "Resonant Nonlinear Susceptibility near the GaAs Band Gap," *Phys. Rev. Lett.*, vol. 69, no. 15, p. 2303, 1992.
- [25] A. Rice, Y. Jin, X. F. Ma, X. -C. Zhang, D. Bliss, J. Larkin and M. Alexander, "Terahertz optical rectification from $\langle 110 \rangle$ zinc-blende crystals," *Appl. Phys. Lett.*, vol. 64, no. 11, pp. 1324-1326, 1994.
- [26] C. Riek, D. V. Seletskiy, A. S. Moskalenko, J. F. Schmidt, P. Krauspe, S. Eckart, S. Eggert, G. Burkard and A. Leitenstorfer, "Direct sampling of electric-field vacuum fluctuations," *Science*, vol. 350, no. 6259, pp. 420-423, 2015.
- [27] A. Nahata, A. S. Weling and T. F. Heinz, "A wideband coherent terahertz spectroscopy system using optical rectification and electro-optic sampling," *Appl. Phys. Lett.*, vol. 69, p. 2321, 1996.
- [28] S. L. Chuang, S. Schmitt-Rink, B. I. Greene, P. N. Saeta and A. F. J. Levi, "Optical Rectification at Semiconductor Surfaces," *Phys. Rev. Lett.*, vol. 68, no. 1, p. 102, 1992.
- [29] R. A. Kandl, F. Eickemeyer, M. Woerner and T. Elsaesser, "Broadband phase-matched difference frequency mixing of femtosecond pulses in GaSe: Experiment and theory," *Appl. Phys. Lett.*, vol. 75, no. 8, p. 1060, 1999.
- [30] Y.-S. Lee, T. Meade, V. Perlin, H. Winful and T. B. Norris, "Generation of narrow-band terahertz radiation via optical rectification," *Appl. Phys. Lett.*, vol. 76, no. 18, p. 2505, 2000.

- [31] X. Zheng, S. Wu, R. Sobolewski, R. Adam, M. Mikulics, P. Kordos and M. Siegel, "Electro-optic sampling system with a single-crystal 4-N,N-dimethylamino-4 '-N '-methyl-4-stilbazolium tosylate sensor," *Appl. Phys. Lett.*, vol. 82, pp. 2383-2385, 2003.
- [32] A. Schneider, M. Neis, M. Stillhart, B. Ruiz, R. U. A. Khan and P. Günter, "Generation of terahertz pulses through optical rectification in organic DAST crystals: theory and experiment," *J. Opt. Soc. Am. B*, vol. 23, no. 9, p. 1822, 2006.
- [33] Z. Yang, L. Mutter, M. Stillhart, B. Ruiz, S. Aravazhi, M. Jazbinsek, A. Schneider, V. Gramlich and P. Gunter, "Large-size bulk and thin-film stilbazolium-salt single crystals for nonlinear optics and THz generation," *Adv. Funct. Mater.*, vol. 17, pp. 2018-2023, 2007.
- [34] L. Mutter, F. D. J. Brunner, Z. Yang, M. Jazbinsek and P. Gunter, "Linear and nonlinear optical properties of the organic crystal DSTMS," *J. Opt. Soc. Am. B*, vol. 24, pp. 2556-2561, 2007.
- [35] O. P. Kwon, S. J. Kwon, M. Jazbinsek, F. D. J. Brunner, J. I. Seo, C. Hunziker, A. Schneider, H. Yun, Y. S. Lee and P. Gunter, "Organic Phenolic Configurationally Locked Polyene Single Crystals for Electro-optic and Terahertz Wave Applications," *Adv. Funct. Mater.*, vol. 18, pp. 3242-3250, 2008.
- [36] F. D. J. Brunner, O. P. Kwon, S. J. Kwon, M. Jazbinsek, A. Schneider and P. Gunter, "A hydrogen-bonded organic nonlinear optical crystal for high-efficiency terahertz generation and detection," *Opt. Express*, vol. 16, pp. 16496-16508, 2008.

- [37] M. Shalaby and C. P. Hauri, "Demonstration of a low-frequency three-dimensional terahertz bullet with extreme brightness," *Nat. Commun.*, vol. 6, p. 5976, 2015.
- [38] S. Kono, M. Tani, P. Gu and K. Sakai, "Detection of up to 20 THz with a low-temperature-grown GaAs photoconductive antenna gated with 15 fs light pulses," *App. Phys. Lett.*, vol. 77, no. 25, pp. 4104-4106, 2000.
- [39] Z. Piao, M. Tani and K. Sakai, "Carrier Dynamics and Terahertz Radiation in Photoconductive Antennas," *Jpn. J. Appl. Phys.*, vol. 39, no. 1, pp. 96-100, 2000.
- [40] Y.-S. Lee, Principles of Terahertz Science and Technology, New York: Springer, 2009.
- [41] J. F. O'Hara, J. M. O. Zide, A. C. Gossard, A. J. Taylor and R. D. Averitt, "Enhanced terahertz detection via ErAs:GaAs nanoisland superlattices," *Appl. Phys. Lett.*, vol. 88, p. 251119, 2006.
- [42] T.-A. Liu, M. Tani, M. Nakajima, M. Hangyo and C.-L. Pan, "Ultrabroadband terahertz field detection by photoconductive antennas based on multi-energy arsenic-ion-implanted GaAs and semi-insulating GaAs," *Appl. Phys. Lett.*, vol. 83, no. 7, pp. 1322-1324, 2003.
- [43] B. Salem, D. Morris, V. Aimez, J. Beauvais and D. Houde, "Improved characteristics of a terahertz set-up built with an emitter and a detector made on proton-bombarded GaAs photoconductive materials," *Semicond. Sci. Technol.*, vol. 21, pp. 283-286, 2006.

- [44] M. Mikulics, M. Marso, S. Mantl, H. Lüth and P. Kordoš, "GaAs photodetectors prepared by high-energy and high-dose nitrogen implantation," *Appl. Phys. Lett.*, vol. 89, p. 091103, 2006.
- [45] D. S. Kim and D. S. Citrin, "Coulomb and radiation screening in photoconductive terahertz sources," *Appl. Phys. Lett.*, vol. 88, p. 161117, 2006.
- [46] A. Dreyhaupt, S. Winnerl, T. Dekorsy and M. Helm, "High-intensity terahertz radiation from a microstructured," *Appl. Phys. Lett.*, vol. 86, p. 121114, 2005.
- [47] F. Peter, S. Winnerl, S. Nitsche, A. Dreyhaupt, H. Schneider and M. Helm, "Coherent terahertz detection with a large-area photoconductive antenna," *Appl. Phys. Lett.*, vol. 91, p. 081109, 2007.
- [48] S. E. Ralph and D. Grischkowsky, "Trap-enhanced electric fields in semi-insulators: The role of electrical and optical carrier injection," *Appl. Phys. Lett.*, vol. 59, no. 16, pp. 1972-1974, 1991.
- [49] J. H. Kim, A. Polley and S. E. Ralph, "Efficient photoconductive terahertz source using line excitation," *Opt. Lett.*, vol. 30, pp. 2490-2492, 2005.
- [50] D. S. Kim and D. S. Citrin, "Efficient terahertz generation using trap-enhanced fields in semi-insulating photoconductors by spatially broadened excitation," *J. Appl. Phys.*, vol. 101, p. 053105, 2007.
- [51] H. Zhang, J. K. Wahlstrand, S. B. Choi and S. T. Cundiff, "Contactless photoconductive terahertz generation," *Opt. Lett.*, vol. 36, no. 2, p. 223, 2011.

- [52] H. Hamster, A. Sullivan, S. Gordon, W. White and R. W. Falcone, "Subpicosecond, Electromagnetic Pulses from Intense Laser-Plasma Interaction," *Phys. Rev. Lett.*, vol. 71, no. 17, pp. 2725-2728, 1993.
- [53] T. Löffler, M. Kress, M. Thomson and H. G. Roskos, "Efficient Terahertz Pulse Generation in Laser-Induced Gas Plasmas," *Acta Physica Polonica A*, vol. 107, no. 1, p. 99, 2005.
- [54] T. Dekorsy, H. Auer, H. J. Bakker, H. G. Roskos and H. Kurz, "THz electromagnetic emission by coherent infrared-active phonons," *Phys. Rev. B*, vol. 53, p. 4005, 1996.
- [55] M. B. Johnston, D. M. Whittaker, A. Corchia, A. G. Davies and E. H. Linfield, "Simulation of terahertz generation at semiconductor surfaces," *Phys. Rev. B*, vol. 65, p. 165301, 2002.
- [56] D. Seletskiy, M. P. Hasselbeck, J. G. Cederberg, A. Katzenmeyer, M. E. Toimil-Molares, F. Leonard, A. A. Talin and M. Sheik-Bahae, "Efficient terahertz emission from InAs nanowires," *Phys. Rev. B*, vol. 84, p. 115421, 2011.
- [57] C. D'Amico, A. Houard, M. Franco, B. Prade and A. Mysyrowicz, "Conical Forward THz Emission from Femtosecond-Laser-Beam Filamentation in Air," *Phys. Rev. Lett.*, vol. 98, p. 235002, 2007.
- [58] M. Kress, T. Löffler, S. Eden, M. Thomson and H. G. Roskos, "Terahertz-pulse generation by photoionization of air with laser pulses composed of both fundamental and second-harmonic waves," *Opt. Lett.*, vol. 29, no. 10, pp. 1120-

- 1122, 2004.
- [59] T. Bartel, P. Gaal, K. Reimann, M. Woerner and T. Elsaesser, "Generation of single-cycle THz transients with high electric-field amplitudes," *Opt. Lett.*, vol. 30, no. 20, pp. 2805-2807, 2005.
- [60] Y. Minami, M. Nakajima and T. Suemoto, "Effect of preformed plasma on terahertz-wave emission from the plasma generated by two-color laser pulses," *Phys. Rev. A*, vol. 82, no. 2, p. 023828, 2011.
- [61] K. Y. Kim, J. H. Gownia, A. J. Taylor and G. Rodriguez, "Terahertz emission from ultrafast ionizing air in symmetry-broken laser fields," *Opt. Exp.*, vol. 15, no. 8, pp. 4577-4584, 2007.
- [62] K. Y. Kim, A. J. Taylor, J. H. Gownia and G. Rodriguez, "Coherent control of terahertz supercontinuum generation in ultrafast laser-gas interactions," *Nature Photon.*, vol. 2, pp. 605-609, 2008.
- [63] L. D. Landau and E. M. Lifshitz, Quantum Mechanics, 2nd Ed., New York: Pergamon, 1965.
- [64] M. Goeppert-Mayer, "Über Elementarakte mit zwei Quantensprüngen," *Annals of Physics*, vol. 9, no. 3, p. 273, 1931.
- [65] L. V. Keldysh, "Ionization in the field of a strong electromagnetic wave," *Soc. Phys. JETP*, vol. 20, pp. 1307-1314, 1965.

- [66] M. V. Ammosov, N. B. Delone and V. P. Krainov, "Tunnel ionization of complex atoms and of atomic ions in an alternating electromagnetic field," *Sov. Phys. JETP*, vol. 64, pp. 1191-1194, 1986.
- [67] K. Y. Kim, "Generation of coherent terahertz radiation in ultrafast laser-gas interactions," *Phys. Plasmas*, vol. 16, p. 056706, 2009.
- [68] T. Brabec and F. Krausz, "Nonlinear Optical Pulse Propagation in the Single-Cycle Regime," *Phys. Rev. Lett.*, vol. 78, no. 17, pp. 3282--3285, 1997.
- [69] Y. S. You, T. I. Oh and K. Y. Kim, "Off-axis phase-matched terahertz emission from two-color laser-induced plasma filaments," *Phys. Rev. Lett.*, vol. 109, no. 18, p. 183902, 2012.
- [70] P. L. Richards, "Bolometers for infrared and millimeter waves," *J. Appl. Phys.*, vol. 76, no. 1, p. 1, 1994.
- [71] H. P. Beerman, "The pyroelectric detector of infrared radiation," *Electron Devices, IEEE Transactions on*, vol. 16, no. 6, pp. 554-557, 1969.
- [72] M. J. E. Golay, "Theoretical consideration in heat and infra-red detection, with particular reference to the pneumatic detector," *Rev. Sci. Instrum.*, vol. 18, p. 347, 1947.
- [73] I.-C. Ho, X. Guo and X.-C. Zhang, "Design and performance of reflective terahertz air-biased-coherent-detection for time-domain spectroscopy," *Opt. Express*, vol. 18, p. 2872, 2010.

- [74] M. V. Exter and D. R. Grischkowsky, "Characterization of an optoelectronic terahertz beam system," *IEEE Trans. Microwave Theory Tech.*, vol. 38, no. 11, pp. 1684-1691, 1990.
- [75] Q. Wu and X.-C. Zhang, "Free-space electro-optic sampling of terahertz beams," *Appl. Phys. Lett.*, vol. 67, p. 3523, 1995.
- [76] J. Dai., X. Xie and Z.-C. Zhang, "Detection of Broadband Terahertz Waves with a Laser-Induced Plasma in Gases," *Phys. Rev. Lett.*, vol. 97, no. 10, p. 103903, 2006.
- [77] Z. Jiang, F. G. Sun, Q. Chen and X.-C. Zhang, "Electro-optic sampling near zero optical transmission point," *Appl. Phys. Lett.*, vol. 74, p. 1191, 1999.
- [78] Q. Wu and X.-C. Zhang, "7 terahertz broadband GaP electro-optic sensor," *Appl. Phys. Lett.*, vol. 70, p. 1784, 1997.
- [79] R. Huber, A. Brodschelm, F. Tauser and A. Leitenstorfer, "Generation and field-resolved detection of femtosecond electromagnetic pulses tunable up to 41 THz," *Appl. Phys. Lett.*, vol. 76, p. 3191, 2000.
- [80] W. Sha, T. B. Norris, J. W. Burm, D. Woodard and W. J. Schaff, "New coherent detector for terahertz radiation based on excitonic electroabsorption," *Appl. Phys. Lett.*, vol. 61, no. 15, pp. 1763-1765, 1992.
- [81] M. Aguilar, M. Carrascosa, F. Agulló-López, M. R. Melloch and D. D. Nolte, "Linear electroabsorption in semi-insulating GaAs/AlGaAs asymmetric double quantum wells," *J. Appl. Phys.*, vol. 86, no. 7, p. 3822, 1999.

- [82] D. J. Cook, J. X. Chen, E. A. Morlino and R. M. Hochstrasser, "Terahertz-field-induced second-harmonic generation measurements of liquid dynamics," *Chem. Phys. Lett.*, vol. 309, no. 3-4, pp. 221-228, 1999.
- [83] A. Nahata and T. F. Heinz, "Detection of freely propagating terahertz radiation by use of optical second-harmonic generation," *Opt. Lett.*, vol. 23, no. 1, pp. 67-69, 1998.
- [84] H. Wang, K. Wang, J. Liu, H. Dai and Z. Yang, "Theoretical research on terahertz air-breakdown coherent detection with the transient photocurrent model," *Opt. Express*, vol. 20, no. 17, pp. 19264-19270, 2012.
- [85] Z. Lu, D. Zhang, C. Meng, L. Sun, Z. Zhou, Z. Zhao and J. Yuan, "Polarization-sensitive air-biased-coherent-detection for terahertz wave," *Appl. Phys. Lett.*, vol. 101, no. 8, p. 081119, 2012.
- [86] H. Zhong, N. Karpowicz and X.-C. Zhang, "Terahertz emission profile from laser-induced air plasma," *Appl. Phys. Lett.*, vol. 88, no. 26, p. 261103, 2006.
- [87] I. Babushkin, S. Skupin and J. Herrmann, "Generation of terahertz radiation from ionizing two-color laser pulses in Ar filled metallic hollow waveguides," *Opt. Express*, vol. 18, no. 9, pp. 9658-9663, 2010.
- [88] G. Gallot, S. P. Jamison, R. W. McGowan and D. Grischkowsky, "Terahertz waveguides," *J. Opt. Soc. Am. B*, vol. 17, no. 5, pp. 851-863, 2000.
- [89] J. Zhang and D. Grischkowsky, "Waveguide terahertz time-domain spectroscopy of

- nanometer water layers," *Opt. Lett.*, vol. 29, pp. 1617-1619, 2004.
- [90] R. W. McGowan, G. Gallot and D. Grischkowsky, "Propagation of ultrawideband short pulses of terahertz radiation through submillimeter-diameter circular waveguides," *Opt. Lett.*, vol. 24, pp. 1431-1433, 1999.
- [91] R. Mendis and D. Grischkowsky, "Plastic ribbon THz waveguides," *J. Appl. Phys.*, vol. 88, p. 4449, 2000.
- [92] S. P. Jamison, R. W. McGowan and D. Grischkowsky, "Single-mode waveguide propagation and reshaping of sub-ps terahertz pulses in sapphire fibers," *Appl. Phys. Lett.*, vol. 76, p. 1987, 2000.
- [93] R. Mendis and D. Grischkowsky, "Undistorted guided-wave propagation of subpicosecond terahertz pulses," *Opt. Lett.*, vol. 26, no. 11, pp. 846-848, 2001.
- [94] K. Wang and D. M. Mittleman, "Metal wires for terahertz wave guiding," *Nature*, vol. 432, pp. 376-379, 2004.
- [95] Y. B. Ji, E. S. Lee, J. S. Jang and T.-I. Jeon, "Enhancement of the detection of THz Sommerfeld wave using a conical wire waveguide," *Opt. Express*, vol. 16, pp. 271-278, 2008.
- [96] J. A. Deibel, K. Wang, M. D. Escarra and D. M. Mittleman, "Enhanced coupling of terahertz radiation to cylindrical wire waveguides," *Opt. Express*, vol. 14, pp. 279-290, 2006.

- [97] H. Harde, S. Keiding and D. Grischkowsky, "THz commensurate echoes: Periodic rephasing of molecular transitions in free-induction decay," *Phys. Rev. Lett.*, vol. 66, no. 14, pp. 1834--1837, 1991.
- [98] L. Zhang, H. Zhong, K. Mu, C. Zhang and Y. Zhao, "Phase characterization in broadband THz wave detection through field-induced second harmonic generation," *Opt. Exp.*, vol. 20, no. 1, pp. 75-80, 2012.
- [99] X. Lu, N. Karpowicz and X.-C. Zhang, "Broadband terahertz detection with selected gases," *JOSA B*, vol. 26, no. 9, pp. A66-A73, 2009.
- [100] W. Franz, "Einfluß eines elektrischen Feldes auf eine optische Absorptionskante," *Z. Naturforschung*, vol. 13a, p. 484–489, 1958.
- [101] L. V. Keldysh, "Behaviour of Non-Metallic Crystals in Strong Electric Fields," *J. Exptl. Theoret. Phys.*, vol. 33, p. 994–1003, 1957.
- [102] D. A. B. Miller, D. S. Chemla, T. C. Damen, A. C. Gossard, W. Wiegmann, T. H. Wood and C. A. Burrus, "Band-Edge Electroabsorption in Quantum Well Structures: The Quantum-Confining Stark Effect," *Phys. Rev. Lett.*, vol. 53, no. 22, pp. 2173-2176, 1984.
- [103] S. H. Autler and C. H. Townes, "Stark Effect in Rapidly Varying Fields," *Phys. Rev.*, vol. 100, no. 2, pp. 703-722, 1955.
- [104] S. Schmitt-Rink, D. S. Chemla, W. H. Knox and D. A. B. Miller, "How fast is excitonic electroabsorption?," *Optics Lett.*, vol. 15, no. 1, p. 60, 1990.

- [105] T. Ido, S. Tanaka, M. Suzuki, M. Koizumi, H. Sano and H. Inoue, "Ultra-high-speed multiple-quantum-well electro-absorption optical modulators with integrated waveguides," *J. Lightw. Technol.*, vol. 114, no. 9, pp. 2026-2034, 1996.
- [106] M. C. Hoffmann, B. S. Monozon, D. Livshits, E. U. Rafailov and D. Turchinovich, "Terahertz electro-absorption effect enabling femtosecond all-optical switching in semiconductor quantum dots," *Appl. Phys. Lett.*, vol. 97, p. 231108, 2010.
- [107] T. Ogawa, S. Watanabe, N. Minami and R. Shimano, "Room temperature terahertz electro-optic modulation by excitons in carbon nanotubes," *Appl. Phys. Lett.*, vol. 97, p. 041111, 2010.
- [108] J. R. Danielson, Y. S. Lee, J. P. Prineas, J. T. Steiner, M. Kira and S. W. Koch, "Interaction of Strong Single-Cycle Terahertz Pulses with Semiconductor QuantumWells," *Phys. Rev. Lett.*, vol. 99, p. 237401, 2007.
- [109] E. Yablonovitch, T. Gmitter, J. P. Harbison and R. Bhat, "Extreme selectivity in the lift-off of epitaxial GaAs films," *Appl. Phys. Lett.*, vol. 51, no. 26, pp. 2222-2224, 1987.
- [110] Z. Yang, A. R. Albrecht, J. G. Cederberg and M. Sheik-Bahae, "DBR-free optically pumped semiconductor disk lasers," in *Proc. SPIE 9349, Vertical External Cavity Surface Emitting Lasers (VECSELs) V*, 934905, 2015.
- [111] K. W. Böer, H. J. Hänsch and U. Kümmel, "Methode zum Sichtbarmachen von Leitfähigkeitsinhomogenitäten von Halbleitern," *Naturwiss.*, vol. 45, no. 19, p. 460, 1958.

- [112] S. L. Chuang, Physics of Optoelectronic Devices, New York: John Wiley & Sons, 1995.
- [113] Y. Yacoby, "High-Frequency Franz-Keldysh Effect," *Phys. Rev.*, vol. 169, p. 610, 1968.
- [114] A. P. Jauho and K. Johnsen, "Dynamical Franz-Keldysh Effect," *Phys. Rev. Lett.*, vol. 76, p. 4576 , 1996.
- [115] Q. Li, S.-H. Ding, R. Yao and Q. Wang, "Real-time terahertz scanning imaging by use of a pyroelectric array camera and image denoising," *J. Opt. Soc. Am. A*, vol. 27, pp. 2381-2386, 2010.
- [116] A. W. Lee and Q. Hu, "Real-time, continuous-wave terahertz imaging by use of a microbolometer focal-plane array," *Opt. Lett.*, vol. 30, p. 2563–2565, 2005.
- [117] B. Pradarutti, R. Müller, W. Freese, G. Matthäus, S. Riehemann, G. Notni, S. Nolte and A. Tünnermann, "Terahertz line detection by a microlens array coupled photoconductive antenna array," *Opt. Express*, vol. 16, p. 18443–18450, 2008.
- [118] Q. Wu, T. D. Hewitt and X.-C. Zhang, "Two-dimensional electro-optic imaging of THz beams," *Appl. Phys. Lett.*, vol. 69, p. 1026, 1996.
- [119] Z. G. Lu, P. Campbell and X.-C. Zhang, "Free-space electro-optic sampling with a high-repetition-rate regenerative amplified laser," *Appl. Phys. Lett.*, vol. 71, p. 593, 1997.

- [120] Z. Jiang and X.-C. Zhang, "Terahertz imaging via electrooptic effect," *Microwave Theory and Techniques, IEEE Transactions on*, vol. 47, no. 12, p. 2644, 1999.
- [121] Z. Jiang, X. G. Xu and X.-C. Zhang, "Improvement of terahertz imaging with a dynamic subtraction technique," *Appl. Opt.*, vol. 39, pp. 2982-2987, 2000.
- [122] W. L. Chan, M. L. Moravec, R. G. Baraniuk and D. M. Mittleman, "Terahertz imaging with compressed sensing and phase retrieval," *Opt. Lett.*, vol. 33, pp. 974-976, 2008.
- [123] W. L. Chan, K. Charan, D. Takhar, K. F. Kelly, R. G. Baraniuk and D. M. Mittleman, "A single-pixel terahertz imaging system based on compressed sensing," *Appl. Phys. Lett.*, vol. 93, p. 121105, 2008.
- [124] J. F. Federici, D. Gary, B. Schukin, F. Huang and H. Altan, "Terahertz imaging using an interferometric array," *Appl. Phys. Lett.*, vol. 83, p. 2477, 2003.
- [125] Z. Jiang and X.-C. Zhang, "Single-shot spatiotemporal terahertz field imaging," *Opt. Lett.*, vol. 23, no. 14, pp. 1114-1116, 1998.
- [126] Y. Coello, V. V. Lozovoy, T. C. Gunaratne, B. Xu, I. Borukhovich, C.-H. Tsing, T. Weinacht and M. Dantus, "Interference without an interferometer: a different approach to measuring, compressing, and shaping ultrashort laser pulses," *J. Opt. Soc. Am. B*, vol. 25, p. A140, 1992.
- [127] V. V. Lozovoy, I. Pastirk and M. Dantus, "Multiphoton intrapulse interference. IV. Ultrashort laser pulse spectral phase characterization and compensation," *Optics*

Lett., vol. 29, no. 7, p. 775, 2004.

- [128] J. M. D. Cruz, I. Pastirk, V. V. Lozovoy, K. A. Walowicz and M. Dantus, "Multiphoton Intrapulse Interference 3: Probing Microscopic Chemical Environments," *J. Phys. Chem. A*, vol. 108, p. 53, 2004.
- [129] P. E. Ciddor, "Refractive index of air: new equations for the visible and near infrared," *Appl. Opt.*, vol. 35, no. 9, pp. 1566-1573, 1996.
- [130] M. Joffre, D. Hulin, A. Migus, A. Antonetti, C. Benoit a la Guillaume, N. Peyghambarian,, M. Lindberg and S. W. Koch, "Coherent effects in pump-probe spectroscopy of excitons," *Opt. Lett.*, vol. 13, no. 4, pp. 276-278, 1988.
- [131] L. D. Landau and E. M. Lifshitz, Quantum Mechanics, New York: Pergamon, 1965.